

分类号: TN292.11

单位代码: 10335

密 级: \_\_\_\_\_

学 号: 10930033

# 浙江大学

## 博士学位论文



中文论文题目: 紫外激光诱导的量子阱混合技术  
及光子集成器件应用

英文论文题目: UV-Laser Induced Quantum Well Intermixing Technique  
and Its Applications for Photonic Integrated Devices

申请人姓名: Mohammad Kaleem

指导教师: Jian-Jun He

合作导师: \_\_\_\_\_

专业名称: Optical Communication Engineering

研究方向: Integrated Optoelectronics

所在学院: College of Information Science and Engineering

论文提交日期 April, 2013



## **Acknowledgements**

This work would not have been possible without a great deal of support and guidance from a great number of people. Firstly, I would like to thank my PHD supervisor Jian-Jun He, Professor at the Department of Optical Engineering of Zhejiang University for the quality of his supervision. His unconditional support and the experience and knowledge he shared with me ensured the success of the different phases of my work. Without his guidance, encouragements and, sometime, “cracking-of-the-whip”, I would never have finished.

I would also like to express my deepest thanks to Jan Dubowski, Professor at the department of Electrical and Computer engineering of the University of Sherbrooke for his thought provoking discussions and tremendous help.

I would like to express my gratitude and many thanks to my fellow PhD colleagues, especially Xin Zhang for offering precious time, great help, guidance and suggestions. Their inputs were always appreciated and helpful. Thanks to all of you for making my time at ZJU a great experience both in the lab and in the outside world.

I also thank the rest of the academic, support staff and members of the clean room staff of the Zhejiang University as well as the other undergraduate and graduated students with whom I had the chance to interact during the last four years.

Finally, I have to say a sincere 'thank-you' to all my friends and family, wherever they are, particularly my parents and most importantly my wife and children from whom I could not ask for anything more, for making me the person I am today.

Last but not least, I would also like to express my sincere gratitude to Dr Ming-Yu Li, for his kind guidance and support through out my PHD.



## 摘要

对二十一世纪的电信业而言，带宽的需求正在不断增加。波分复用（WDM）技术的问世，大大提升了光纤传送的数据量。目前，一些关键技术的发展有望彻底改变这种状况。其一是应用大范围可调谐激光器，它可调整到国际电信联盟（ITU）指定的任意信道，取代固定波长激光器，这将大大降低系统运行的成本。其二是光子集成回路（PIC），它将允许通过单片集成降低成本。与这些关键技术配套的设备是搭建下一代高效、高带宽光纤网络的理想积木。

类似于电子集成中的方式将分立元件集成到一个系统中，可以有效地提高性能、可靠性和功能性，并同时降低制造成本。光子集成回路的制作需要将多个带隙结构整合在一个单一的半导体芯片里。量子阱混合（QWI）是一种很有前途的实现多功能单片集成元件的技术。与选择性区域外延和蚀刻再生长技术相比，量子阱混合技术要简单得多，更好的重复性，并可有效地调节量子阱结构的带隙。在其它潜在的实现单片光子集成回路的技术中，在选定的区域进行生长后量子阱混合的方法，可以增加半导体量子阱结构的有效带隙能量。杂质和点缺陷，比如自由空位和填隙，能加速由热引起的混合过程。

基于以上认识，本论文工作拟研究基于生长  $\text{SiO}_2$  和  $\text{Al}_2\text{O}_3$  后的紫外激光的量子阱混合，并探索与此对应的新型晶片加工技术。其中的量子阱混合过程中允许形成多个量子阱带隙，理想情况下每一个对应于特定的集成组件。我们调查了紫外线照射如何创建这些点缺陷，以及在特定区域的 InP 量子阱结构的点缺陷和热扩散是如何控制量子阱混杂的。本论文工作探究了基于  $\text{SiO}_2$ ,  $\text{Al}_2\text{O}_3$  和紫外激光的量子阱混杂技术领域的工作，并实现了该技术在光子集成回路的光子器件中。主要的创新包括：

1. 发展了紫外激光诱导量子阱混合技术，首次将其应用于压应变的量子阱结构，得到了 142 nm 的蓝移，比普通量子阱结构中的蓝移更大，同时具有增强的 PL 强度和更窄的半极大处全宽度（FWHM）。
2. 使用紫外激光诱导量子阱混杂技术，在 InGaAsP 量子阱结构上制作了无源光波导。光波导在 1545 nm 的损耗从 110 dB/cm 降到 20 dB/cm。
3. 使用紫外激光诱导量子阱混杂技术，在压应变 InGaAsP 量子阱结构上制作了激射波长为 1435 nm 的 FP 腔激光器，并且得到了更低的阈值电流和更大的输出功率。
4. 实现了在标准的 InGaAsP/ InP 压应变多量子阱结构上的氩离子诱导溅射 SiO<sub>2</sub>的量子阱混合，并且系统地研究了射频功率、退火温度的改变与量子阱 PL 峰蓝移、PL 强度的关系。
5. 第一次提出并研究了在带和不带牺牲层的 InGaAsP/ InP 多量子阱结构上的 Al<sub>2</sub>O<sub>3</sub>等离子体诱导量子阱混杂技术，并且获得超过 110 nm 的蓝移。

**关键词：**光子集成； 量子阱混合 (QWI)； 光致发光 (PL)； 氩离子诱导量子阱混杂； 光子集成电路 (PIC)； 低损耗波导； 半导体激光器.

## **Abstract**

Demand for bandwidth continues to increase for the twenty-first century's telecommunication industry. The advent of wavelength division multiplexing (WDM) technique has greatly increased the quantity of data transported within each optical fiber. Several key technologies are poised to revolutionize the communication industry. The introduction of widely-tunable lasers that are capable of tuning to any channel on the international telecommunications union (ITU) grid will dramatically reduce the cost of running system through sparing functions, allowing system operators to reduce laser inventory and replacing fixed wavelength lasers with tunable lasers. Another key technology is the photonic integrated circuit (PIC), which can allow the cost reduction through monolithic integration. These devices are considered ideal building blocks for the development of next generation, efficient, high bandwidth fiber optic networks.

Integration of discrete components into a single system is similar to that of electronic integration. It enhances the performance, reliability and increases the functionality while lowering the cost of manufacturing. Fabrication of photonic integrated circuits requires the integration of multiple bandgap structures within a single semiconductor chip. Quantum well intermixing (QWI), among others is a promising technique for realizing multifunctional monolithic integrated components. QWI is much simpler, reproducible and effective to modify the band-gap of quantum well structure as compared to the selective-area-epitaxy or etch-and-re-growth techniques.

Among other potential techniques to achieve monolithic photonic integrated circuits, post-growth quantum well intermixing in selected regions increases the effective band gap energy of a semiconductor QW structures. Thermally activated intermixing process is accelerated by the diffusion of impurities and of point defects such as free vacancies and interstitials.

For this thesis work, we investigate and demonstrate experimentally ultra-violet laser based post-growth QWI technique and then develop a novel wafer processing technique using UV-laser QWI. The QWI process allows the formation of multiple quantum well band edges, ideally one specific to each integrated component. We investigate how UV irradiation creates point defect and how the thermal diffusion of these point defects in InP based QW structures controls the quantum well intermixing in specific regions. We further investigated two other QWI techniques using the sputtering of  $\text{SiO}_2$  and  $\text{Al}_2\text{O}_3$  as an alternative to UV-laser QWI.

This thesis presents my contribution to post-growth UV-laser,  $\text{SiO}_2$  and  $\text{Al}_2\text{O}_3$  based quantum well intermixing techniques and demonstrates the applications of UV-laser QWI for photonic devices that can lead to photonic integrated circuits. The main innovations are as follows:

1. Developed experimentally UV-laser induced quantum well intermixing and applied it to strained multiple quantum well (MQW) structure. Obtained larger blue shift (over 142 nm) as compared to unstrained MQW, while the PL peak intensity becomes even higher with narrower full width at half maximum (FWHM).
2. Fabricated passive optical waveguides using UV-laser induced quantum well intermixing in InGaAsP/InP quantum well structure. The loss of the waveguide for 1545nm light drops from 110dB/cm to 20dB/cm.
3. Fabricated Fabry-Perot cavity lasers with blue-shifted lasing wavelength of 1435nm using UV-laser induced quantum well intermixing in InGaAsP/InP strained quantum well structure and obtained a lower threshold current and a large output power.
4. Implemented the Argon plasma induced QWI during the sputtering of  $\text{SiO}_2$  in standard InGaAsP/InP compressively strained multiple quantum well structure and systematically studied the relations of RF power, annealing temperature to the altered quantum well PL peak blue-shift and PL intensity.

5. Proposed and investigated sputtering of Al<sub>2</sub>O<sub>3</sub> induced quantum well intermixing technique in InGaAsP/InP multiple quantum well structure with and without sacrificial layer for the first time, and obtained over 110nm blue-shift.

**Key words:** Photonic integration, Quantum well intermixing (QWI), Photoluminescence (PL), Argon Plasma Induced Quantum well intermixing, Photonic integrated circuit (PIC), Low loss waveguide, semiconductor lasers.



## TABLE OF CONTENTS

<b>ACKNOWLEDGEMENTS.....</b>	<b>I</b>
<b>摘要.....</b>	<b>III</b>
<b>ABSTRACT.....</b>	<b>V</b>
<b>1 GENERAL INTRODUCTION.....</b>	<b>1</b>
1.1 MOTIVATION OF THE WORK.....	1
1.2 PIC FABRICATION TECHNIQUES.....	5
1.2.1 Hybrid Integration.....	6
1.2.2 Monolithic Integration.....	8
1.3 PROJECT DESCRIPTION.....	11
<b>2 THEORY OF ENERGY BAND STRUCTURE AND INTERACTION OF LIGHT WITH SEMICONDUCTORS.....</b>	<b>14</b>
2.1 INTRODUCTION.....	14
2.2 ENERGY BAND STRUCTURES IN SEMICONDUCTORS.....	14
2.3 THE QUANTUM WELL.....	17
2.4 CHARGE CARRIERS RECOMBINATION.....	18
2.5 STRAIN AND STRESS.....	20
2.5.1 Strain.....	21
2.5.2 Stress.....	21
2.5.3 Effect of Strain on the Band Structure of a Crystal.....	22
2.5.4 Example of an InGaAs/GaAs Quantum Well Under Biaxial Strain.....	24
2.6 LASER INTERACTION WITH SEMICONDUCTORS.....	26
2.6.1 Photo-excitation and Surface Response.....	26
2.6.2 Laser Induced Desorption and Ablation.....	28
2.6.3 Laser Pulse Absorption and Heat Transfer Processes.....	29
2.7 SUMMERY.....	31
<b>3 QUANTUM WELL INTERMINGING TECHNIQUES.....</b>	<b>32</b>
3.1 INTRODUCTION.....	32
3.2 DESCRIPTION OF THE QUANTUM WELL INTERMINGING PROCESS.....	33
3.3 DIFFUSION EQUATION AND CALCULATION OF ENERGY LEVELS.....	33
3.4 POINT DEFECTS INFLUENCE.....	36
3.5 POINT DEFECT DIFFUSION UNDER A STRAIN GRADIENT.....	39
3.6 REVIEW OF QUANTUM WELL INTERMINGING TECHNIQUES.....	41
3.7 IMPURITY INDUCED DISORDERING.....	42
3.8 IMPURITY-FREE VACANCY DISORDERING.....	43
3.9 DIELECTRIC SPUTTERING INDUCED INTERMINGING.....	47
3.10 LOW TEMPERATURE EPITAXIAL “DEFECT” LAYER.....	49
3.11 ION IMPLANTATION INDUCED QUANTUM WELL INTERMINGING.....	50
3.12 PLASMA INDUCED DEFECT DISORDERING.....	53
3.13 LASER INDUCED QUANTUM WELL INTERMINGING.....	54
3.13.1 Continuous Wavelength Laser Induced QWI.....	54
3.13.2 Pulsed Laser Induced Disorder.....	56
3.13.3 Ultra-Violet Laser Induced Quantum Well Interminging.....	57
3.14 SUMMARY.....	61
<b>4 UV-LASER INDUCED QUANTUM WELL INTERMINGING AND PHOTONIC INTEGRATED DEVICES.....</b>	<b>64</b>
4.1 INTRODUCTION.....	64

<b>4.2 EXCIMER LASERS.....</b>	<b>65</b>
4.2.1 KrF Laser Characteristics.....	67
<b>4.3 InGaAsP/InP Heterostructure.....</b>	<b>68</b>
<b>4.4 Irradiation Setup.....</b>	<b>69</b>
4.4.1 ProMaster (KrF laser).....	70
4.4.2 Masks.....	70
4.4.3 UV Illumination Optics.....	71
4.4.4 Image Projection Lens.....	72
4.4.5 Vision Systems.....	72
4.4.6 Environment.....	72
4.4.7 Process Control.....	72
4.4.8 ProMaster System Architecture.....	73
4.4.9 Laser.....	73
4.4.10 ProMaster BDU.....	73
4.4.11 Part Motion.....	74
4.4.12 Controls.....	74
<b>4.5 CHARACTERIZATION TECHNIQUES.....</b>	<b>74</b>
4.5.1 Principle of Photoluminescence.....	75
4.5.2 Recombination Mechanism.....	77
<b>4.6 UV-LASER PROCESSING OF THE QW MATERIAL.....</b>	<b>79</b>
<b>4.7 ETCH RATE.....</b>	<b>80</b>
<b>4.8 PL MAPS.....</b>	<b>81</b>
<b>4.9 UV-LASER OF DEVICE FABRICATION.....</b>	<b>81</b>
<b>4.10 LOW LOSS PASSIVE WAVEGUIDE.....</b>	<b>82</b>
4.10.1 Waveguide Structure.....	82
4.10.2 Fabrication Steps.....	84
4.10.3 Characterization and Testing Result.....	85
4.10.4 Measurement Setup.....	86
<b>4.11 FABRY-PEROT LASER.....</b>	<b>89</b>
4.11.1 Fabrication Steps.....	89
4.11.2 Measurement Setup.....	90
4.11.3 Characterisation.....	91
<b>4.12 SUMMARY.....</b>	<b>93</b>
<b>5 QWI by Sputtering SiO<sub>2</sub> and Al<sub>2</sub>O<sub>3</sub> Methods Procedures, Experiments and Results .....</b>	<b>95</b>
<b>5.1 INTRODUCTION.....</b>	<b>95</b>
<b>5.2 SPUTTERING.....</b>	<b>95</b>
5.2.1 How Sputtering Works.....	96
5.2.2 Sputtering PVD 75 System.....	96
5.2.3 RF Sputtering Procedure.....	97
5.2.4 Recipe Controlled Deposition Example.....	100
5.2.5 Target Changing.....	101
5.2.6 Sputtering Parameters.....	102
<b>5.3 RAPID THERMAL ANNEALING PROCEDURE (RTA).....</b>	<b>103</b>
5.3.1 Thermal Stability.....	104
<b>5.4 PHOTOLUMINESCENCE (PL) PLATFORM.....</b>	<b>105</b>
<b>5.5 InGaAsP/InP Heterostructure.....</b>	<b>106</b>
5.5.1 Photoluminescence Map of the Wafer.....	106
<b>5.6 ETCH RATE ANALYSIS.....</b>	<b>107</b>
<b>5.7 RTA-ONLY RESULTS.....</b>	<b>107</b>
<b>5.8 RTA and Sputtering SiO<sub>2</sub> .....</b>	<b>108</b>
<b>5.9 PL COMPARISON.....</b>	<b>109</b>
<b>5.10 Al<sub>2</sub>O<sub>3</sub> Based QWI.....</b>	<b>110</b>
5.10.1 Sputtering Procedure.....	110

5.11.2 Sputtering Parameter.....	111
5.10.3 RTA.....	111
5.10.4 Etch Rate Analysis.....	111
5.10.5 PL Maps.....	112
5.11 SUMMARY.....	113
<b>6 CONCLUSIONS AND FUTURE WORK.....</b>	<b>115</b>
6.1 CONCLUSION.....	115
6.2 PERSPECTIVES AND FUTURE WORK.....	117
<b>REFERENCES.....</b>	<b>118</b>
<b>AUTHOR'S BIOGRAPHY.....</b>	<b>130</b>



## 1 General Introduction

### 1.1 Motivation of the work

Monolithic integration and wavelength agile lasers are the key technologies for the growth of advanced optical fibre networks. As the demand for bandwidth to deliver the next-generation of dynamic broadband services increases, the communications industry is faced with a paradigm shift. In the last twenty years, the information and communication technologies have developed at an alarming rate. The rapid growth of the World Wide Web and wireless technologies shaped the consumer market for new services such as the multimedia-over-IP, telemedicine, video on demand and software define network (SDN). Data centers of facebook and google have tremendously increased the bandwidth demand of the telecommunication and computer networks due to the accessibility of tons of multimedia files on the web. Since 1990, the global network traffic has been dominated by internet data and has grown at a staggering rate of 60% per year ineffective by new/old technologies [1]. The key feature to this explosive growth was the introduction of optical technology in the telecommunication industry.

Optical fibres have become the new ideal medium for data transmission, as they can transmit an encoded signal over long distances with minimal losses and without heat dissipation. Telecommunication systems with optical fibres still are commonly used for long distance communications and they require few interconnections and low flexibility. The capacity of optical fibre networks is increased due to the invention of wavelength division multiplexing (WDM). WDM allows transmitting multiple signals on various channels located at different wavelengths in one optical fibre. The implementation of WDM does not require many modifications to the existing fibre networks because different wavelengths do not interfere with each other. The transmission and reception units were required to be upgraded. New functionalities to the optical networks have been added due to the implementation of WDM technologies. For instance, specific channels could be allocated to various services. Today, commercial WDM systems can carry close to 10 Tbit/s over a single fiber, and research experiments have reached the 100-Tbit/s mark [1].

Figure 1.1 shows different applications that were defined by WDM grids. The L-band (1561-1620 nm) and the C-band (1528-1561 nm) are the commonly used grids. A variant of WDM technologies known as dense wavelength division multiplexing (DWDM) is used by these two grids. Telecommunication system involving long distances like inter-continental networks mainly use DWDM. The standard for DWDM networks are defined by the International telecommunication union (ITU). The standard grids consist of 32 to 160 channels, with an assigned spacing changing between 1.6 and 0.2 nm. In an extreme case, a system of optical transceiver with 128 channels requires 128 laser sources, 128 modulators, a string of coupling passive waveguides and an optical multiplexer to feed the multiplexed signal in the optical fibre channel.

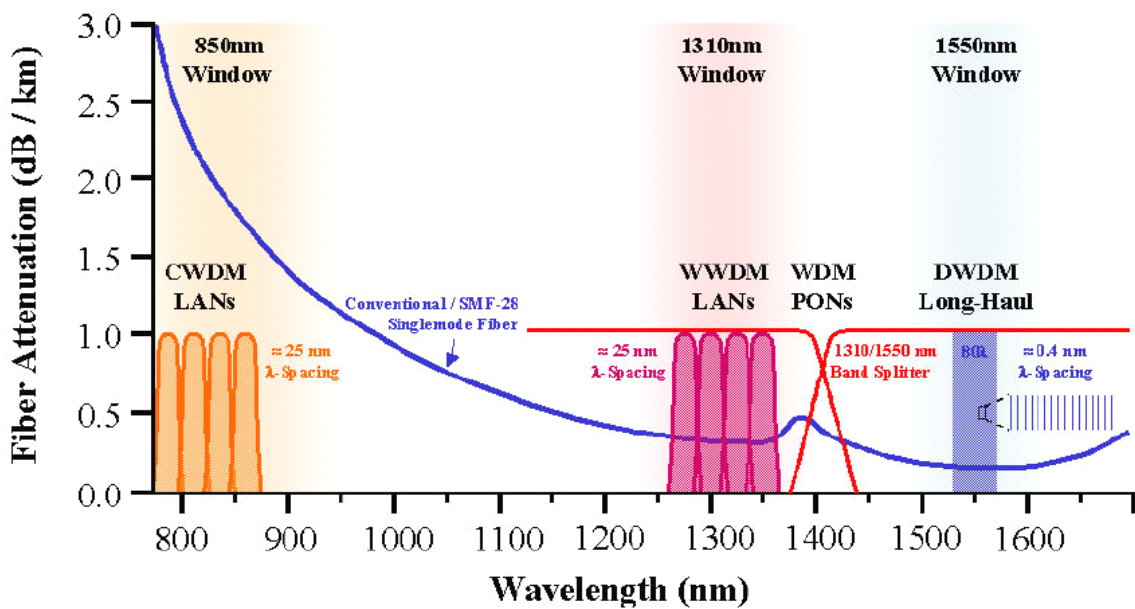


**Fig. 1.1 WDM spectral grids and blue line shows the attenuation in an ordinary SMF-28 fibre [2].**

Although, optical interconnections have great benefits, they only stand for 2% of the total number of interconnections and are mainly reserved for long distance communication [3]. The rest of the 98% interconnections are still made of copper and are dedicated to short distance communications. This includes distances ranging from computer-to-computer and chip-to-chip as shown in Figure 1.2. Nevertheless, with the availability of new online services and the increased demand of the bandwidth, interconnections based on copper are required to be denser and the problems linked with heat dissipation and electro-migration are expected to arise. In this situation,

short distance optical communication becomes more attractive. That is the reason why much research is conducted on WDM-based short distance access networks. High cost related to the installation of optical systems entails their limited use. It costs only few cents to build a copper based interconnection whereas the installation of an optical transceiver costs between few hundreds to few thousand dollars. Consequently, telecommunication companies tend to limit their installation on optical routes where huge amount of data transferred from point A to point B. Further, they are searching for alternatives such as silicon based optical transceivers. Scientific community have had some successes in developing silicon based photo detectors, optical multiplexers, filters, switches, amplifiers, modulators and waveguides but we are still a distance away from developing silicon based optical laser source. Therefore more research needs to be done to come up with cost-effective solutions that can make optical communication affordable for any compute platform, revolutionizes applications and architecture.

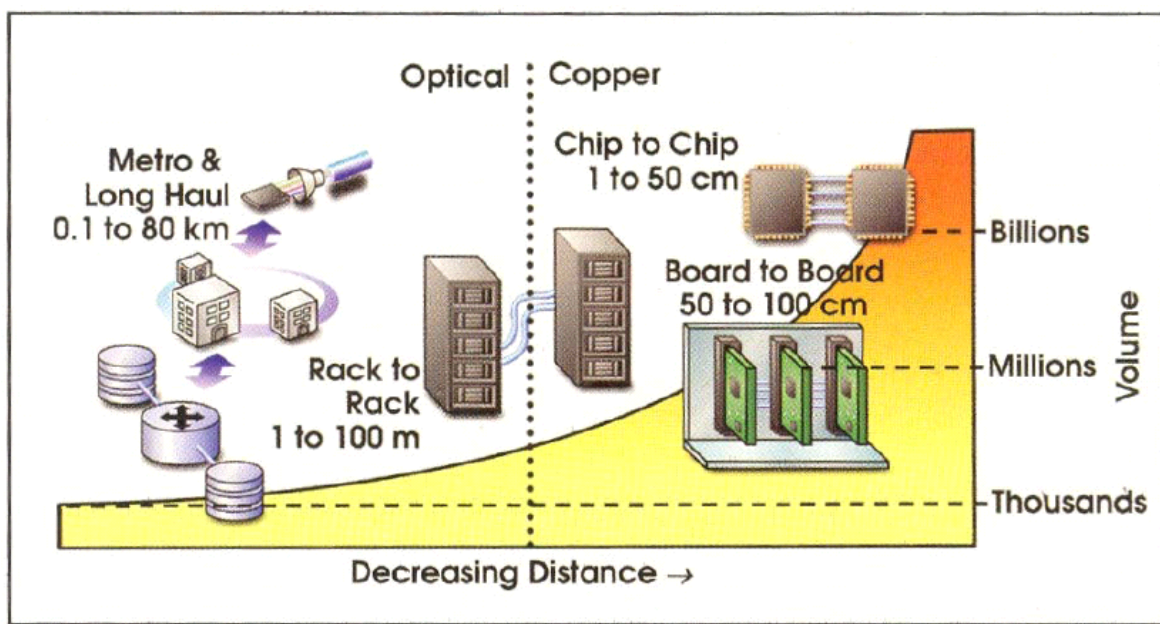


**Fig. 1.2 Volume of interconnections versus the distance over which data get transmitted [2].**

Since 1970s, key features in electronics like micro-processor speed and memory density have doubled every 18 months and it is known as the Moore's law [4]. This is mainly due to the advancement of microelectronic integration technologies. Integrating various devices on a single chip not only facilitate to cut the size and the cost of every component but also allowed the mass manufacturing of integrated

circuits. Moreover, new functionalities can be recognized by increasing the complexity and the devices density on a chip. This was impossible with a few discrete electronic devices. This progress has allowed the steady enhancement of devices performance as systems were effectively kept at a constant price.

Encouraged by the microelectronics model, researchers have previously tried to fabricate photonic integrated circuits (PICs) with partial success. PIC is a part of optoelectronics circuits (OEICs) technology using a single substrate for the monolithic integration of optoelectronic devices. Mainly OEIC fabricated today have been designed to satisfy the requirements of conventional point-to-point optical link. In this case, the optical device works as a terminal device that converts a processed electrical signal into an encoded optical signal for optical fibre communication, or vice versa. In comparison, PIC include optically interconnected devices that redirect, condition, or process the signal while in its optical domain. The motivation behind the enhancement of PIC is the expected intricacy of next-generation optical communication link, architectures of networks and advanced switching systems.

A reason for high cost of such architectures is the difficulty of realizing single mode optical connections between guided-wave components. For optimized performance, such devices often require highly accurate waveguides, resulting in delicate sub-micrometer alignment when coupled to single mode optical fibers. By replacing separately aligned connections with lithographically formed passive waveguides, PICs can lead to cost reduction, dramatically compact size, simplify mechanical designs, cuts the coupling steps between the various components and improved packaging robustness [5].

In 2002, Jeremy Mills predicted that the encapsulation of devices was linked to the 70- 90% fabrication costs of the photonic devices [6]. This suggests that, it is a quite attractive option to incorporate many components in one package .The optical and electronic properties of the devices will also be improved by such integration. For instance, the losses associated with optical interconnection between separate devices will be diminished. The parasite inductances will also be reduced by bringing the electronic control circuit close to the modulator which would then let the modulators to function at elevated frequencies.

Let us look at an example of a simple PIC illustrated in Figure 1.3. In this PIC, passive transparent optical waveguides carry the light signal to different active optoelectronic devices within the same plane of the QW wafer. The bandgap energies of different components should be related to each other in a particular fashion to ensure optimum performance. For instance, in Figure 1.3, it is necessary that the passive waveguide gathering and distributing the light signal from the laser diode must be as transparent as possible to the laser wavelength (i.e., have a larger bandgap energy than that of the laser source) so that during transit, little amount of optical power is vanished to absorption [5].

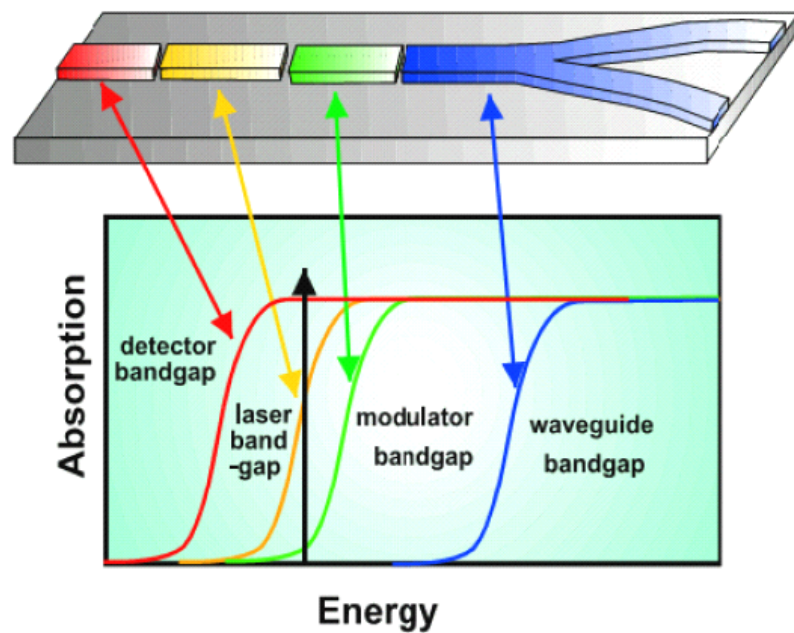


**Fig. 1.3 Schematic diagram of a PIC that contains laser diode whose light is injected into a transparent waveguide 3-dB splitter via an external electroabsorptive modulator. The optimum operation of this PIC necessitate that the bandgap energies of three components should have a specific relationship shown in the Figure<sup>[5]</sup>.**

## 1.2 PIC Fabrication Techniques

Till today, mainly two approaches have been used to fabricate different photonic active and passive components on a single substrate. The first technique utilizes the hybridization of various components i.e., individually fabricated devices are mounted on a supporting substrate as shown in Figure 1.5. The second approach comprises of fabricating all the photonic devices straight from single wafer. This technique is known as the monolithic integration. It is vital that these two techniques are not

exclusive. These techniques can be used simultaneously to a different extent for the production of a complex photonic integrated circuit (PIC).

Figure 1.4 shows the relation between the densely integrated photonic devices, the production volume and the maturity of manufacturing technologies. With the increase of the production volume and hence due to lower fabrication costs, the hybrid and monolithic solutions become more and more attractive. On the other hand, complexity hinders the progress towards increasing the density of monolithically integrated devices. This is simply due to the reason that designs of complex devices make it harder to achieve the levels of standardization and volume production desired to move to the next phase [6].

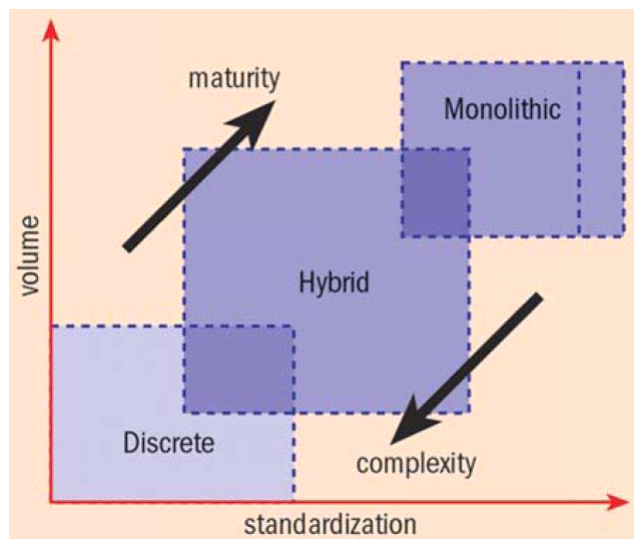


**Fig. 1.4 Densely integrated devices become the new standard with mature technology and it increases production volume [6].**

### 1.2.1 Hybrid Integration

A comparison with electronic device manufacturing process can be made by an example of a printed photonic circuit where different discrete components of a transceiver are coupled together on a PCB, as shown in Figure 1.5. The substrate contains passive transparent waveguides which work like data buses between the active components. It presents hybrid silicon lasers integrated with modulators for data encoding and a multiplexer to put four optical channels onto a single fiber. Data rate of 50Gbps scaleable to 1Tbps is achievable. One of the recent advances of this approach was achieved in 2012 by Justin Rattner and his colleagues [7-9] and is being developed for the telecom market by Intel. They laminated a number of laser diodes

on a silicon substrate on which modulators and waveguides were patterned earlier, as shown in Figure 1.6. The significant advantage of this approach is the employment of substrates for devoted applications. The electronic circuit can be fabricated using standard CMOS process on a silicon substrate and similarly the laser diodes can be fabricated on III-V semiconductors QW structures. Therefore, mounting many devices made out of different materials on a single substrate can be demanding, particularly if light requires to be coupled from a high index QW material, such as III-V semiconductor, to a lower index material, like silicon.

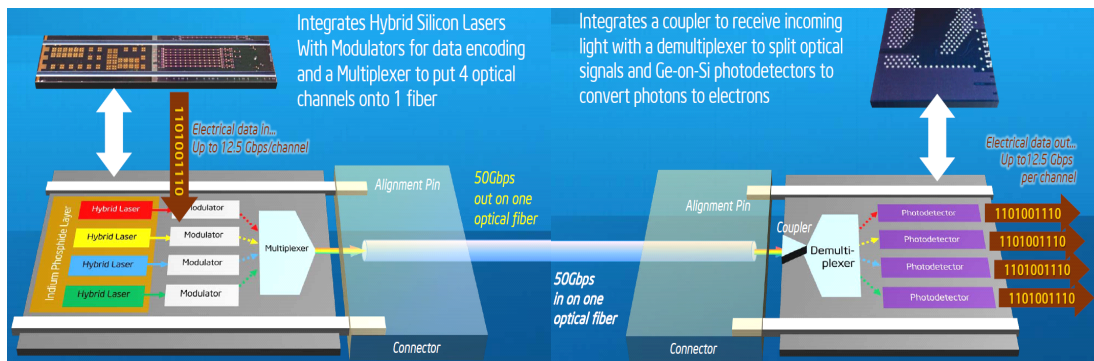


Fig. 1.5 Schematic of a complex hybrid PIC [70].

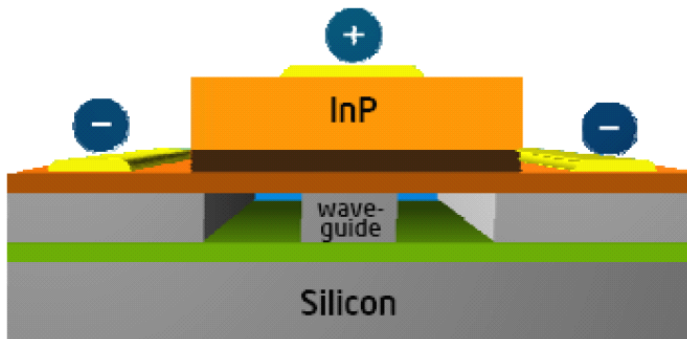
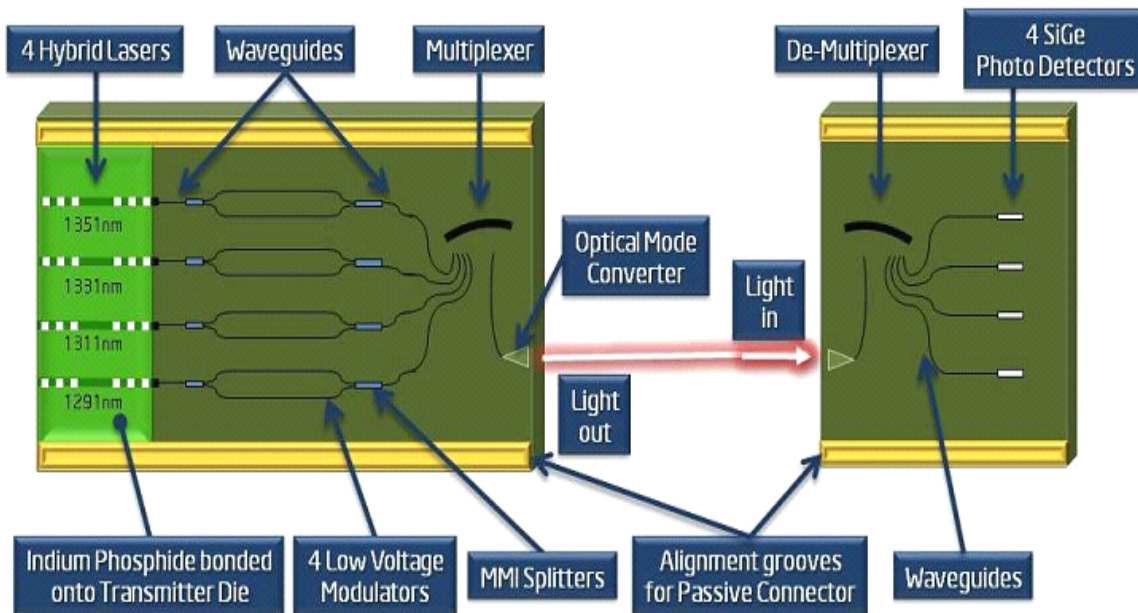


Fig. 1.6 Cross section view of the hybrid silicon laser [9].

Fig. 1.7 shows one of the examples of fabricated device using hybridization method. It shows four hybrids InP based lasers coupled with four Si waveguides and on the receiver side demuxle using etched diffraction gratings are coupled with four SiGe detectors. The system operates at 12.5Gbps per channel and demonstrates a 50Gbps aggregate bandwidth for silicon photonics link [9].



**Fig. 1.7 Schematics of the integrated 4-channel CWDM Silicon photonic transmitter (left) and receiver (right)<sup>[10]</sup>.**

### 1.2.2 Monolithic Integration

The monolithic integration technique has been used effectively in the production of simple photonic integrated devices. Laser diodes integrated with modulators are available commercially, as shown in Figure 1.8. By using monolithic integration technique, much denser integration and more robust systems can be realized as compared to the hybrid ones, as same substrate material is used to make different devices. In this case, it is much easier to couple light signal between different devices. However, monolithic designs, frequently experience very low yields. As we desire, lossless, reflection less transitions between different sections of the PIC.

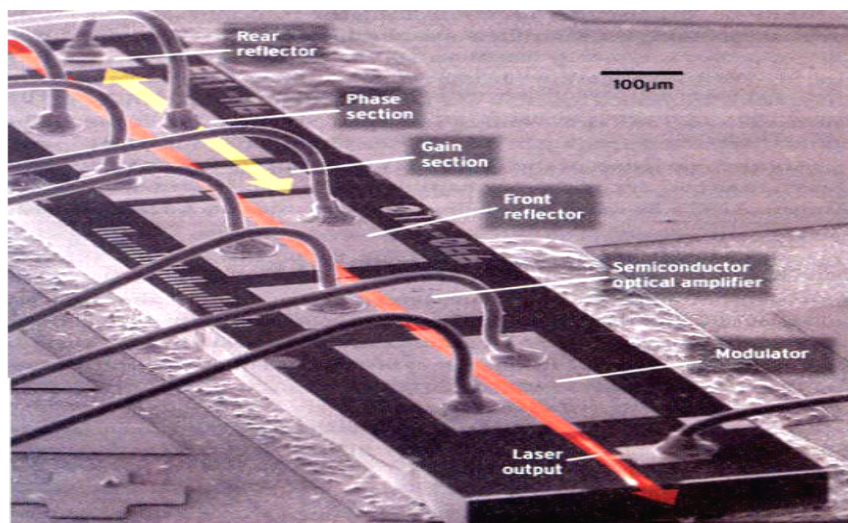


**Fig. 1.8 Monolithically integrated photonic device example that shows a wavelength-agile laser is integrated with modulator<sup>[11]</sup>.**

It is very important to be able to locally modify the actual properties of the QW substrate. Today, most of the monolithically integrated photonic devices are made by utilizing one of the techniques such as Vertical twin-guide, Butt-joint Re-growth, Selective area growth, off set quantum well, Dual quantum well and Quantum well intermixing as shown in Figure 1.9.

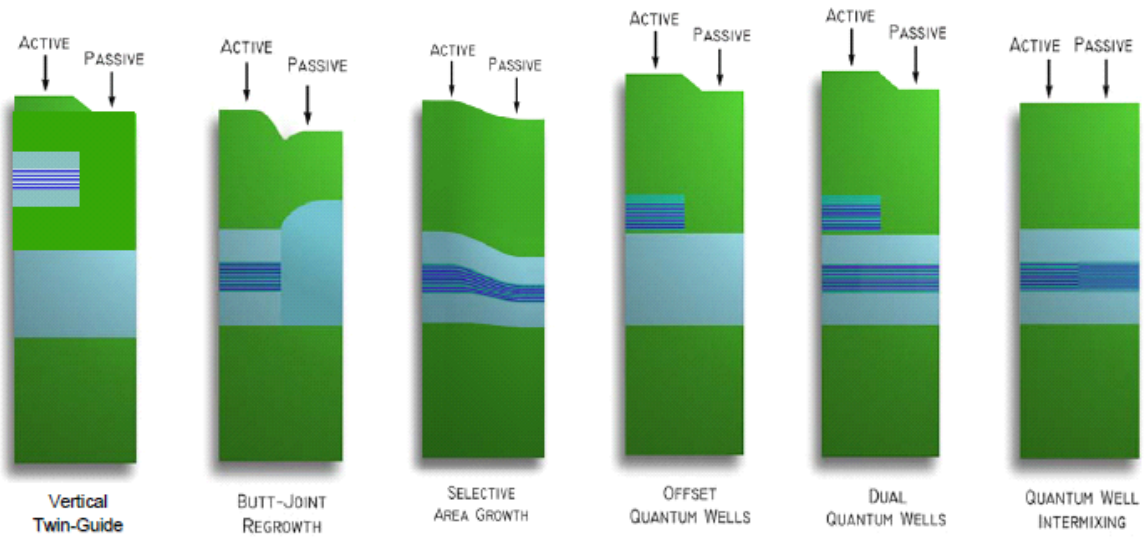


**Fig. 1.9 Various techniques for attaining active and passive regions orthogonal to the growth direction [12].**

The majority of the PIC devices fabricated today are based on multiple epitaxial growths. This implies that after the first growth, the sample undergoes lithography and etching steps before putting the sample back again in the epitaxial reactor to do a second growth (Figure 1.10).

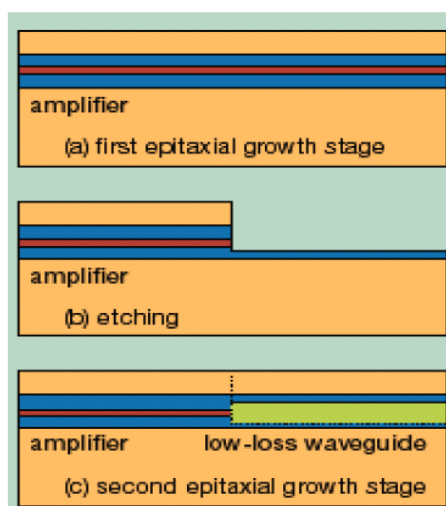


**Fig. 1.10 Principal steps needed to fabricate an active/passive waveguide from a QW structure [13].**

Since multiple epitaxial growths is a lengthy process, further the etching techniques can produce a considerable number of defects at the surface and edges of the processed wafer. Therefore such technique yields low production output and can be expensive. The defects implanted in the interfaces of the QW material created during etching methods often cannot be removed throughout the successive growth and these defects become liable for diminishing the feature of the fabricated device.

If a post-growth method is developed then the problems linked with the cost, low throughput and quality of the wafers produced by etchings and multiple epitaxial growths can be relieved. That would permit the fabrication of wafers with tangentially modulated properties. In that situation, quantum well intermixing (QWI) is one of the most promising techniques [14]. This procedure addresses QW structure used to manufacture active and passive integrated photonic devices. It modifies the bandgap by inducing atomic inter diffusion between the well and barrier of the QW materials [14-16]. This is due to the heterogeneity in the composition of the QW layer structure, as shown schematically in Fig. 1.11. This process in general, increases the bandgap energy by rounding of the originally square QW bandgap profile. This provides a way to produce low-loss transparent optical waveguides, and bandgap shifted modulators integrated with laser sources and photo detectors, by only using single epitaxial step. Furthermore, due to increase in the bandgap, the refractive index is customized enough to offer better optical confinement, gratings and reflectors.

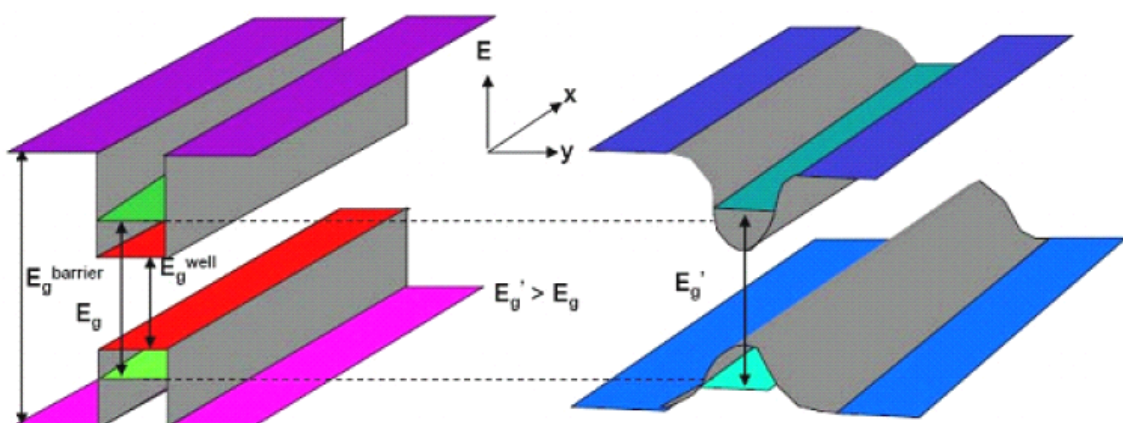


**Fig. 1.11 Schematic diagram illustrating QW shape modifications of the QW bandgap energies.**

However the QWI technique also has some disadvantages in comparison to regrowth and etching steps. As it will be explained later, QWI is associated with the

diffusion of point defects. These point defects require to be generated and the method used to achieve this can harm the QW structure making it unfit for device fabrication. The left over point defects created by QWI can also affect the optical and electrical properties of the device. The spatial resolution of the QW intermixing process also needs to be investigated because the diffusion of point defects is isometric most of the time. The spatial resolution subsequently depends on the quantum well depth.

### **1.3 Project Description**

This research work explores the post-growth selective QWI techniques using UV-laser,  $\text{SiO}_2$  and  $\text{Al}_2\text{O}_3$ . It explores new methods to overcome known deficiencies and also presents applications of UV-QWI technique for photonic devices that could lead to photonic integrated circuits. It aims at developing a novel expertise of QWI for alteration of bandgap properties of QW structures and controlled creation of point defects vital for improved intermixing of the QW and barrier materials that stand on the application of UV excimer lasers. The objective is to examine the potential of such a technique in developing a well controllable and reproducible procedure capable of fabricating monolithically integrated photonic devices using III-V semiconductors technologies. This desirable technique should also be compatible with the existing micro-fabrication processes.

Lasers are a highly useful tool for post-growth processing of semiconductor wafers due to their versatility. A laser can be utilized for local heating of the semiconductor QW structure [17,18] based on the emission wavelength and duration of pulse, causing thermal shock which generates point defects close to the surface of quantum well [19] or alter the surface chemistry [20- 23]. All these things have an instant consequence on the point defects diffusion and therefore on the QWI process. The main objective of this research work is to study and demonstrate a practical UV-laser based QWI technique in InGaAsP/InP laser structures, and to apply the UV-laser QWI technique for the fabrication of photonic devices. We also studied and demonstrated post-growth alternative QWI techniques based on sputtering  $\text{SiO}_2$  and  $\text{Al}_2\text{O}_3$  that can also selectively control bandgaps in standard InGaAsP/InP laser structure.

The main innovations and findings of this thesis work can be summarized as follows:

1. Developed experimentally UV-laser induced quantum well intermixing and applied it first time in strained multiple quantum well (MQW) structure. Obtained larger blue shift (over 142 nm) as compared to unstrained MQW, while the PL peak intensity becomes even higher with narrower full width at half maximum (FWHM).
2. Fabricated passive optical waveguides using UV-laser induced quantum well intermixing in InGaAsP/InP quantum well structure. The loss of the waveguide for 1545nm light drops from 110dB/cm to 20dB/cm.
3. Fabricated Fabry-Perot cavity lasers with blue-shifted lasing wavelength of 1435nm using UV-laser induced quantum well intermixing in InGaAsP/InP strained quantum well structure and obtained a lower threshold current and a large output power.
4. Implemented the Argon plasma induced QWI during the sputtering of SiO<sub>2</sub> in standard InGaAsP/InP compressively strained multiple quantum well structure and systematically studied the relations of RF power, annealing temperature to the altered quantum well PL peak blue-shift and PL intensity.
5. Proposed and investigated Al<sub>2</sub>O<sub>3</sub> plasma induced quantum well intermixing technique in InGaAsP/InP multiple quantum well structure with and without sacrificial layer for the first time, and obtained over 110nm blue-shift.

This research allows the improvement of knowledge on the fundamental physical mechanisms involved in UV-QWI laser controlled QWI method. It demonstrates the viability of UV excimer based QWI in realizing sub-micrometer level microstructures. Lastly the developed expertise permits the fabrication of optoelectronic, photonics and micro/nanostructures compatible with the adopted fabrication processes of the industry.

A review of the theoretical concepts related to QW and laser interaction with matters is presented in chapter two. It explains the electronic characteristics of

semiconductor QW structures and how mechanical strain influences their properties. Particular attention is given to laser based desorption and capability of a laser to change chemical composition of exposed surface of the InGaAsP/InP laser structure.

Chapter three provides assessment of the techniques used for PIC and presents the current progress in the QWI approach. It introduces the QWI concept and describes the most common intermixing techniques used for photonic integrated circuits. This chapter also discusses stressed field of the QW structure in context with point defects diffusion.

Chapter four presents experimental procedures required to conduct UV-laser based QWI. The chapter explains the characterization techniques and also analyses the results of UV-QWI in InGaAsP/InP laser structures. It contains an article, “UV laser induced selective-area bandgap engineering for fabrication of InGaAsP/InP laser devices”, published in April 2013 [23]. This chapter also discusses the results of fabricated low loss waveguides and FP-laser diodes using UV-QWI technique.

Chapter five presents an alternative QWI techniques based on sputtering SiO<sub>2</sub> and Al<sub>2</sub>O<sub>3</sub>. The chapter also explains the experimental methods used to achieve the goals of this thesis. The sputtering setup along with RTA process and then the results of QWI controlled by sputtering SiO<sub>2</sub> and then by Al<sub>2</sub>O<sub>3</sub> in InGaAsP/InP laser structures are discussed. To analyze the optical and electrical properties of the altered material, the characterization techniques used for this purpose are also presented.

Chapter six discusses the directions of future work and presents the over all conclusions of this thesis.

## **2 Theory of Energy Band Structure and Interaction of Light with Semiconductors**

### **2.1 Introduction**

This chapter presents an assessment of physics principles essential to appreciate the extent and the connotations of my thesis work. The first section of the chapter describes the bands structure in semiconductor multiple quantum wells. Moreover, I also explain how recombination of charge carriers can result in the release of light and how this procedure is affected due to the existence of point defects, impurities and mechanical strain. InGaAs quantum well example is used to explain these concepts.

The second part of this chapter illustrates the interaction of a laser light with semiconductor materials. I introduce the light absorption processes and give details of the various desorption and ablation mechanisms.

### **2.2 Energy Band Structures in Semiconductors**

The energy band structure of each crystal is different. This trait explains a variety of optical and electrical characteristics in various materials. We can divide solids into three individual categories based on the relative location of the conduction and valence bands, i.e., metals, semiconductors and insulators.

Metal (Figure 2.1a) valence and conduction bands lie on top of each other or are only partially filled. It means that conduction band electrons are at the same energy level to that of empty energy states. Therefore in the presence of an external force, they can move without restraint. While in semiconductors and in insulators, the energy bands are separated by an energy gap  $E_g$  unfilled of available energy states. Hence, the bandgap is a kind of an energy barrier that an electron desires to overcome in order to jump to the conduction band where it can add to the electric conduction. At 0K temperatures, electron is not present in the conduction band of semiconductors or insulators (Figure 2.1b and c). These two categories of materials (semiconductors and insulators) differ on the basis of their bandgap sizes. In principle, materials with

bandgap lower than 2 eV are known as semiconductors whereas insulators have larger bandgap [24]. A semiconductor with relatively small bandgap permits the excitation of electrons to the conduction band by a realistic amount of thermal or optical energy.

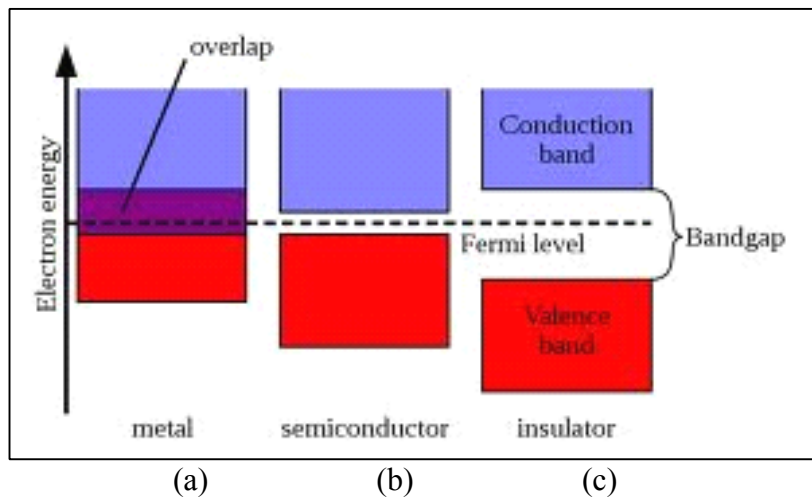


**Fig. 2.1 Typical bands profiles at 0 K for a: an insulator, b: a semiconductor and c: a metal [24].**

The couplings of the electronic orbitals in a crystal are directly linked to the arrangement and the position of the bands. All fundamental semiconductors (germanium, silicon and carbon) can be located in the fourth column of the Mendeleev's periodic table and all of them have a crystalline structure analogous to that of a diamond. Compound semiconductors consist of elements that, when combined together, have a mean amount of valence electrons equivalent to four. These compound semiconductors either consist of atoms taken from the third and fifth columns of the periodic table (III-V semiconductors such as GaAs, GaSb, GaP, InAs, GaN, InSb, InP, InN, AlP, AlSb, AlAs, AlN), from the second and the sixth columns of the periodic tabel (II-VI semiconductors like ZnO, ZnSe, ZnS, CdS, ZnTe, CdTe, CdSe, HgSe, HgS, HgTe), from the forth group (IV-IV semiconductors such as SiC, SiGe, ...), or fewer known semiconductors from the second and the fifth groups (II-V semiconductors as Zn<sub>3</sub>As<sub>2</sub>, Cd<sub>3</sub>P<sub>2</sub>, Cd<sub>3</sub>As<sub>2</sub>, ...). The mixture of more than one binary compounds leads to the formation of ternary and quaternary compound semiconductors like AlGaAs, InAlGaAs, InGaAsP and InGaAs.

An additional distinct property of all known semiconductors is their band diagram. It describes the location of the energy states against the carriers' wave vector  $k$  (Figure 2.2), or carriers' momentum.

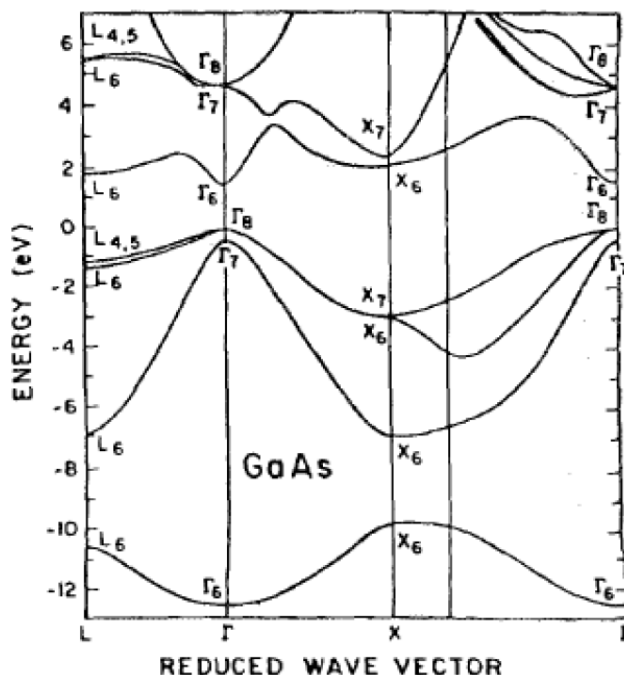


**Fig. 2.2 Electron energy of GaAs versus the reduced wave vector of the four valence bands and first conduction bands [25]. The energy origin is set at the maximum of heavy-light holes.**

In the majority of semiconductors, the valence band maximum is situated at the  $\Gamma$  point of the Brillouin zone. Each valence band has three branches, i.e., the heavy holes, light holes bands, which lie on top of each other at  $k = 0$ , and the spilt-off band, which maximum also occurs at  $k = 0$ , but at different energy. At different values of wave vector, the conduction band minimum can be positioned. A semiconductor has a direct bandgap (Figure 2.3a) if the conduction band minimum and the valence band maximum are placed at the same wave vector position. This is normally the case with majority of III-V and II-VI compound semiconductors. In contrast, if there is a momentum difference between the position of the conduction band minimum and the valence band maximum, the gap is then considered as indirect (Figure 2.3b). This is the case in elemental semiconductors (Si, C and Ge) and in some III-V compounds like AlP, GaP, AlAs and AlSb.

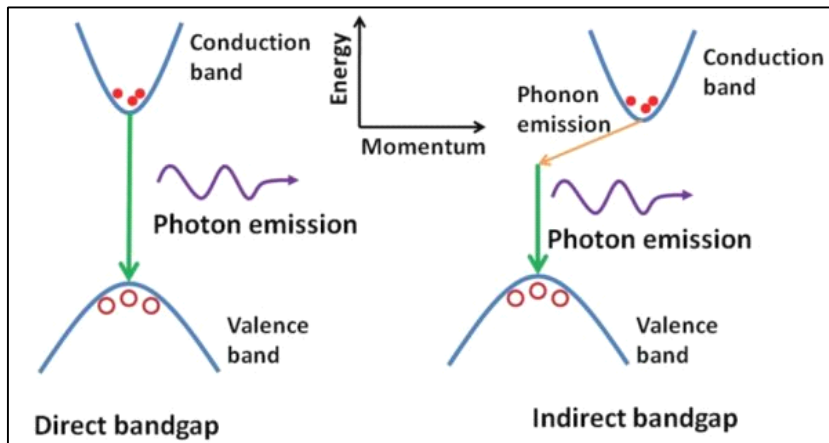


Fig. 2.3 a: Direct and b: Indirect bandgaps in semiconductor [24].

### 2.3 The Quantum Well

The quantum well is made of a successive stacking of various materials. The important feature of the quantum well depends on the QWI process. The well is created if a comparatively small bandgap material (e.g. GaAs) is squeezed between two larger bandgap materials also called the barriers (e.g. AlGaAs) as shown in Figure 2.4. The charge carriers intend to travel toward the central region to minimize their energy. Because the thickness of the well is of the order of electron's wavelength within the material, the well limits the moves of the charge carriers in the growth direction. The discretisation of the energy levels within the well is due to the confinement of the charge carriers.

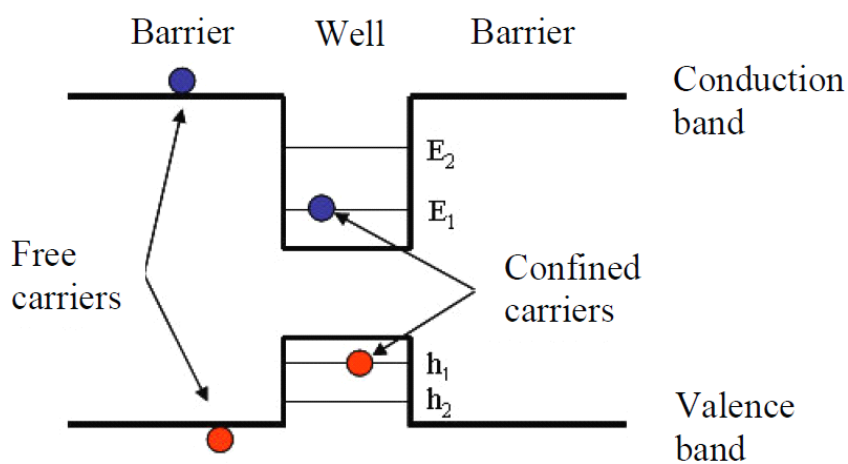
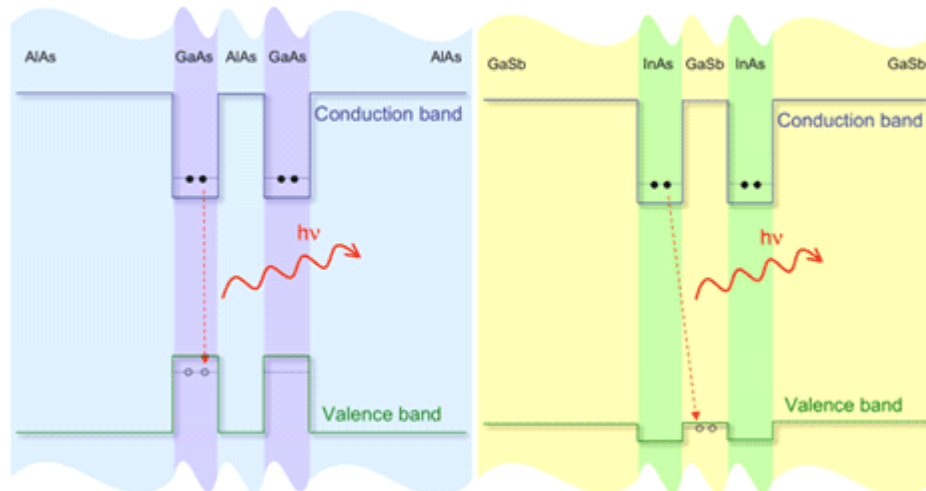


Fig. 2.4 Schematic of a type I QW band structure

The levels position relies on the composition of the material and on thickness of the well. Furthermore, a quantum wire confines the charge carriers in two dimensions whereas a quantum dot limits the charge carriers in three dimensions.

The electronic affinity defines the relative location of the valence band of two dissimilar materials. It also decides the quantum well type. A quantum well of type I confines both electrons and holes in the middle section, whereas a type II only confines one type of charge carrier (Figure 2.5). Since both of carriers are confined in the well layer in case of type I quantum wells therefore they are the only ones allow direct inter-band recombination. Hence, type I quantum well structures are mainly used for photonic applications in near/mid infrared and the visible wavelengths. Type II quantum wells photonic applications are typically based on intra-band transition that leads to the release of far infra-red photons. However, in our research work only type I quantum wells are used implicitly.



**Fig. 2.5 quantum well type I and type II heterostructures**

## 2.4 Charge Carriers Recombination

We require using indirect methods because it is not possible to directly calculate the band structure of a material. Majority of these methods (transmission, absorption and luminescence etc) depend upon on the interactions between charge carriers and photons. We differentiate between three kinds of interactions i.e., absorption, spontaneous emission and stimulated emission. Absorption occurs when a photon passes on its energy ( $E_{ph}$ ) to an electron, causing it to jump from its original state  $E_1$  to

a new state  $E_2$  on a higher energy level, therefore  $E_{ph} = E_2 - E_1$ . It is very important that the  $E_2$  state must be empty for the absorption to happen. In semiconductors, if the photons energy is larger than the bandgap energy, nearly all transitions happen as electrons leap from the valence band to the conduction band [24]. The existence of a carrier vacancy in the valence band notices the molecular orbitals which produce a quasi-particle i.e., the hole (Figure 2.6a). Spontaneous emission is the opposite process of absorption. An electron relaxes through the release of a photon of energy  $E_{ph} = E_2 - E_1$  as shown in figure 2.6c. As photons have almost zero momentum, this transition cannot be completed with a modification in the carrier momentum. This means that indirect bandgap material such as silicon cannot release light during an electron- hole simple recombination. This can only be achieved with the help of a third particle with non-zero momentum like phonon. Because it involves the collision of three particles, the likelihood of an indirect transition is comparatively small compared to relaxation via direct radiative processes.

Since the likelihood of taking place a collision with a phonon is bigger than the chance of recombination, therefore when an electron is energized to the upper levels of the conduction band, its energy is decreased during interaction with the vibration of the crystal until it arrives at the bottom of the conduction band (Figure 2.6b). Lastly, if a photon with energy  $E_{ph} = E_2 - E_1$  passes in the surrounding of an electron at the energy level  $E_2$ , then the photon can encourage the electron-hole recombination. This results in the release of a 2<sup>nd</sup> photon with equal energy, polarization, phase and direction of the first one. The last transition is known as stimulated emission. In comparison, photons released through the process of spontaneous emission contain random phase and direction. A schematic of absorption, stimulated emission and spontaneous emission in a system having two energy levels is shown in figure 2.7.

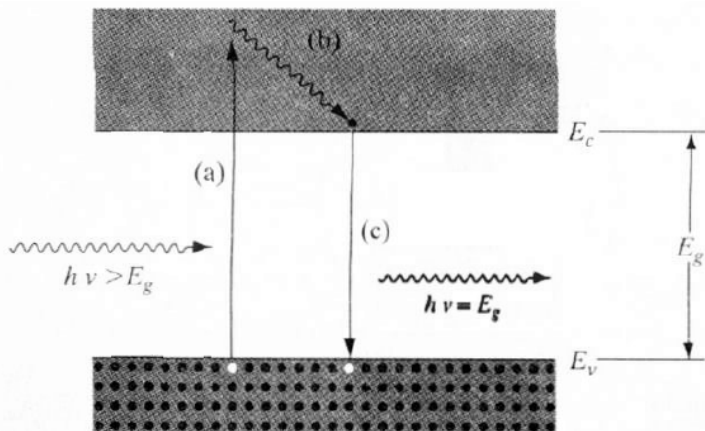


**Fig. 2.6 Absorption of a photon  $h\nu > E_g$**  a: Electron flies to conduction band and leaves a hole in the valence band b: electron decreases its energy through collisions with phonons c: electron-hole recombination and emission of a photon  $h\nu = E_g$  [24].

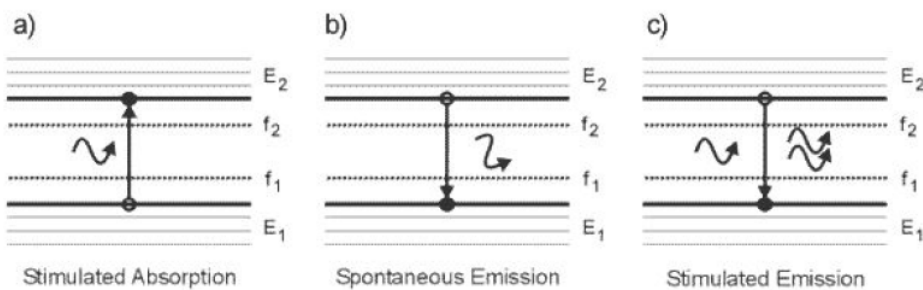


**Fig. 2.7 Photon-electron interactions in a system with only two energy levels, a: absorption, b: spontaneous emission and c: stimulated emission** [26].

The electron wave function also depends on defects and impurities within the material. This generates available energy levels, a few of them within the material bandgap. The associated relaxations processes can be radiative or non-radiative. If the location of the energy level of impurities is very close the minimum of the conduction band or the valence band maximum, then it is essential to examine the semiconductor material using low temperature to differentiate transition associated with impurities from the inter-bands one.

## 2.5 Strain and Stress

The material's band structure has direct relationship with the strain and stress. The confinement profile and the energy bandgap can be changed by applying stress field on the semiconductor QW structure.

Ahopelto used these phenomena to fabricate strain induced quantum dots using InGaAs/GaAs quantum well structure [27]. Strained QW structures are also utilized to produce laser diodes of low threshold current due to the lower effective mass of the charge carriers in the stressed materials [28].

### 2.5.1 Strain

We describe strain ( $\epsilon$ ) as the deformation of a material from its equilibrium position. Generally, if we assume a deformation vector  $\vec{u}$ , then linear strain becomes

$$\epsilon_{ii} = \frac{\partial u_i}{\partial x_i}, \text{ for } i = 1, 2, 3 \text{ Where } x_1 = x, x_2 = y \text{ and } x_3 = z, \quad (2.1)$$

and the shear strain becomes:

$$\epsilon_{ij} = \frac{1}{2} \left[ \frac{\partial u_i}{\partial x_j} + \frac{\partial u_j}{\partial x_i} \right], \text{ for } i \neq j. \quad (2.2)$$

Where  $\epsilon_{ii}$  and  $\epsilon_{ij}$  are components of the strain tensor  $\epsilon$ . The existence of an exclusive shear strain does not modify the material volume as linear strain occurs in compression or dilation. We describe the material dilation as  $\text{div } \vec{u}$ :

$$\overset{\rightarrow}{\text{Div }} \mathcal{U} = \epsilon_{xx} + \epsilon_{yy} + \epsilon_{zz} \quad (2.3)$$

### 2.5.2 Stress

Stress is the force linked to an elastic distortion:  $\vec{F} = -\text{div}(\sigma)$ . While for strain, we define

$$\sigma = \begin{bmatrix} \sigma_{xx} & \sigma_{xy} & \sigma_{xz} \\ \sigma_{yx} & \sigma_{yy} & \sigma_{yz} \\ \sigma_{zx} & \sigma_{zy} & \sigma_{zz} \end{bmatrix} \quad (2.4)$$

Strain and stress associated with each other via the Poisson ratio  $\nu$ , Shear modulus  $C'$  and the Young modulus  $Y_0$ ,

$$\epsilon = \frac{1}{Y_0} [\sigma_{xx} - \nu(\sigma_y + \sigma_z)] \quad (2.5)$$

$$\varepsilon_{xy} = \frac{\sigma_{xy}}{2c'} = \frac{(1+\nu)\sigma_{xy}}{\gamma_0} \quad (2.6)$$

Expression (2.5) and (2.6) can be generalized for all components of the strain tensor  $\varepsilon$ .

We can differentiate between two specific stress configurations. The hydrostatic stress has similar linear components i.e.,  $\sigma_{xx} = \sigma_{yy} = \sigma_{zz}$  and has no shear component. The strain counterpart has a diagonal matrix with all non-zero components

$\varepsilon_{ii} = \sigma_{ii}(1 - 2\nu)/\gamma_0$ . The biaxial stress tensor is

$$\sigma_{biaxial} = \begin{bmatrix} \sigma_{\perp} & 0 & 0 \\ 0 & \sigma_{\perp} & 0 \\ 0 & 0 & 0 \end{bmatrix}, \quad (2.7)$$

Where  $\sigma_{\perp}$  is the strain component in the plane of material, vertical to the growth direction. The consequent strain tensor is

$$\sigma_{biaxial} = \frac{1}{\gamma_0} \begin{bmatrix} \sigma_{\perp(1-\nu)} & 0 & 0 \\ 0 & \sigma_{\perp(1-\nu)} & 0 \\ 0 & 0 & -2\sigma_{\perp} \end{bmatrix} \quad (2.8)$$

### 2.5.3 Effect of Strain on the Band Structure of a Crystal

The main consequence of strain is mechanical i.e., the sample bends just like an ordinary bimetallic strip. By using atomic force microscopy (AFM) or scanning tunneling microscopy (STM), surface deformation can be calculated to find out the local strain values in a well-known material [29]. When the strain is quite large, it will also force samples to crack or devices to fail. Microscopically, strain influences the band structure. It moves the conduction and valence band and it changes the trapping rate of charge carriers and excitons by altering their effective masses [29]. It also affects the refractive index of the material and can make birefringence.

In case of direct bandgap, at the  $\Gamma$  position of the Brillouin zone, dilatation reduces the material bandgap by shifting the conduction band and valence band nearer to each other. Dilatation  $\operatorname{div} \vec{u}$  decreases the location of the conduction band  $E_c$  such that

$$\Delta E_c = \alpha_c \cdot \operatorname{div} \vec{u} \quad (2.9)$$

Where  $a_c$  is the distortion potential of the conduction band, typically it is -5 to -10 eV.

The position of the conduction band increases due to compression. Likewise, dilation also influences the position of the valence band. Nevertheless, this change is adjusted by the strain induced variation from the crystal cubic symmetry [30]. We describe the axial strain  $\epsilon_{ax}$  as a deviation from hydrostatic strain:

$$\epsilon_{ax} = \epsilon_{zz} - \frac{1}{2}(\epsilon_{xx} + \epsilon_{yy}) \quad (2.10)$$

Next we define the changes of the heavy holes band  $\Delta E_{hh}$  and the light holes band  $\Delta E_{lh}$  positions as

$$\Delta E_{hh} = a_v \cdot \vec{div} \cdot \vec{u} - b_v \epsilon_{ax} \quad (2.11)$$

$$\Delta E_{lh} = a_v \cdot \vec{div} \cdot \vec{u} + b_v \epsilon_{ax} \quad (2.12)$$

Where  $a_v$  represents the distortion potential for the valence band and  $b_v$  is for the axial distortion potential. Expressions (2.11) and (2.12) explain that breaking of the crystal cubic symmetry elevates the heavy and light holes bands degeneracy at the  $\Gamma$  position of the Brillouin zone. Therefore due to negative axial strain (tensile biaxial strain), the light hole band becomes minimum in energy as shown in figure 2.8. It modifies curvature of the holes' band in the various wave vector  $k$  directions, as illustrated in figure 2.9 that alters the effective mass of the heavy and light holes.

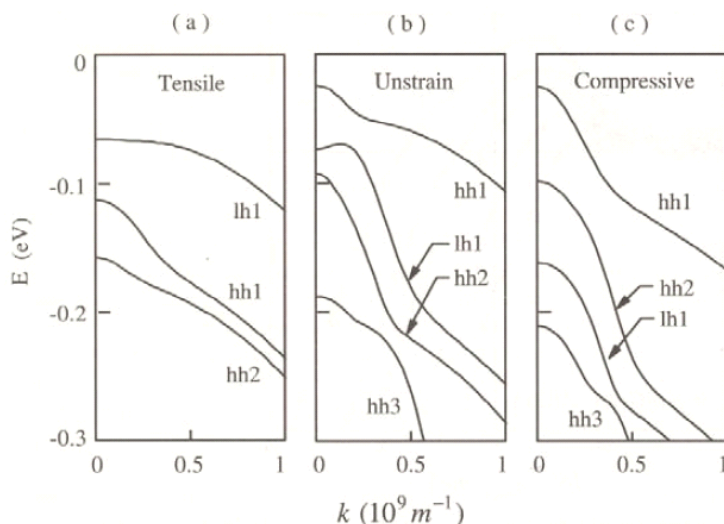


**Fig. 2.8 Heavy and light holes bands in 5 nm In<sub>x</sub>Ga<sub>1-x</sub>As/InP QW for various biaxial strain configurations. The strain is restricted by selecting indium composition in the well, a: tensile**

**strain,  $x = 0.33$ , b: lattice matched on InP,  $x = 0.53$ , c: compressive strain,  $x = 0.73$  [31].**

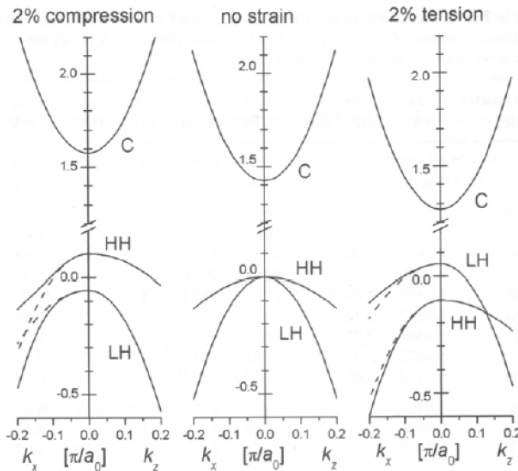


**Fig. 2.9 Raise of the heavy and light holes bands wickedness at  $\Gamma$  position and vary in band curvature under axial strain [32].**

In general, the refractive index  $n$  depends on the semiconductor material bandgap. Compression enlarges the bandgap and therefore increases the refractive index [33,34]. It can lead to the fabrication of a waveguide. Materials birefringent can be achieved by breaking the crystal symmetry. Assume a waveguide going in the direction  $y$ , the alteration in the dielectric constant for the transverse electric optical mode TE ( $\Delta \epsilon_{xx}$ ) and transverse magnetic TM waves ( $\Delta \epsilon_{zz}$ ) are expressed as [33].

$$\Delta \epsilon_{xx} = -\epsilon^2_{xx} \left\{ \epsilon_{xx} \left[ \frac{1}{2} (p_{11} + p_{12}) + p_{44} \right] + \epsilon_{zz} p_{12} \right\}, \quad (2.13)$$

$$\Delta \epsilon_{zz} = -\epsilon^2_{xx} (\epsilon_{xx} p_{12} + \epsilon_{zz} p_{11}), \quad (2.14)$$

Here  $p_{ij}$  is a component of the photo elastic tensor.

#### 2.5.4 Example of an InGaAs/GaAs Quantum Well Under Biaxial Strain

In order to illustrate the consequence of strain and stress on a real QW structure, we will take an example of a single strained InGaAs quantum well structure grown on a GaAs substrate. In this case, a very small layer of InGaAs with lattice parameter  $a_f$  adjusts itself to form a pseudomorphic strained layer with a new lattice parameter  $a_\perp$  vertical to the growth direction equivalent to the one of the substrate  $a_s$ . The vertical strain in the quantum well can be written as

$$\varepsilon_{\perp} = \varepsilon_{xx} = \varepsilon_{yy} = \frac{a_s - a_f}{a_s} \quad (2.15)$$

As in this case,  $a_s > a_f$ , the lattice gets bigger in the xy plan. As a complement, it contracts in the growth direction z. To describe the effect of strain on electron-hole recombination, first we require defining the biaxial strain tensor  $\varepsilon$ , using equation (2.8)

$$\varepsilon = \begin{bmatrix} \varepsilon_{\perp} & 0 & 0 \\ 0 & \varepsilon_{\perp} & 0 \\ 0 & 0 & -2 \left[ \frac{c_{12}}{c_{11}} \right] \varepsilon_{\perp} \end{bmatrix} \quad (2.16)$$

Here  $\varepsilon_{\perp}$  is the strain in the xy plan, for compressive strain it is negative and for tensile strain positive and where  $c_{ij}$  are elastic distortion constants with  $c_{12}/c_{11} = v/(1-v)$ .

To launch the dilatation induced modification to the conduction band  $\Delta E_c$  and valence band  $\Delta E_v$ , we have to define the hydrostatic distortion potentials  $a_c$  and  $a_v$  for every band. i.e.,

$$a_c = -\frac{1}{3} \left[ c_{11} + 2c_{12} \frac{dE_c}{dp} \right], \quad (2.17)$$

$$a_v = -\frac{1}{3} \left[ c_{11} + 2c_{12} \frac{dE_v}{dp} \right] \quad (2.18)$$

Here  $dE_c/dp$  and  $dE_v/dp$  represents the hydrostatic pressure coefficients for the minimum direct bandgap. The alteration to the conduction band then becomes

$$\Delta E_c = \frac{2}{3} \left[ c_{11} + 2c_{12} \frac{dE_c}{dp} \right] \left( 1 - \frac{c_{12}}{c_{11}} \right) \varepsilon_{\perp} \quad (2.19)$$

Using the axial strain component, we can find the splitting of the heavy and light holes bands and conclude their positions.

$$\Delta E_{hh} = \frac{2}{3} \left[ c_{11} + 2c_{12} \frac{dE_v}{dp} \right] \left( 1 - \frac{c_{12}}{c_{11}} \right) \varepsilon_{\perp} - b_v \left[ 1 + 2 \frac{c_{21}}{c_{11}} \right] \varepsilon_{\perp} \quad (2.20)$$

$$\Delta E_{lh} = \frac{2}{3} \left[ c_{11} + 2c_{12} \frac{dE_v}{dp} \right] \left( 1 - \frac{c_{12}}{c_{11}} \right) \varepsilon_{\perp} - b_v \left[ 1 + 2 \frac{c_{21}}{c_{11}} \right] \varepsilon_{\perp} \quad (2.21)$$

The parameters  $b_v$ ,  $c_{ij}$ ,  $dE_c/d_p$  and  $dE_v/d_p$  used in equations (2.16) to (2.21) directly depend on the composition profile through the QW. Figure 2.10 demonstrates the strain effects on an InGaAs/GaAs intermixed quantum well.

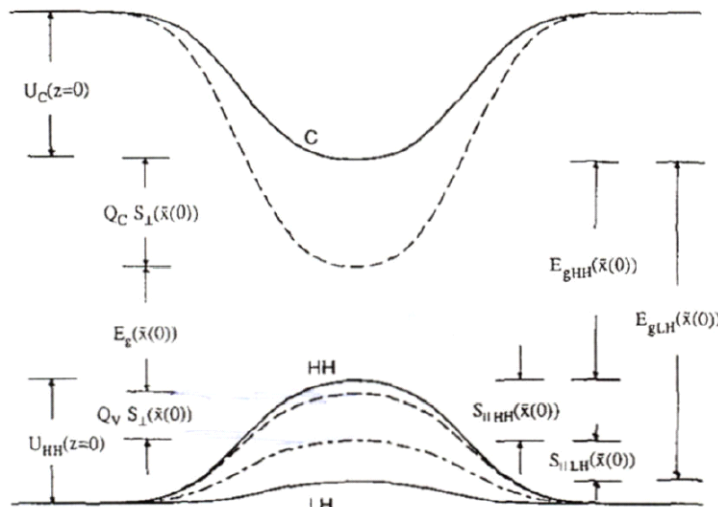


**Fig. 2.10 Strain influence in intermixed InGaAs/GaAs QW [30].**  
The dashed lines indicates the well normal band profile, the dash-dotted line presents the result of compression while the full lines show the heavy holes and light holes degeneracy elevate owing to axial strain component.

## 2.6 Laser Interaction with Semiconductors

The modification of material surfaces by using light is a fact which has been acknowledged for centuries. Michel Faraday in the nineteenth century was the first scientist to observe the “solarisation” of glass by UV light. Previously discolouration, cracking and bleaching of sun exposed surfaces was noticed frequently. Nevertheless, the learning of large extent light induced surface modification in a short time had to wait for the progress of a high density photon source i.e., the laser.

This section describes the fundamentals of the laser-matter interaction especially between lasers and III-V semiconductors. I introduce various photo-excitation processes then gives an assessment of the laser induced desorption and ablation methods.

### 2.6.1 Photo-excitation and Surface Response

Based on the wavelength of utilized laser, we can describe four kinds of absorption mechanism in semiconductors [35]. Here  $E_g$  is the material bandgap,  $n_{ec}$  is the free electrons density and  $\tau_{NR}$  represents the lifetime of non-radiative states,

1. Dielectric mechanism ( $h\nu \ll E_g$ )

The direct interaction between photons and the lattice results in absorption. The absorption generates coherent hypersonic phonons under high excitation,

2. Metallic mechanism ( $n_{ec}$  high)

This is a type of absorption, which occurs in material having high density of free carriers, electrons of the conduction band absorb photons energy through direct heating of the charge carriers gas. The excitation is degenerated due to the collisions among the electrons and the lattice.

3. Stimulate metallic mechanism ( $h\nu > E_g$  and  $\tau_{NR}$  long)

Profound excitation of electron of the valence band is crucial for this mechanism. The non-equilibrium free carriers absorbed the light. This excitation process is very significant than inter-band transitions.

4. Pure semiconductor mechanism ( $h\nu > E_g$  ;  $\tau_{NR}$  short)

In this mechanism, absorption of light generates electron-hole pairs. The charge carriers recombine through relaxation mechanism, the reaction of the lattice to the generation and movement of electron-hole pairs and free carriers rely on the energy  $h\nu$  of incident photon, on the electronic structure, on the material bandgap  $E_g$ , and on the built-in defects as illustrated in figure 2.11. The key mechanism of energy transfer to heat is via non-radiative electron-hole recombination.

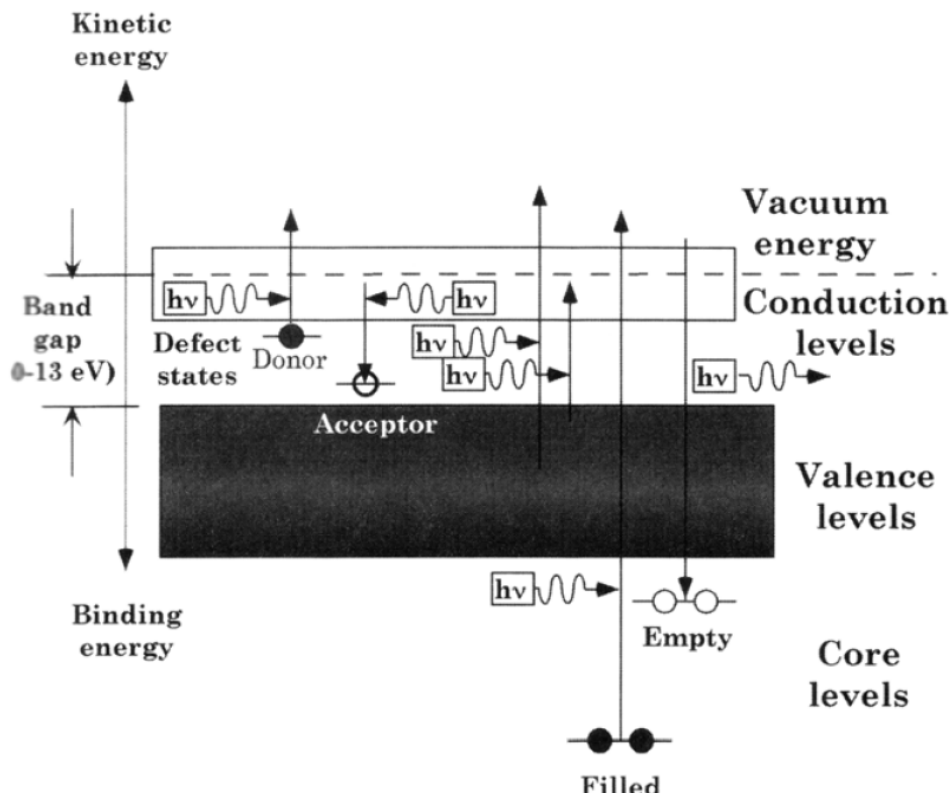


**Fig. 2.11 Schematic shows the photon assisted energy transition procedure in a nonmetallic solid [36].**

The laser caused desorption and damage dynamics is related to the photo-excitation process. Since the UV photons energy is more than the energy of InP bandgap, therefore the absorption mechanisms in InP material should be of type 3 or 4, that means the thermal relaxation has a large effect on the damage creation process.

### 2.6.2 Laser Induced Desorption and Ablation

When a material absorbed the laser irradiation, this means that the photon energy is changed to vibrational and electronic energy. The conversion of those photo-excited states into kinetic energy leads to the expulsion of atoms, molecules, ions, and clusters from the semiconductor material surface. By principle, the laser caused desorption is described as the ejection of particles,

- without causing visible mesoscopic alteration to the surface composition or structure,
- with a particle yield i.e., a linear function of the electronic density and vibrational excitation,

- without any considerable gas dynamic influences in the stream of particles exiting the surface [36].

On the other hand, laser ablation is described as the sputtering procedure in which

- material deletion rates typically go over one-tenth monolayer per pulse,
- surface of the material is structurally or compositionally changed at mesoscopic length scales,
- particle yields are super linear functions of the density of excitation [36].

Further, an increasing gas cloud of an ablated material, the ablation trail, make tricky image of laser ablation by adding notions of plasma-surface interaction, gas dynamics and laser caused photochemistry to the philosophy of the laser matter interaction. The difference between laser caused desorption and laser ablation is not very spiky. For example, at low laser fluences, desorption of the material surface may lead to material alteration that would permit ablation later on.

It is usually acknowledged that macroscopic harm caused by a nanosecond laser pulses happens when the material temperature gets its fusion threshold [37,38]. In this case, the quick extension of the irradiated material take place during the phase transition expels part of the material from its surface. This is also called as phase explosion. Based on this definition, it is likely to find out a material theoretical threshold to damage from the equation of the heat diffusion. Kunar and Garg observed the strength of this model by examining pulsed laser irradiated ( $\lambda = 1.06 \mu\text{m}$ ,  $\Delta t \sim \text{ms}$ ) Ge, GaAs and Si samples with SEM and optical reflectivity measurements.

### **2.6.3 Laser Pulse Absorption and Heat Transfer Processes**

The explanation of the heat diffusion expression allows the computation of the heat spatial and time distributions [35,39-41] in the semiconductor. We begin by using the heat diffusion mathematical expression adapted from the Fourier theory.

$$\rho c \frac{\partial T}{\partial t} = K \frac{\partial^2 T}{\partial x^2} + (1-R)\alpha P_0 e^{-\alpha x} \quad (2.22)$$

Here  $\rho$  is the material density,  $K$  is the thermal conductivity,  $c$  is the specific heat,  $\alpha$  is the absorption coefficient,  $R$  is the reflection coefficient,  $P_0$  is the applied power density where as  $T$ ,  $t$  and  $x$  are the temperature, time and depth respectively. In addition, we define the thermal diffusion coefficient  $D = K/\rho c$ . Table 2.1 presents the values of these constants for InP and GaAs materials for 248 nm excitation wavelength. By assuming semi-infinite substrate, the border conditions are

$$1) T(x)_{x \rightarrow \infty} = 0, \frac{\partial T}{\partial x} |_{x=0} = 0, \quad T(x)_{t=0} = T_0 ,$$

Then the solution to equation (2.22) is

$$\begin{aligned} T(x,t) = & \frac{(1-R)P_0}{K\alpha} \left[ 2\sqrt{D\alpha^2 t} \cdot ierf\left(\frac{x}{2\sqrt{Dt}}\right) - \exp(-ax) \dots \right] \\ & + \frac{1}{2} \exp(D\alpha^2 t - ax) erfc\left(\sqrt{D\alpha^2 t} - \frac{x}{2\sqrt{Dat}}\right) \dots \quad (2.23) \\ & + \frac{1}{2} \exp(D\alpha^2 t - ax) erfc\left(\sqrt{D\alpha^2 t} + \frac{x}{2\sqrt{Dat}}\right) + T_0 \end{aligned}$$

**Table 2.1 Thermal, mechanical and optical properties of GaAs and InP**

	GaAs	Reference	InP	Reference
$k$ (W/cm-K)	$0.425(300/T)^{1.1}$	Kuanr 1996	$0.68$ (T=300)	NSM Archive
$\rho$ (g/cm <sup>3</sup> )	5.31	NSM Archive	$4.81$ (T=300)	NSM Archive
$c$ (J/g-K)	$0.303+0.015(T/300)$	Kuanr 1996	$0.31$ (T=300)	NSM Archive
$D$ (cm <sup>2</sup> /s)	0.25 (T=300)	NSM Archive	$0.372$ (T=300)	NSM Archive
$R^I$ ( $\lambda = 248$ nm)	0.6 (T=300)	Phillip and Ehrenreich 1963	0.6 (T=300)	Aspnes and Studna 1983
$R^*$ ( $\lambda = 193$ nm)	0.4	Phillip and Ehrenreich 1963	0.4	Properties of InP [1991]
$\alpha$ (cm <sup>-1</sup> ) ( $\lambda = 248$ nm)	$2 \times 10^6$ (T=300)	Casey et al. 1975	$5.05 \times 10^6$ (T=300)	Aspnes and Studna 1983
$\alpha$ (cm <sup>-1</sup> ) ( $\lambda = 193$ nm)	$1.4 \times 10^6$	Casey et al. 1975	$1.3 \times 10^6$	Properties of InP [1991]
$T_{\text{fusion}}$ (K)	1520	Kuanr 1996	1333	NSM Archive
$\beta$ (°C <sup>-1</sup> )	$5.73 \times 10^{-6}$	NSM Archive	$4.60 \times 10^{-6}$	NSM Archive
$Y_0$ (dyn/cm <sup>2</sup> )	$8.59 \times 10^{11}$	NSM Archive	$6.11 \times 10^{11}$	NSM Archive
$p_0$	0.31	NSM Archive	0.36	NSM Archive

## 2.7 Summary

In this chapter, I have presented an assessment of the physics principles required to appreciate the extent and the propositions of my research work. The fundamentals of semiconductors and their relation with light were presented. Especially emphases were given to the relation of III-V semiconductors with laser light and how it can cause surface atoms desorption. This interaction also changes the stoichiometry of the surface as it plays a significant role in the research carried out in this thesis.

I talked about the bands profile effect on the optical characteristics of semiconductors. I also explained the concept of quantum well whose principal is the foundation of the QWI process. The composition and the width of the well also manage the optical characteristics of optoelectronic devices fabricated using QW structure.

I also introduced the theory of stress and strain. We have observed that they also alter the electrical and optical characteristics of a semiconductor. The dilation reduces the bandgap whereas deformations which change the symmetry of the crystal lift the light and heavy holes bands decadence at the  $\Gamma$  point of the Brillouin zone. Further, the formation of a biaxial stress is due to the existence of pseudomorphic strained layer having dissimilar lattice parameter than the substrate.

In the last section, I tried to distinguish the perceptions of desorption and ablation and explained their principal sources. They can occur due to heat transfer from the excited carriers, because of the existence of holes plasma and a free electron or from the mechanical stress caused by the temperature gradient.

Preferential desorption of certain atom can result in strong variation from surface stoichiometry. Nevertheless, UV-laser irradiation also works as an originator for surface chemical reaction. When operated in air environment, it robustly improves the oxidation of InP base QW structure.

## 3 Quantum Well Intermixing Techniques

### 3.1 Introduction

In order to integrate photonic devices monolithically, different regions representing certain optical and electrical properties should be fabricated on a single chip. The majority of commercially available passive-active photonic devices fabricated using quantum well structures. Commonly, optical characteristics of a semiconductor QW structures depend band structure and bandgap of the material. In comparison to microelectronic devices, where the integration can be realized by doping the semiconductor material locally, monolithic integration of photonic devices involves wafers with built-in sections of different bandgaps. Quantum well intermixing is a technique used to produce such wafers, without needing etching and multiple epitaxial re-growth steps.

Intermixing influences the composition and bandgap of the quantum well material, therefore it also affects its optical properties. For instance, changing the shape of the quantum well will result in a change in the electronic confinement, effective mass of the charge carriers and the refraction index. Such alterations can then be utilized to produce waveguides, to form a section of high optical confinement or to decrease losses in Bragg reflectors [16,43].

Further, QWI can also be applied to heterostructures with lower dimensionality than QW. Intermixing is happening in quantum wire [43,44] and in quantum dots [45] that modifies the position and the bands profiles. Moreover, since intermixing changes these nanostructures in volume, not only the vertical profile like in case of QW, its influence on the bandgap is even larger.

Here, I first explain the QWI concept, describe the effect of generated point defect and then stress on diffusion process. I briefly review various QWI techniques and present advantages and weaknesses of these techniques.

### 3.2 Description of the Quantum Well Intermixing Process

The QWI technique takes benefit of the heterogeneity of semiconductor structures utilized to produce photonic devices. We describe the active region as a stack of well and barrier layers. The function of photonic devices is defined by the characteristics of this active region, which is normally tens of nanometers wide. As wells and barriers are prepared from different materials due to which a big atomic concentration gradient present between them. At adequately high temperatures, the diffusion forces related to the concentration gradient start the intermixing process [46]. Further, this homogenizes the layers of wells and barriers and modifies the QW shape. Figure 3.1 demonstrates the modifications in composition and the change in the shape of the potential well linked to the intermixing process.

### 3.3 Diffusion Equation and Calculation of Energy Levels

We define analytically the influence of QW intermixing on the bands structure profile of a single quantum well by assuming that the barrier is wider than the diffusion length i.e.,  $L_D = \sqrt{D_t}$ , where t is the time and D is the diffusion coefficient. In this case, the intermixing is not affected by the composition of other layers. For instance, a ternary compound  $A_x^{''''} B_{1-x}^{'''} C^v$ , the diffusion expression can be resolved mathematically and the solution provides the concentration profile  $x(z, L_D)$  of a certain constituent atom as an error function profile [14].

$$x(z, L_D) = x_B + \frac{x}{2} \left[ \operatorname{erf}\left(\frac{L_z + 2z}{4L_D}\right) + \operatorname{erf}\left(\frac{L_z - 2z}{4L_D}\right) \right], \quad (3.1)$$

Here z is the growth direction, x and  $x_B$  are the initial composition within the well and in the barrier respectively while  $L_z$  is the well width centered at  $z = 0$ . Figure 3.2 illustrates evolution of such concentration profile.

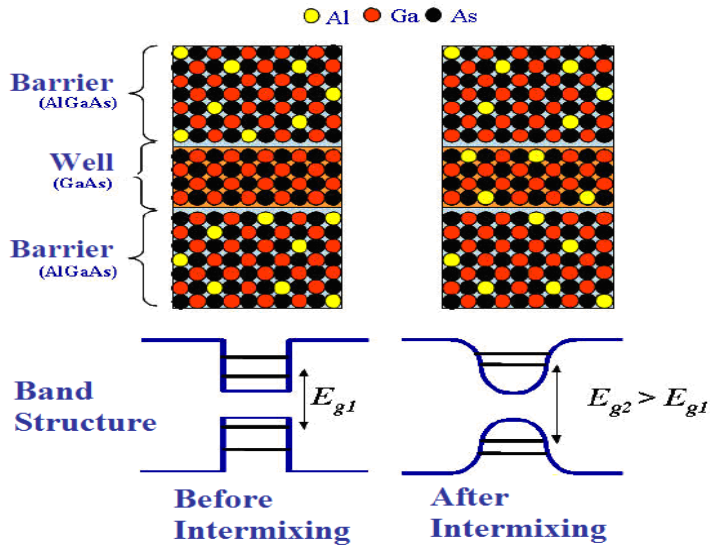


**Fig. 3.1 Schematic representation of QWI in AlGaAs/GaAs heterostructure**

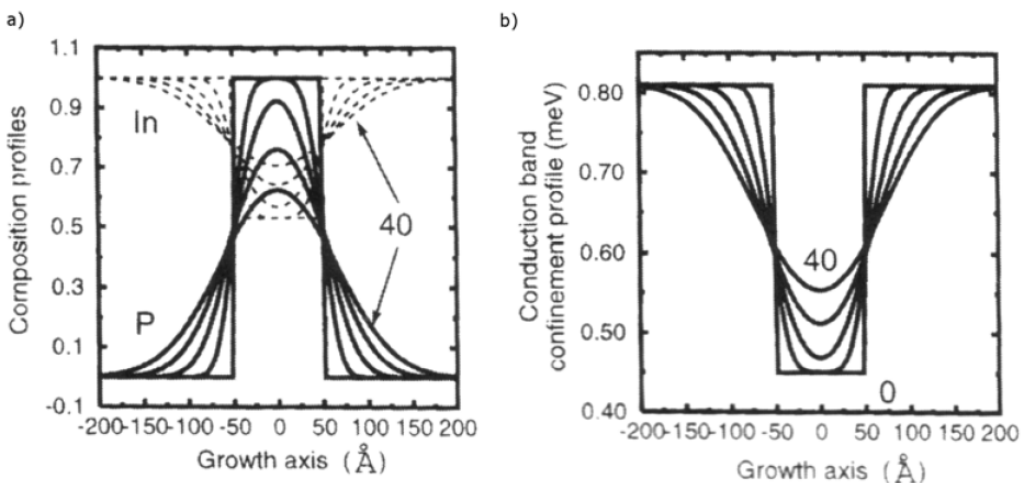


**Fig. 3.2 a:** Simulation of In and P composition profile in an InGaAs/InGaAsP QW for different diffusion length  $L_D$  ( $\text{\AA}$ ) following the model of equation (3.1b) conduction band profiles related to intermixed composition profiles [14].

Most of QW structures based on GaAs ( $A_x^{III}B_{1-x}^{III}\text{As}/\text{GaAs}$ ), group III atoms of the sub-lattice modify between the barrier and the well. But most InP based quantum well structures ( $A_x^{III}B_{1-x}^{III}C_yD_{1-y}^V/\text{InP}$ ), there is a concentration gradient among the barriers and the well for both group III and group V atoms. This implies that expression (3.1) must be generalize with two uncoupled expressions for concentration of group III elements (x) and group V elements (y) and consist of two different diffusion lengths i.e.,  $L_{III}$  and  $L_V$ :

$$x(z, L_{III}) = x_B + \frac{x}{2} \left[ \operatorname{erf} \left( \frac{L_z + 2Z}{4L_{III}} \right) + \operatorname{erf} \left( \frac{L_z - 2Z}{4L_{III}} \right) \right] \quad (3.2)$$

$$x(z, L_v) = x_B + \frac{y}{2} \left[ \operatorname{erf} \left( \frac{L_z + 2Z}{4L_v} \right) + \operatorname{erf} \left( \frac{L_z - 2Z}{4L_v} \right) \right] \quad (3.3)$$

Apart from very particular situations, the different diffusion lengths  $L_{III}$  and  $L_v$  between group III and group V atoms causes new strain in the quantum well. Therefore, in  $\text{In}_{0.53}\text{Ga}_{0.47}\text{As}/\text{InP}$  QW structure, preferential diffusion of group V atoms results in the formation of biaxial tensile strain in the wells, reducing the bandgap energy. The reverse influence is achieved with preferential diffusion of group III atoms. Bollet and colleagues modeled the influence of irregular diffusion length on the bandgap of an intermixed QW and confirmed that QWI can lead to red shift when  $L_v$  is larger than  $L_{III}$  illustrated in figure 3.3 [47]. To make the model simple, theorists typically make the supposition that altered layers remain lattice matched with InP, hence  $x$  and  $y$  are link to each other as  $x = 1 - 0.47y$  [48]. This makes sure that the strain related to lattice mismatch is restricted to 0.032% [49].

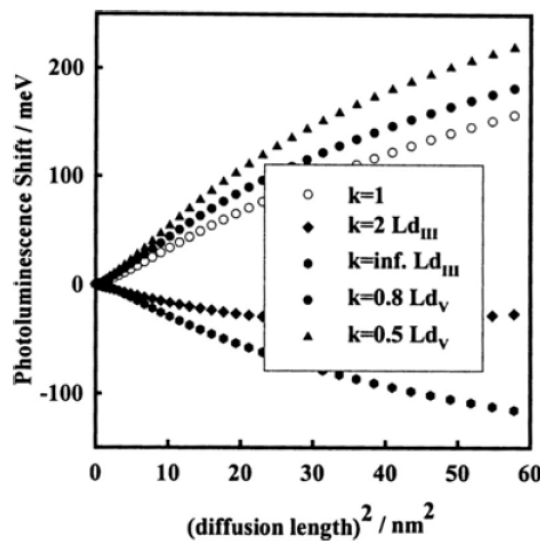


**Fig. 3.3** Theoretically calculated photoluminescence blueshift as a function of diffusion length with  $k = L_{\text{d}_{\text{III}}}/L_{\text{d}_v}$ . The abscissa is  $L_{\text{d}_{\text{III}}}$  for  $k > 1$  and  $L_{\text{d}_v}$  for  $k < 1$  [47].

By resolving the Schrödinger expression in BenDaniel-Duke approximation [50], the energy levels of the charge carriers in the intermixed well are determined with approximating the effective mass ( $m_r^*$ ) and an envelope function i.e.,

$$-\frac{\hbar^2}{2} \frac{d}{dz} \left[ \frac{1}{m_r^*(z)} \frac{dx_{rl}(z)}{dz} \right] + U_r(z) x_{rl}(z) = E_{rl} x_{rl}(z), \quad (3.4)$$

Here z is the growth direction,  $E_{rl}$  is the quantized energy level as l = p or q refers respectively to the level in the electrons and holes sub-band and  $\chi_{rl}$  is for the envelope wave function. By solving expression (3.4), we find the quantized energy levels  $E_{Cp}$  and  $E_{Vq}$  and their wave function  $\chi_{Cp}$  and  $\chi_{Vq}$ .

### 3.4 Point Defects Influence

At the start of the 80s, researchers revealed that it was viable to lower the energy required to achieve intermixing in AlGaAs/GaAs like structures by integrating zinc atoms [51]. They exposed that zinc impurity diffusion triggers the quantum well intermixing. This finding was technological spring board as it allowed the local alteration of semiconductor QW band structure without any need of re-growth step. Controlling the diffusion of the lattice defects was the vital element.

I indicate various types of lattice defects. They can be divided in groups based on three dimensionality i.e., point, line, planar and bulk defects as 0D, 1D, 2D and 3D respectively. Line, planar and bulk defects require much more energy to diffuse than 0D defects due to their bigger dimensionality. Therefore their ability to participate in the intermixing process is rather low. In contrast, point defects are usually weakly bounded to the rest of the lattice. So they can more easily diffuse over large distance. We indicate various types of point defects (Figure 3.4)

- Vacancies are unfilled lattice sites
- Interstitials are atoms which inhabit a site in the crystal between the normal lattice sites
- Frenkel pair or Frenkel defect is a pair of close by interstitial and vacancy
- Impurities are atoms which do not belong to the pure crystal, they can inhabit interstitial sites or substitute themselves to normal atomic sites

- Anti-site defect happens in ordered compound material when an atom of the sub-lattice A inhabits a site on the sub-lattice B.

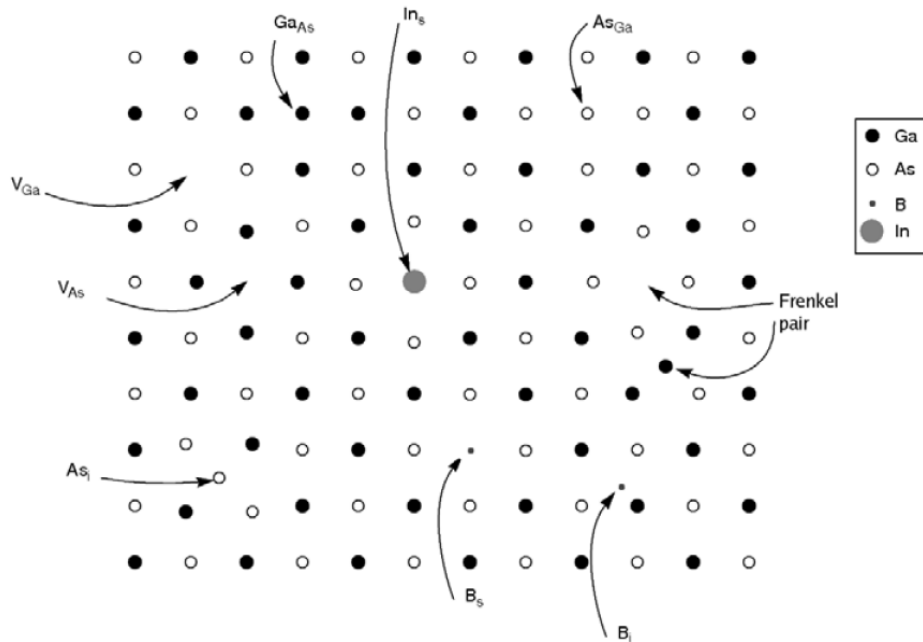


**Fig. 3.4 Image of the various point defects in a GaAs lattice. In this schematic, V represents vacancy, i for interstitial and s presents substitutionnal, while the notation AB indicates that the atom A inhabits the site of an atom B.**

Under certain thermodynamic condition and for a given temperature, the concentration of a specific kind of point defect will tend to accomplish its thermo-equilibrium concentration [52]. For example, as we raise the material temperature, vacancies close to the surface area achieves their equilibrium concentration through processes like desorption and generation of Frenkel pairs. The diffusion of the recently formed vacancies toward the bulk permits the whole material to get to its equilibrium. This also happens if a certain region of the material holds an extra concentration of point defect. Through diffusion, the material will intend to homogenize its concentration of point defects. Point defect diffusion obeys the Fick's laws, assuming de-concentration  $c$ , a kind of defect.

$$\vec{J} = -D\nabla c \quad (3.5)$$

and

$$\frac{dc}{dt} = D\nabla^2 c + S \quad (3.6)$$

Where  $\vec{J}$  is the flux of point defect, S is the generation-annihilation term and D is the diffusion coefficient. The passing of point defects via the active region decreases the energy required to accomplish intermixing between well and the barriers. The coefficient of intermixing relies on the activation energy  $E_A$  and obeys an Arrhenius law in respect with the temperature T. For instance, in an AlGaAs/GaAs QW structures, we state the intermixing coefficient  $D_{Al \leftrightarrow Ga}$  as

$$D_{Al \leftrightarrow Ga} = D_0 \exp(-E_A / K_B T), \quad (3.7)$$

Where  $D_0$  is the coefficient of intermixing at an infinite temperature,  $E_A$  is the activation energy and  $k_B$  is the Boltzmann constant. The existence of a point defect at barrier/well interface decreases the activation energy, permitting a quicker intermixing rate. Three major processes of point defect facilitated diffusion are shown in Figure 3.5.

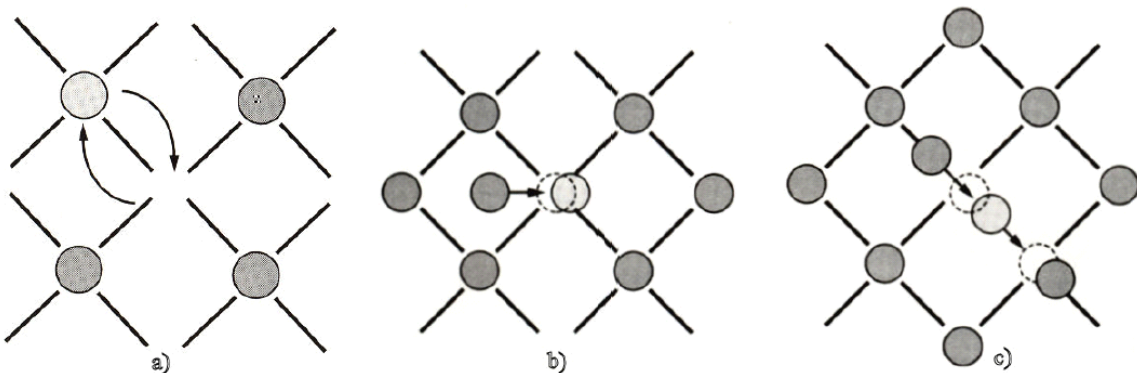


Fig. 3.5 Point defect initiated diffusion. a: Vacancy assisted diffusion, b: an interstitial thrusts an atom out of its lattice, c: diffusion channeling via interstitial jumps [53].

The activation energy of intermixing relies not only on the type of the material but also on the point defects diffusion processes in the material. This clarifies why at temperature up to 800°C, the GaAs based QW structures are stable while InP based QW structures typically start to show intermixing around 630°C. Every point defect diffusion process also influences the reliability of the QWI techniques with various material types. For instance, since in GaAs the interstitials do not diffuse easily, whereas it is the reverse case in InP. Therefore a quantum well intermixing technique based on the near surface generation of this kind of defects would have more success in InP than in GaAs.

### 3.5 Point Defect Diffusion under a Strain Gradient

Mainly, no external force is asserted on the point defects as ( $\vec{F} = 0$ ). So, the concentration gradient entirely directs the diffusion of point defects. Conversely, if some external force is there then the Fick's laws expressions (3.5) and (3.6) will change to

$$\vec{J} = -D\nabla c + \frac{D}{K_B T} \vec{F}c \quad (3.8)$$

and

$$\frac{dc}{dt} = D[\nabla^2 c - (\nabla c \cdot \nabla \vec{F} + c \nabla^2 \vec{F})] + S \quad (3.9)$$

Where  $\vec{F}$  is an external force asserted on the defect. Since point defects can be charged, so an electric field would have an influence on them. Therefore, a defect with an effective charge  $Z^*$ ,

$$\vec{F} = Z^* e \vec{E} \quad (3.10)$$

Likewise, if a temperature gradient ( $\nabla T$ ) exists in the structure then the resulting force will be

$$\vec{F} = -\frac{H_M}{T} \nabla T \quad (3.11)$$

Here  $H_M$  is the migration enthalpy.

On the other hand, with two standard forces, the elastic force on a defect relies strongly on the symmetry of the defect itself [54]. This is because of the interaction of the asserted strain field with the one formed by the defect. The defect symmetry is spherical in case of point defects in an isotropic material. We define a relationship between the defect volume  $V$  as a function of the mean atomic site volume  $V_0$  and mismatch parameter  $\alpha$ , i.e.,

$$V = V_0(1 + \alpha) \quad (3.12)$$

By using this classification, an interstitial atom comprises a dilatation center ( $\alpha > 0$ ) whereas a vacancy permits the lattice to compress on itself ( $\alpha < 0$ ). The asserted force on the defect can then be written as

$$\vec{F} = \alpha \frac{4}{3} r_0^3 \nabla \text{Tr}(\sigma) \quad (3.13)$$

Here  $r_0$  is the radius of the defect and  $\text{Tr}(\sigma)$  is the trace of stress tensor i.e.,

$$\text{Tr}(\sigma) = \sigma_{11} + \sigma_{22} + \sigma_{33}.$$

Equation (3.13) reveals that

1. Shear stress does not assert any force on a point defect.
2. A stress gradient desires to be present.
3. Under identical conditions, vacancies and interstitials are strained to drift in opposite directions. Considering a stress gradient, the Fick's laws are then written as

$$\vec{J} = -D \nabla c + \frac{D}{K_B T} \alpha \frac{4}{3} r_0^3 c \nabla \text{Tr}(\sigma) \quad (3.14)$$

and

$$\frac{dc}{dt} = D \left[ \nabla^2 c - \frac{4\alpha r_0^3}{3 K_B T} (\nabla c \cdot \nabla \text{Tr}(\sigma) + c \nabla^2 \text{Tr}(\sigma)) \right] + S \quad (3.15)$$

This depiction of point defect diffusion in enforced material was used by Britton and his fellows to imitate the smart-cut process utilized to produce silicon-on-insulator type wafers [55]. For this kind of process, large doses of  $H^+$  ions are implanted in a  $SiO_2$  coated silicon wafer [56]. The implanted atoms are situated in a very small volume where their presence causes a tensile stress in the QW material. In accordance with equation (3.15), interstitials are carried away to highest position from stress field, whereas vacancies drift toward it where they will come together as shown in figure 3.6. This will permit the top layers of the wafer to be sliced away from the substrate at high temperature,

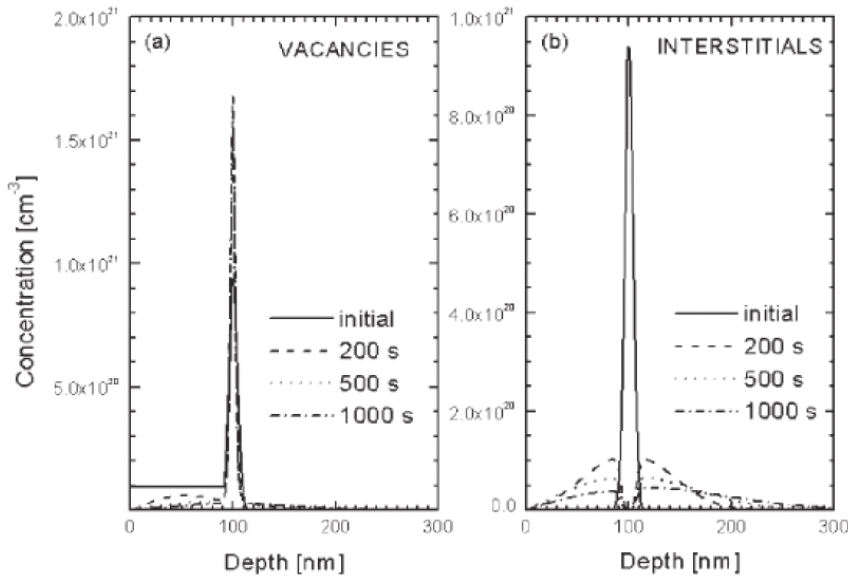


**Fig. 3.6 Temporal depth profiles, a: center of dilatation (vacancies) b: center of contraction (interstitials) in the field of tensile stress centered at the defect's original position [55].**

### 3.6 Review of Quantum Well Intermixing Techniques

By heating a QW structure over a threshold temperature, QWI can be realized. Because of the high concentration gradient at high temperature, constituent atoms intermix at each interface in between two layers. The intermixing coefficient  $D_{A \leftrightarrow B}$  obeys law of Arrhenius as a function of temperature:

$$D_{A \leftrightarrow B} = D_0 \exp\left(\frac{-E_A}{K_B T}\right) \quad (3.16)$$

At an infinite temperature,  $D_0$  is the intermixing coefficient,  $k_B$  is the Boltzmann constant,  $T$  is temperature and  $E_A$  is the activation energy. We describe the thermal shift as the blueshift, entirely linked to the thermal annealing. This eliminates the influence of point defects deliberately launched in the QW structure or of stress asserted prior to the annealing step. Equilibrium native point defects participate in the intermixing process and their existence decrease the activation energy  $E_A$ . Because it only needs a furnace therefore this technique is comparatively easy to implement. Nonetheless, it does not suggest any way to classify selectively intermixed regions of the same wafer [5]. Moreover, for the production of multi-bandgap material with distinct regions, thermal shift is not required and we normally desire to limit this

influence to a least amount typically less than 15 nm, in order to preserve the original properties of the QW structure.

In the last 35 years, various quantum intermixing techniques were introduced. We can categorize these techniques in four special categories, i.e., impurity induced intermixing [57], impurity-free vacancy diffusion [58-61], QWI induced by ion implantation [5,62], and laser induced QWI [63,18].

Commonly, laterally controlled QWI techniques depend on the diffusion of point defects. This is achieved either by asserting an external force on the defects or by establishing an extra concentration of defects in the QW material.

### **3.7 Impurity Induced Disorder**

At the start of the 80s, QWI was first considered in AlGaAs/GaAs heterostructures as an unwanted influence happening during high temperature treatments [51]. The diffusion on zinc while anneal at 600°C enhances aluminum and gallium inter-diffusion by a factor of 105 [64]. Other impurities utilized as dopants, Ge, Si, S, Se, Mg and Be were also found to boost the Al/Ga inter-diffusion [65].

One of the most studied of all quantum well intermixing techniques is Impurity induced disordering (IID) in (Al)GaAs structures. Through its research, the function of group III point defects (free vacancies and interstitials) was recognized and so was the influence of the Fermi level [66] and arsenic overpressure on the intermixing performance [65]. Even though it is well known and effective technique, the impurity induced disordering will always results in bigger optical losses because trapping of the free carriers by impurities in the active region of the QW structure. Consequently, its use for photonic integration is restricted. Furthermore it is established that the metal contacts are not successful after IID QWI. The IID method can not only be realized in many ways to accomplish localised QWI in GaAs based QW structures but also in InP [67]. However, since it enlarges the optical losses in the intermixed region.

Therefore, this method is more applicable for application which does not directly entail passive light transmission in the intermixed areas [68].

### 3.8 Impurity-free Vacancy Disorder

This technique's principle depends on the improved diffusion of constituent atoms of the QW structures. This means, it is achieved without incorporating new impurities. For this purpose, a dielectric cap, normally  $\text{SiO}_2$ , is deposited on the surface of the QW structure. Mainly, during an annealing process, constituent atoms travel into the cap layer which creates new point defects very close to the surface. The annealing process also influences the point defects to diffuse toward the active region of the material where they trigger the intermixing. The capping layer's thickness affects the number of free vacancies generated. For thinner caps, the limit of solubility is achieved quicker than for thicker caps. This implies that the maximum concentration of surplus point defects is achieved quicker and smaller inter-diffusion coefficient can be realized.

For instance, in case of  $\text{AlGaAs}/\text{GaAs}$  QW structures, while annealing, due to its high solubility in  $\text{SiO}_2$ , gallium (Ga) out-diffuses in the cap layer, leaving gallium vacancies in the material. Still under the influence of high temperature, these vacancies diffuse through the quantum well and barrier layers where they participate in the quantum well intermixing by decreasing the activation energy [16]. As these vacancies diffuse at a temperature lower than the thermal energy required to activate the atomic inter-diffusion inside the wells, the intermixing is restricted to the capped areas.

The type of the capping material will also affect the intermixing, i.e., whether it activates or restrains the inter-diffusion process. For example, in case of  $\text{AlGaAs}/\text{GaAs}$  QW structures, the intermixing is accelerated by  $\text{SiO}_2$  [61], while intermixing is slowed down by using  $\text{SrF}_2$  [59],  $\text{TiO}_2$  [69, 70] and  $\text{Ga}_2\text{O}_3$  [71]. During the procedure of annealing, the disparity in the expansion coefficients  $\alpha$  of semiconductor and the dielectric layer causes stress in both materials [70]. In  $\text{GaAs}$  ( $\alpha_{\text{GaAs}} = 5.73 \times 10^{-6} \text{ }^{\circ}\text{C}^{-1}$ ), the annealing with a  $\text{SiO}_2$  ( $\alpha_{\text{SiO}_2} = 0.5 \times 10^{-6} \text{ }^{\circ}\text{C}^{-1}$ ) cap places the  $\text{GaAs}$  under

compressive strain which assist gallium out-diffusion toward  $\text{SiO}_2$  and enhances the creation of extra gallium vacancies. While annealing using a cap with a higher expansion coefficient than GaAs, e.g.  $\text{TiO}_2$  ( $\alpha_{\text{TiO}_2} = 8.2 \times 10^{-6} \text{ }^{\circ}\text{C}^{-1}$ ), has the reverse influence and suppresses thermal shift in InGaAs/AlGaAs/GaAs QW structures [70] and in InGaAs/GaAs quantum dots [69]. Moreover, these capping materials typically have little gallium solubility, therefore under them gallium vacancies are less likely to generate contrast with GaAs free surface. Lithography methods permit the patterning of a QW sample with dielectric material promoting and restraining the intermixing (Figure 3.8) [72].

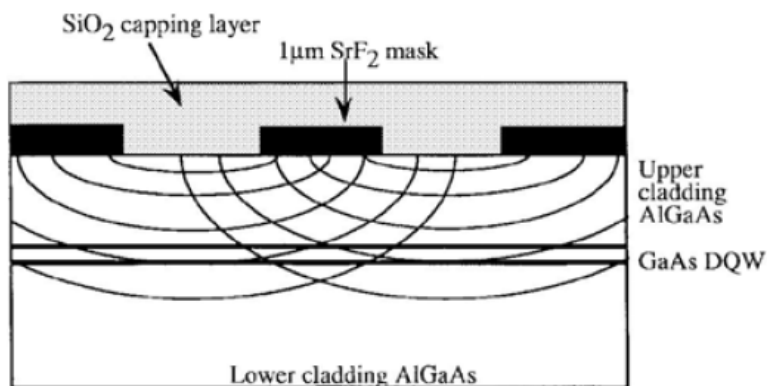


**Fig. 3.8 An example of dielectric capping to restrict QWI [73].**  
 **$\text{SiO}_2$  promotes interdiffusion while  $\text{SrF}_2$  prevents interdiffusion.**

Mainly, silicon nitride ( $\text{Si}_3\text{N}_4$ ) is utilized in order to suppress intermixing in GaAs based quantum well structure when using the impurity-free vacancy disordering technique [74,61] since the deposition of high quality  $\text{Si}_3\text{N}_4$  film is well studied. Mr. Teng and his group achieved 135 nm blueshift using InGaAsP/InP QW structure covered with either  $\text{SiO}_2$  or  $\text{Si}_3\text{N}_4$  after an annealing at  $800^{\circ}\text{C}$  for 100s. Figure 3.9 also illustrates that covering part of the under observation sample with  $\text{Si}_3\text{N}_4$  reduced the thermal shift compared to the uncovered region. Nevertheless, under specific deposition conditions [75],  $\text{Si}_3\text{N}_4$  can also improve the inter-diffusion.

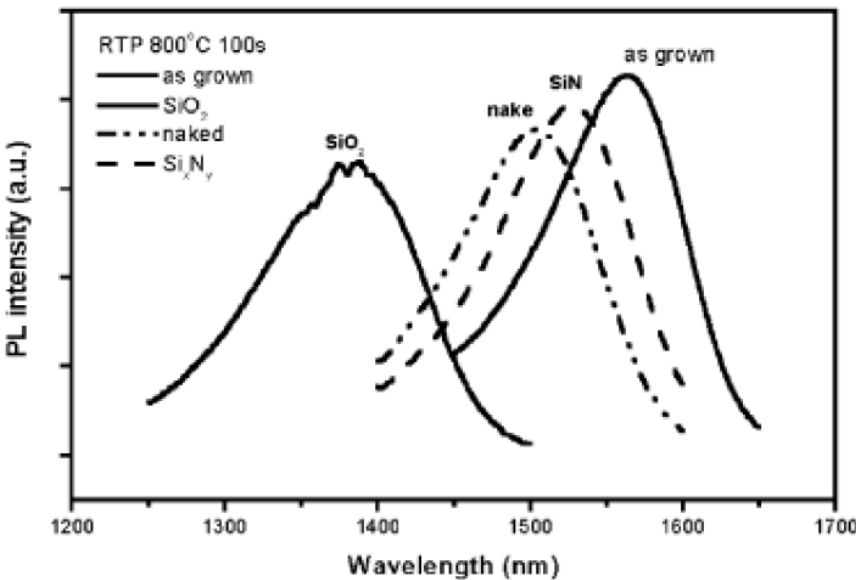


**Fig. 3.9 Photoluminescence spectra from an altered and reference InGaAsP MQW sample after annealing [61].**

On the contrary, with most inhibiting materials,  $\text{Si}_3\text{N}_4$  does not cause a tensile stress in GaAs but a little compressive stress ( $\alpha_{\text{Si}_3\text{N}_4} = 2.8 \times 10^{-6} \text{ }^{\circ}\text{C}^{-1}$ ). Therefore the inhibition mechanism while using  $\text{Si}_3\text{N}_4$  as a dielectric cap is simply related to its little solubility to gallium. When the porosity of  $\text{Si}_3\text{N}_4$  enhances, its voids increase out-diffusion of gallium atoms from GaAs which improves the QWI process [76].

In some situations,  $\text{SiO}_2$  caps can also restrain intermixing. Suppressed intermixing in AlGaAs/GaAs laser structure was observed [77] by using caps of phosphorus doped  $\text{SiO}_2$  ( $\text{SiO}_2:\text{P}$ ). They deposited  $\text{SiO}_2:\text{P}$  by using plasma enhanced chemical vapour deposition on one n-i-p and one p-i-n double QW structures and annealed them at temperatures (800°C - 950°C). They accomplished intermixing suppression in both structures and achieved contrasts as large as 50 nm (n-i-p) and 40 nm (p-i-n) with samples coated with  $\text{SiO}_2$  and annealed as shown in figure 3.10. The suppression is simply due to the fact that  $\text{SiO}_2:\text{P}$  holds far less voids than  $\text{SiO}_2$  and that it is denser, consequently it has a lesser solubility to gallium. Further, inclusion of phosphorus in  $\text{SiO}_2$  boosts its expansion coefficient which lowers the caused stress while annealing, making Ga out-diffusion less favorable.

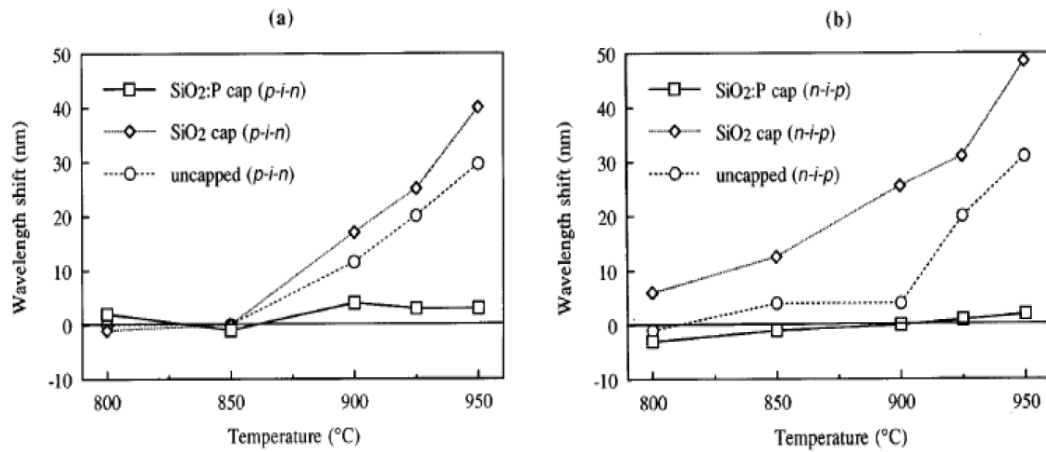


**Fig. 3.10 Shift of PL peak for SiO<sub>2</sub>:P capped, SiO<sub>2</sub> capped and uncapped, a: p-in and b: n-i-p laser structures [77].**

Mostly, impurity-free vacancy disordering is utilized to integrate optoelectronic devices fabricated using (In)AlGaAs/GaAs QW structures [78]. Whereas this technique has also been successfully utilized to integrate devices made on InP based QW structures [61]. Its use on this kind of semiconductor is more challenging than on crystalline systems based on GaAs and typically need the growth of a defect layer. In InP QW structures, the energy required to trigger the out-diffusion of surface atoms in the dielectric cap is analogous to the inter-diffusion activation energy. Moreover, impurity-free vacancy disordering only serves a limited selectivity and frequently results in energy shift on the entire sample [79]. The strain situated inside the dielectric layers was recommended to affect the diffusion process and influence its reproducibility [80].

One of the main benefits of this method is the fact that it does not launch impurity inside the material. Easy implementation of this technique and its simplicity make it extensively used in GaAs based QW structures. Nevertheless, dielectric capping induced QWI does not provide a global solution to produce photonic integrated circuits, especially on InP based QW structures. The quality of the deposited dielectric material is hard to control and such control is critical to achieve reproducible results. Furthermore, this technique does not provide practical diagnosis tools permitting in-situ measurement of the inter-diffusion.

### 3.9 Dielectric Sputtering Induced Intermixing

This technique was introduced by a group from the Glasgow University, and also identified as “universal damage technique”. It is also recognized as impurity-free because it does not require the introduction of alien atomic species within the QW structure. It involves in depositing a layer of  $\text{Si}_3\text{N}_4$ ,  $\text{SiC}$  or  $\text{SiO}_2$ , on top of the substrate using magnetron sputtering [81]. In addition to generate a dielectric cap, the sputtering method damages the surface of the QW structure creating shallow point defects. An annealing step triggers the QWI process. Two mechanisms are accountable for the inter-diffusion in this technique. First one is the sputtering generated free vacancies and interstitials near the surface diffuse toward the active region and trigger the inter-diffusion at high temperature. Secondly, in case of GaAs based materials, while annealing, the dielectric cap absorbs gallium atoms and creates surface free vacancies in the semiconductor. Similar to the dielectric capping method, these new point defects diffuse in the direction of the well and contribute to the inter-diffusion [82]. Patterned resist can also be utilized to guard specific regions, preventing the process of intermixing under them.

To learn the defect creation process, Kowalski and his fellows used QW structures with five quantum wells of dissimilar width (Figure 3.11a). They calculated the photoluminescence (PL) spectra before and after sputtering. The decreased PL intensity of the two shallowest peaks recommended that the sputtering process creates damage in the shape of mobile point defect, which enhanced the non-radiative recombination. They calculated the damage limit depth to be 550-750 Å [81]. After annealing step, the PL signal from the first wells was improved due to the diffusion of the high concentration of point defects toward the surface and deeper inside the QW structure.

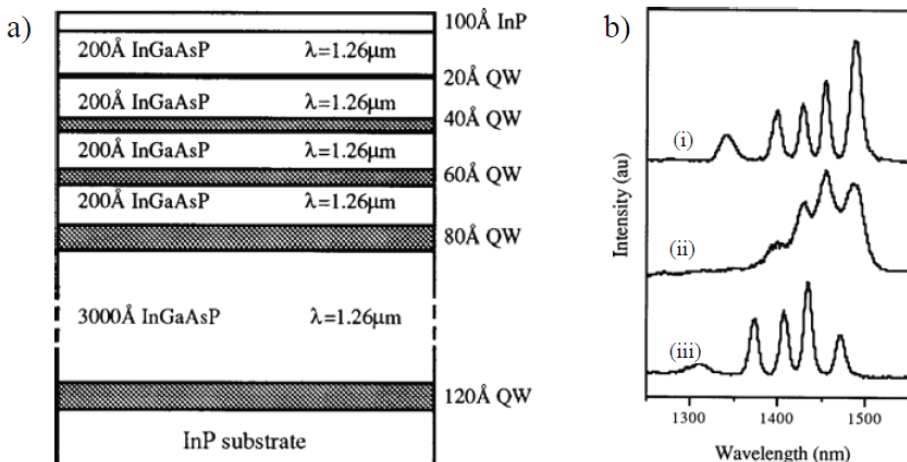


**Fig. 3.11 a:** InGaAs/InP QW structure with five QWs of different widths, **b:** PL spectra before (i) and after (ii) pulverization and after RTA at 500°C for 60s [81].

The process is almost the same for InP [83] based QW structure than on GaAs [84]. Nevertheless, it is hard to control the quantity of created defects. Reproducibility then becomes a key problem. The extent of inter-diffusion can be controlled by annealing temperature and time. It is then tricky to realize sites with more than two different bandgaps. Liu and colleagues tried to tackle this problem by masking the QW structure using a stepped SiO<sub>2</sub> layer (Figure 3.12a) deposited by PECVD before the sputtering method [85]. They noticed that the blueshift reduced as the thickness of the SiO<sub>2</sub> mask increased (Figure 3.12b). The SiO<sub>2</sub> mask restricted the number of created point defects while sputtering.

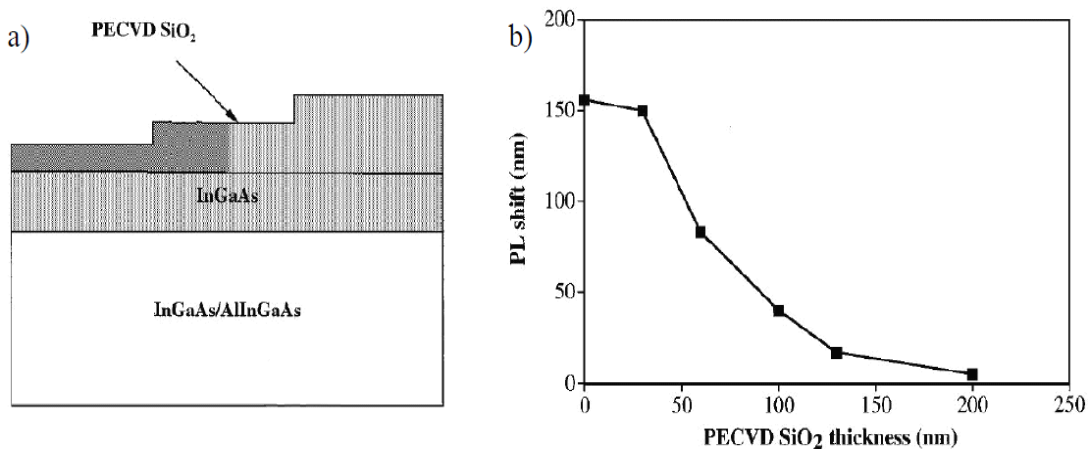


**Fig. 3.12 a:** Schematic diagram of the stepped PECVD SiO<sub>2</sub> mask, **b:** PL blueshift as a function of mask thickness [85].

Since this technique generates large quantity of sub-surface damage, therefore the quality of the QW material is drastically compromised. Laser diodes produced from

such intermixed QW structures (blueshift = 140 nm) reveal a threshold current of 300% higher than the one calculated for laser diodes fabricated from the untreated material [82,86].

### 3.10 Low Temperature Epitaxial “Defect” Layer

Enhanced QWI during native point defect diffusion can also be achievable by growing a layer having a large concentration of defects. This kind of layer can be grown by using low-temperature epitaxy technique. For example, a layer holding large concentration of Ga vacancies and As interstitials was achieved by growing GaAs at temperature about 200°C, i.e., well below the temperature needed for the growth of high quality GaAs [87]. This technique was also utilized productively for QWI in InP based QW structure [61] and InAs quantum dots grown on InP [88]. This process does not need any defect introduction after the epitaxial growth of the structure. By selective elimination of the defect layer prior to annealing, the localized bandgap shift can be achieved.

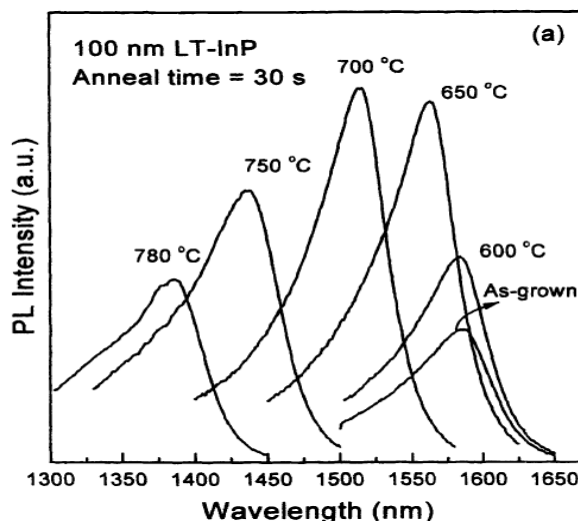


**Figure 3.12** PL intensity of samples annealed at various temperatures for 30s with a LT-InP layer [89]

As an example, (Figure 3.12) for a 30s anneal at temperature 780°C, the LT-InP sample produces a net blue-shift of 155nm. More important is the fact that blue-shifts necessary for making an integrated wave-guide or modulator structure, sufficiently transparent can be achieved at considerably lower temperatures. For example, using the LT-InP process it is possible to obtain a net blue-shift of 6nm following a 30s

anneals at 700°C, and it is possible to produce adequate blue-shifts for anneals at temperatures below 700°C.

The major disadvantage for this process is the condition of non standard QW structures with low temperature growth, which can lead to reproducibility problems and the intricacies to have a steady control of the bandgap shift.

### **3.11 Ion Implantation Induced Quantum Well Intermixing**

When a semiconductor is implanted with an ion beam, the collision between the implanted specie and the lattice atoms relocate the later ones away from the initial site, making Frenckel's pair defects [90]. We differentiate between two different categories of implantation. The first one is made at low acceleration energies (under 500 keV). With these energies, ions are blocked well above the quantum well and the created defects are restricted to the higher layers. This type of implantation is identical to the one used for doping semiconductor material when producing integrated circuits. The second implantation category is achieved with high acceleration energies (0.5 to 10 MeV). In the latter case, ions are implanted through the whole QW structure and the creation of point defects takes place directly in the quantum wells.

The created defects are due to the multiple collisions of the incident ions with the atoms of the material. The extremely active ions propagate through the lattice and they thrust atoms out of their lattice sites. Consequently, ion implantation creates vacancies as recently vacant lattice site and interstitials which correspond to the relocated atoms and the implanted ions. An additional annealing step allows the defects diffusion and activates quantum well intermixing in both low and high energy implantation. The annealing process also rebuilds part of the damage done to the lattice [91].

The amount of point defects introduced in the QW material depends of various implantation parameters [5].

- the dose ( $\text{ion}/\text{cm}^2$ ),
- the mass of the implanted ions,

- the incident angle,
- the ion energy,
- ion flux or ion current density ( $\text{A}/\text{cm}^2$ ),
- the substrate temperature during the implantation.

The dose plays a critical role on the degree of blueshift as shown by figure 3.13.

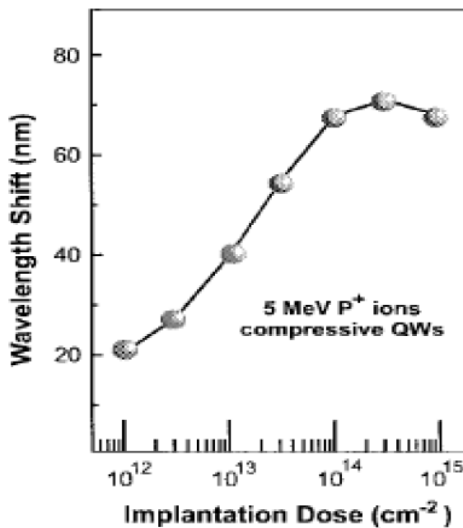


**Fig. 3.13 Quantum well PL peak shift as a function of implantation dose [5].**

In case of AlGaAs/GaAs QW structures, best results were achieved by implanting constituent atoms straight through the quantum well, i.e. using acceleration energies of few MeV [92]. Due to the rapid diffusion of point defects, diffusion in InP based QW structures [62], defects do not require to be generated in the active region area. In contrast, creating them farther from the quantum well causes less damage. The crystal then requires a lower annealing temperature to reconstruct itself which decreases the impurity diffusion in doped QW structures. Moreover, as there is less damage close to the active region, we can guess superior performances of devices produced from the intermixed material. Figure 3.14 shows that a blueshift of 25 nm can be achieved without influencing the threshold current density of the laser diode. A sacrificial layer can also be utilized to further restrict the damage to the QW structure [93]. After the annealing step, the sacrificial layer is etched away, leaving nearly damage free surface for the device fabrication.

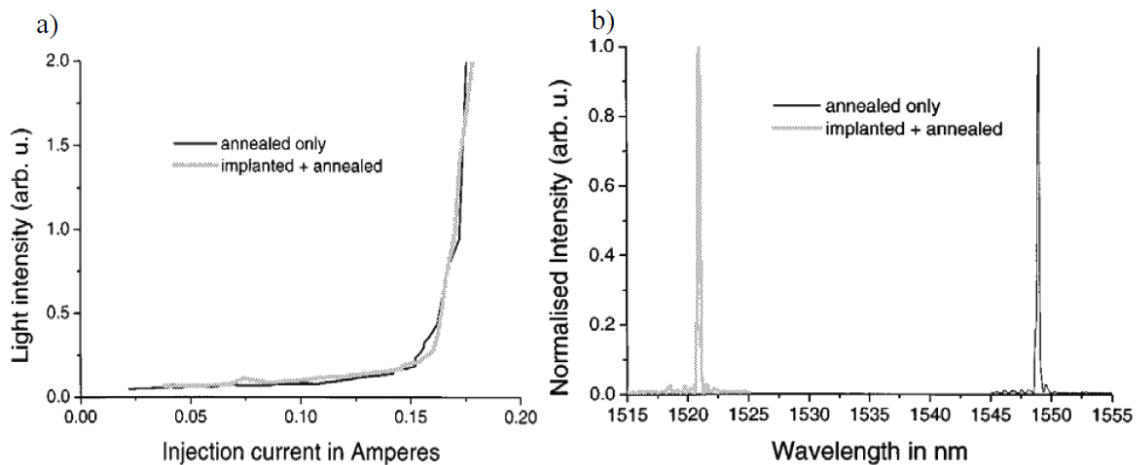


**Fig. 3.14 An example of laser diode characteristics, a: Implanted and RTA sample showed almost no increase of the threshold current density compared to the RTA-only sample b: while the implantation make the laser diode to shift by 25 nm [62].**

Researchers have fabricated multiple bandgap samples to address integration of photonic devices. This was achieved either by masking various regions and doing numerous implantation steps or by implanting through a single mask using a variable thickness [94]. In the latter case, a mask of graded SiO<sub>2</sub> was utilized to hold back the incident ions. Doing so, Ng and fellows accomplished an integrated chip on a single InGaAs/InP laser QW structure with twelve regions of different bandgaps. Using this technique, a waveguide modulator arrays was fabricated on a single InGaAs/InP wafer chip [95].

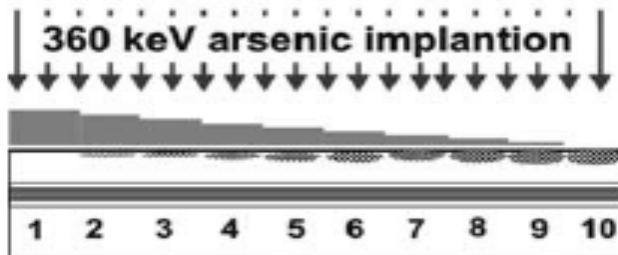


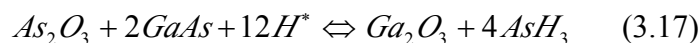
**Fig. 3.15 Schematic diagram of arsenic implantation using a graded SiO<sub>2</sub> mask [95].**

As we know that the ion implantation is present previously in the microelectronic industry as a doping solution. The ion implantation induced QWI particularly for low acceleration energies, suggest an interesting solution as an integration means for photonic devices. Even though an industrial ion implantation induced QWI procedure would need a devoted ion implanter, which is a costly apparatus. As substrate sizes

and contamination matters would stop such a tool for ion implanting both in InP and Si based devices. The lattice damage requires to be annealed out so it does not influence the devices electrical and optical properties for low and high energies implantation. The main disadvantage associated with this procedure is linked to multiple bandgap devices fabrication where the bandgap control needs the fabrication of complicated SiO<sub>2</sub> masks with controlled thickness steps or multiple masking/implantation Steps, therefore resulting to lower yields.

### **3.12 Plasma Induced Defect Disorder**

Reactive ion etching (RIE) is linked with bombarding the QW sample with energetic ions. Similar to low energy ion implantation, the RIE ions create Frenckel's pair defects when they crash with the atoms of the lattice. A large density of point defects is created in the surface area, far away from the active region, which stops the damage and deterioration to the optical performances of the intermixed material [96]. An annealing step is required to drift the mobile point defects diffuse toward the active region and to initiate the intermixing process. Novel research on plasma induced defect disordering was carried out on AlGaAs/GaAs QW structures treated in a RIE system using H<sub>2</sub> plasma. After nine exposures and annealing steps, a maximum blueshift of 24 nm was achieved [73]. The technique was also applied to InGaAs/InP QW structures and led to maximum 10 nm of blueshift [97]. In AlGaAs/GaAs systems, when the QW sample was previously covered with a native oxide. The H<sub>2</sub> plasma procedure was carried out at room temperature and was also noticed to suppress the intermixing [98]. This was due to the strong dipping capacity of hydrogen, which modifies the stoichiometry of the native oxide by decreasing the As<sub>2</sub>O<sub>3</sub> to AsH<sub>3</sub>. The freed oxygen atoms can then react with the GaAs and form Ga<sub>2</sub>O<sub>3</sub> [99].



Here H\* are the hydrogen radicals. This reaction proceeds to an entire coverage of Ga<sub>2</sub>O<sub>3</sub> as all liberated Ga, As and As<sub>2</sub>O<sub>3</sub> are forced to form Ga<sub>2</sub>O<sub>3</sub> - the most steady product of the reaction [98]. While annealing, the Ga<sub>2</sub>O<sub>3</sub> layer works as a stressor and set the QW structure under tensile strain. This was reported to stop vacancies placed in the surface area to diffuse toward the QW active region [69].

Argon plasma produced by an inductively induced plasma (ICP) initiator was also utilized to introduce point defect in InGaAs/InP QW structures [96]. Djie and his group accomplished 88 nm differential shift between the masked regions and the plasma treated ones using a patterned SiO<sub>2</sub> mask.

Models of defects produced by plasma procedure [100] have permitted various research teams to examine their role and the QWI kinetics [101,102]. This method was also effectively used to produce integrated devices [103]. This process has the benefit to be based on comparatively easily available tools. Nonetheless, in case of H<sub>2</sub> plasma irradiation, the several problems related to the consistency and reproducibility of the technique will require more research for this method to be a genuine solution to photonic devices integration.

### **3.13 Laser Induced Quantum Well Intermixing**

Laser induced QWI relies firmly on the type of the laser (CW vs pulse), emission wavelength and the duration of pulse. Photons with energy larger than the absorption edge of the semiconductor material are absorbed easily and raise the lattice temperature, whereas, photons with smaller energy can only be absorbed at defect locations through multi-photon processes.

#### **3.13.1 Continuous Wavelength Laser Induced QWI**

The 1<sup>st</sup> example of laser caused altering of the QW sample goes back to 1986, when Epler and his group utilized an argon ion laser ( $\lambda = 488$  nm) to intermix an AlGaAs/GaAs superlattice [104]. The laser power densities of  $2.5 \times 10^7/\text{cm}^2$  were utilized. Intermixing was mainly because of the quick melting and re-growth of the laser operated material. Covering of the QW structure with Si<sub>3</sub>N<sub>4</sub> and Si caps prior to the laser irradiation permitted Si impurities to integrate in the QW structures during the irradiation process. An annealing process then initiated the impurity diffusion, similar to the IID method leading to an impurity induced inter-diffusion of the superlattice. The laser spot can be applied on a much localised area. Delimiting the various regions is achieved either by directly writing on the QW structure by utilizing a scanning beam or by coating a reflecting mask defined by lithography. Using the laser

caused diffusion, Epler's team achieved 40 nm shifts between the altered and as-grown regions. Even if scanning electron microscopy illustrated damage linked to the laser irradiation, low threshold laser diodes were produced using Ar<sup>+</sup> laser disordering [104,105].

A continuous wave Nd:YAG laser (1-20 W/mm<sup>2</sup>) was studied for QWI in InGaAs/InGaAsP QW structures by McLean and his group in 1992. The irradiation time was about 30 minutes. The laser source's wavelength was selected in such a way that the photons were only absorbed in the barriers and the wells at room temperature, while the cladding layers were transparent to them (Figure 3.16) [106]. Laser radiation was absorbed in the QW region. The relaxation of the charge carriers in excess concentration and non-radiative recombination creates heat which initiates the intermixing process. The coating of a dielectric cap also hinder the surface desorption caused by the laser irradiation [106]. The degree of QWI is controlled by changing the irradiation time or the applied power density. Even though this method is "layer composition sensitive" [16] at room temperature, as the temperature of the QW structure increases, its bandgap decreases and photon absorption can take place over the entire sample thickness.

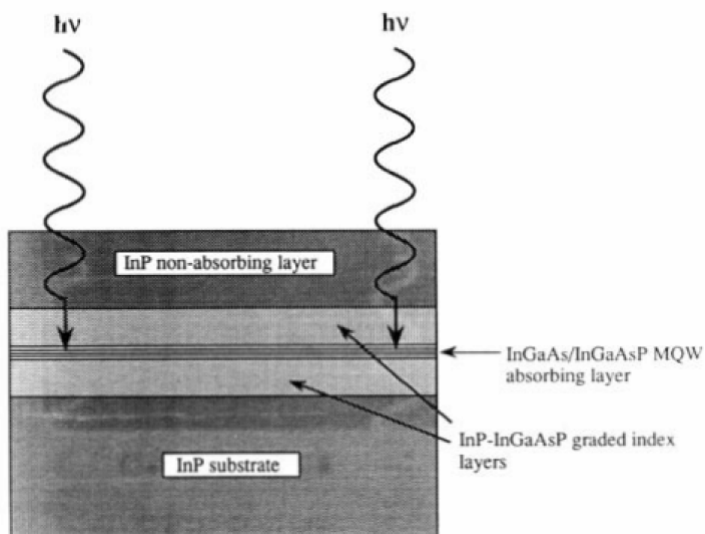


**Fig. 3.16 Laser absorption in the QW and barriers. Cladding layer of InP and the substrate are transparent to incident light [16].**

Figure 3.17 presents the peak position of PL emission from an InGaAs/InGaAsP/InP QW structure sample after Nd:YAG laser irradiation with an

enlarged Gaussian beam. The power density of  $0.5 \text{ W/mm}^2$  was used for 20 seconds and the wavelength shift was more than 120 nm. For a modest irradiation (site #2), the laser annealing repaired region of the structural defects still present after the QW structure growth, enhancing the intensity of the PL signal [18].

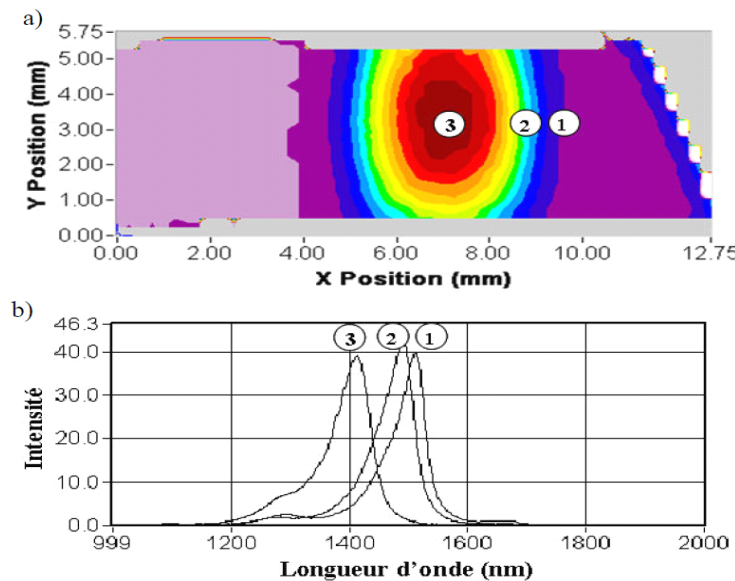


**Fig. 3.17 a)** Photoluminescence mapping of a InGaAs/InGaAsP/InP heterostructure irradiated with an Nd:YAG laser, **b)** photoluminescence spectra taken on the sample at position 1,2,3 [18].

Direct laser writing has been utilized to heat certain regions of a quantum well structure and therefore generates a multi-bandgap sample [18].

This method has the prospective to create intermixed material with exceptional optical and electrical properties. Nevertheless, its spatial selectivity is restricted by the laser spot size and the heat lateral diffusion inside the active region. This approach was also used to produce various types of photonic integrated circuits such as multi-wavelength laser diode arrays and modulator/laser diode chips etc [107,18].

### 3.13.2 Pulsed Laser Induced Disorder

Pulse laser irradiation was explored to learn the QWI in QW structures based on InP [108] or GaAs [63]. Similar to the previous approach, laser light is absorbed in the quantum well. Laser pulses can quickly heat the crystal lattice. The quick thermal dilation splits molecular bonds and modifies the crystal lattice. This increases considerably the local concentration of point defects [109]. As laser pulses do not

provide enough energy to initiate the inter-diffusion, an extra annealing treatment is required. This treatment can be achieved in a rapid thermal processor [19] or with a continuous wavelength laser [10]. In the later case, to stop the surface desorption of group V atoms, Qiu and his group coated a  $\text{Si}_x\text{N}_y$  or  $\text{SiO}_2$  cap on top of the QW structure. Such a cap layer can also improve ( $\text{SiO}_2$ ) or restrain ( $\text{Si}_3\text{N}_4$ ) the intermixing process. Spatially resolved PL measurements on QW sample partly covered with a patterned reflective gold mask (Figure 3.18) illustrated that the spatial resolution of this technique is about of  $2.5 \mu\text{m}$  [19]. Time resolved spectroscopy reveled that after laser irradiation, the carrier lifetime can be decreased by one order of magnitude [11]. This approach was utilized to produce multi-wavelength laser diodes [19] and electro-absorbing modulators [12]. This technique was also used as an in-situ wavelength trimming means for DFB lasers [13].

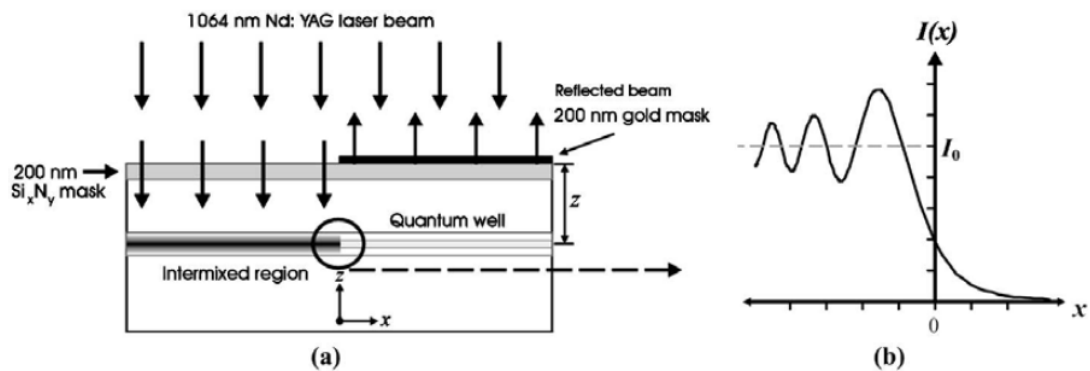


**Fig. 3.18 a: Laser irradiation using a patterned reflective gold mask, b: diffracted laser beam's intensity plot in the QW layer [19].**

The micrometer level spatial resolution makes both continuous wave and pulsed laser QWI techniques attractive for photonic device fabrication. These techniques have the potential to fabricate material appropriate for attaining complicated integrated photonic devices especially when considering the large amount of microelectronic processes based on identical laser processing technologies that guide to a high reliability of these systems.

### 3.13.3 Ultra-Violet Laser Induced Quantum Well Intermixing

UV-laser interaction with surfaces of the semiconductor structures can be carried out without damaging the material located deeper than, usually, 10-20 nm. This way, a layer of disordered material with large concentration of structural defects can be created, e.g., without causing lasting harm to the active region of the QW structure.

As a result, the UV-laser QWI approach has the potential to produce integrated photonic devices with minimum compromised parameters associated with laser induced defects. Excimer lasers, which have previously been utilized in microelectronics (repairing masks, thin film annealing and high resolution photolithography) can also be used at the semiconductor surface to activate atmosphere-dependent chemical reactions.

In UV-laser controlled QWI, the surface of the QW structure is irradiated selectively by UV-laser pulses (Figure 3.19) to introduce the formation of point defects or modify the chemical stoichiometry near the surface layer [114]. After that, the QW structure undergoes an annealing step at high temperature for a small period of time (30-120s) to induce QWI. Since UV photons are quickly absorbed by the cap layer of the semiconductor, it is probable to control the macroscopic changes to a comparatively thin (sacrificial) layer, which can be wet etched after the annealing treatment. This makes it likely to get rid of the effect of laser created residual defects on characteristics of devices produced from the intermixed material [93].

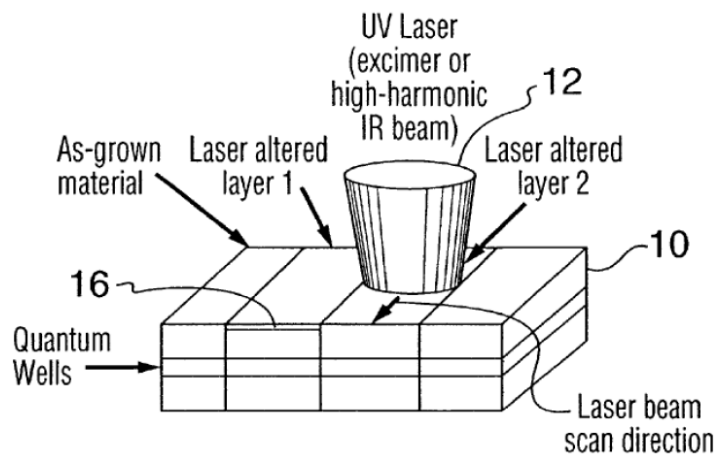


**Fig. 3.19 UV laser irradiation of QW structure allows obtaining selective area QWI [114].**

To illustrate the potential of this approach, an InP-based QWI structure was irradiated using KrF excimer ( $\lambda = 248$  nm,  $\Delta t = 30$  ns) laser pulses of fluence in the range of  $100 \text{ mJ/cm}^2$  [114]. Two exposition regions, marked by a laser mask projection procedure were irradiated using 500 and 1000 pulses. The sample was then annealed at  $750^\circ\text{C}$  for 10 seconds. The annealing process produced a 6 nm blueshift in the untreated region, while the quantum well intermixing regions blueshifted 29 nm and

56 nm exposed with 500 and 1000 pulses respectively. This approach was also lately utilized to intermixed InGaAs/GaAs quantum dots [115].

### 3.13.3.1 Influence of UV Irradiation Parameters on Quantum Well Intermixing

As discussed previously, the depth at which laser can creates defects highly depends on the energy or the wavelength of the incident photons. Figure 3.20 presents absorption coefficients  $\alpha$ , for InP and GaAs as a function of photon energy. For energies greater than that of the semiconductor bandgap, the absorption coefficient increases rapidly, which gives a shallower absorption depth. Nonetheless, heat diffusion processes can extend laser created defects to depths notably beyond those of the absorption length  $\alpha^{-1}$ .

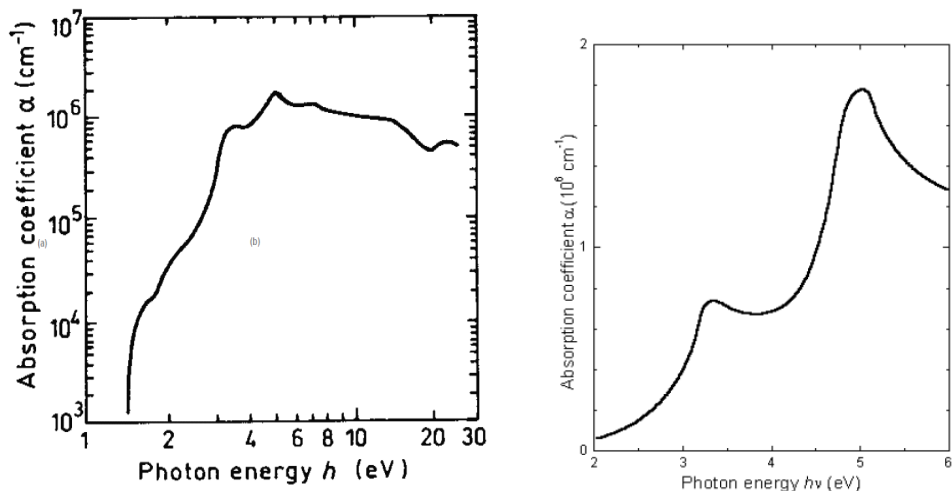


**Fig. 3.20 An example of Absorption coefficients as a function of incident photon energy for a: GaAs [116] and b: InP [117]**

The sample reflection coefficient (Figure 3.21) also affects the processes of defects creation since it affects the transmitted power density.

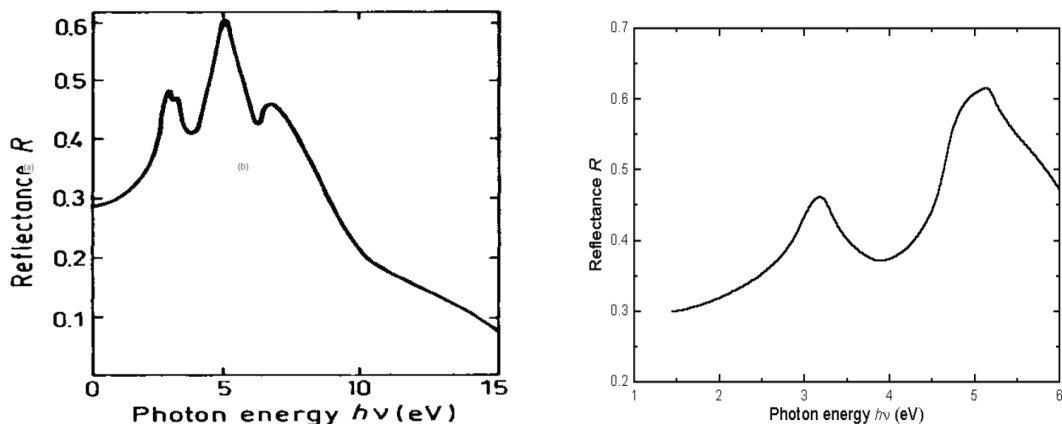


**Fig. 3.21 Reflection coefficients vs normal incident photons energy for a: GaAs<sup>[118]</sup> and b) InP<sup>[117]</sup>**

The interaction of laser pulses with semiconductor material also relies on the temporal length of the laser pulses used. For instance, the ablation threshold reduces as the pulse length decreases as shown in figure 3.22. While using ultra-short pulses, thermal conduction is negligible and can be ignored. The interaction volume is then controlled by the absorption thickness  $\alpha^{-1}$ . The defect creation process is also affected by the pulse length. Though under longer pulses, the thermal influences are deeply accountable for expelling matter out of the target, under ultra-short, it is linked to photomechanical processes <sup>[119]</sup>.

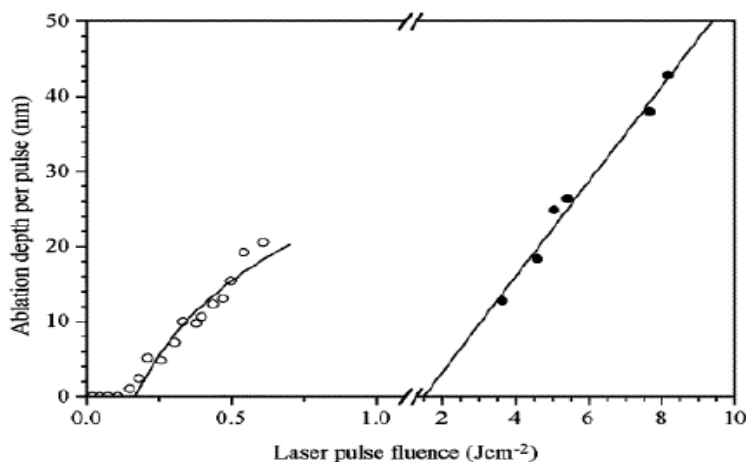


**Fig. 3.22 An example of Ablation depth of a copper target as a function of KrF laser ( $\lambda=248$  nm) energy density (short •, 0.5 ps) and long (○, 20 ns) pulses<sup>[120]</sup>.**

The repetition rate of laser pulse also has a small affect on the dynamics of laser matter interaction. During each pulse, the temperature within the interaction volume raises and gets to its maximum. The heat then diffuses to the semiconductor substrate.

The material's surface can return to its original temperature if the time in between each pulse is large enough. In this case, each pulse is autonomous. In contrast, if the period is smaller than the heat diffusion time then the heat accumulates as the quantity of pulses increases and new reactions can be initiated. For example, in case of UV-laser enhanced oxidation of GaAs, a modification of the surface temperature changes the oxidation dynamics. Fast pulses would some time help the preferential formation of a non-stoichiometric gallium oxide whereas slower ones would create an oxide with same extent of gallium oxide and arsenic oxide.

UV-lasers are extremely attractive tool for post-growth processing of semiconductor wafers due to their versatility. As the photon's penetration depth in the QW structure depends on the photon wavelength, the disordered layer thickness and the defects concentration can be accomplished by carefully selecting the laser wavelength and the irradiation dose. Excimer laser can also be utilized to process fairly large areas in a single step, similar to the coverage area realized by the excimer based photolithography technique. They can produce surface heating, creates near surface defects and change the surface chemistry [21].

### **3.14 Summary**

In this chapter, I explained QWI and presented a brief review of various QWI techniques. I discussed the benefits and draw backs of each technique. I put more emphasis on techniques based on laser technologies as I also use this technique to fabricate lasers diodes and waveguides for monolithically integration of photonic devices. Nevertheless, I also put some importance on the impurity free vacancies disordering technique, such as UV-laser controlled quantum intermixing, it also induces intermixing by modifying the QW material's surface properties. The main points of this chapter can be summarized as follows.

Quantum well intermixing is a technique initiated thermally. It modifies the shape of a quantum well from a square-like well to a smoother form which increases the location of the discrete energy levels inside the well and alters the material bandgap.

The intermixing process is accelerated by the existence of point defects in the well area. Impurity induced disordering is a well reported and well known technology. Though, as it increases the optical losses in the active section of the QW, it is inappropriate for passive optoelectronic devices. In addition, it also increases the power consumption in active devices.

Impurity free vacancies disordering is a comparatively simple technique to realize QWI. This technique uses different capping layers to enhance and suppress the blueshifts. It is very efficient for GaAs based QW structures, but has illustrated limited success in InP based structures. Since defects are generated at the surface, the spatial resolution of this approach is limited by the lateral diffusion of point defects and relies on the position of the active region underneath the surface of the QW material. It is hard to control the quality of dielectric cap and that leads to reproducibility problems.

The “universal damage” technique, or silica sputtering technology, has the benefit of working well on both InP and GaAs based QW structures as the point defects are generated in both by the sputtering damage and the surface out-diffusion in the dielectric layer. Yet, it is tricky to control the quantity of generated defects and therefore reproducibility becomes a main problem. This approach reduces the material quality. Ion implantation caused QWI works practically well for both GaAs and InP based QW structures. Models of defect generation are also accessible for this technique. When ions are implanted, defects can be created at the preferred depth by modifying the ion specie or the acceleration energy. Nevertheless, realizing multi-bandgap wafers need multi-steps implantation or grey tone masking which is not easy to reproduce. Shallow ion implantation achieved by using reactive ion etcher or an induced coupled plasma etching system would be an attractive choice to implant sample without using a pricey ion implanter. Moreover, under high energy acceleration, ion implantation left behind residual damage near the active region which decreases the devices performances.

UV-lasers can be used effectively to produce QWI promoting defects since they are absorbed in a very thin volume of the surface layer. The laser can also change the

chemical stoichiometry of the top surface layer therefore the modified layer improves or prohibits diffusion of point defects towards the quantum well active region. The UV-lasers are potentially attractive tools for the fabrication of PICs with surface heating and possibility to modify the surface chemistry,

## 4 UV-laser Induced Quantum Well Intermixing and Photonic Integrated Devices

### 4.1 Introduction

In this chapter I first explain the procedures and experimental setup required to investigate UV-laser based QWI. The first section of the chapter presents principles of UV-laser, quantum well intermixing based on UV-laser technique and discusses interesting experimental results. The second section demonstrates the applications of this technique for fabrication of photonic devices that could lead to monolithic integration.

It is known that the absorption of UV-laser radiation by solids can induce disruption to the lattice and lead to the intermixing effect. The bond strength of InP is weaker than the bond strength of InGaAs. Thus, by using an InP top sacrificial layer we can achieve higher concentration of point defects with even low UV-laser fluences in the sacrificial layer while the InGaAs surface remains undamaged which is necessary for the fabrication of photonic devices on the QWI altered material. The resulting material can have high optical and electrical quality.

Previous published work demonstrated blue shifts up to 130nm using unstrained InGaAs/InGaAsP QW laser structure. Here, we report superior experimental results with wavelength blue shifts as large as 142 nm in compressively strained InGaAsP/InP QW laser structure using the combination of UV-laser irradiation process and rapid thermal annealing treatment. We show that the photoluminescence (PL) intensity can be enhanced with reduced linewidth under certain UV irradiation conditions, possibly due to the change of strain distribution in the QW that alters the band structure and enhances the Fermi occupation factor. By using a thick InP sacrificial layer that is removed after UV irradiation and RTA, little surface damage was observed which might affect the device performance.

As we know that the photonic integrated devices are based on the integration of active lasers and low-loss passive waveguides [124-126]. In order to investigate the

versatility of the UV-laser quantum well intermixing approach, we fabricated and then characterized two devices using this technique. Firstly, fabrication procedures and the results of low-loss passive waveguides, transparent at 1545 nm are discussed. Secondly FP cavity lasers were fabricated and characterized to observe the low threshold current and large lasing wavelength shift while keeping the same emission spectra's profile.

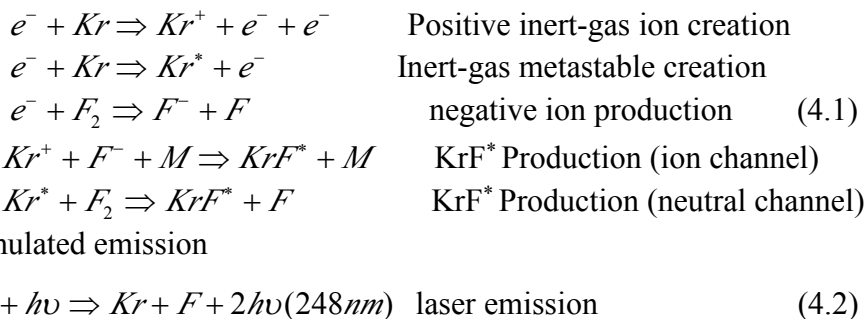
## 4.2 Excimer Lasers

Most powerful lasers existing in the UV spectrum are excimer lasers. The name excimer represents the expression excited dimer which is a kind of molecules created by the combination of two similar atoms or constituents in excited state. Though, nowadays the name excimer is used by principle because mainly “excimer” lasers are made from rare gas monohalides also called exciplexes (excited complexes). Exciplexes only exist in excited state. Rare gases like Ar, Kr or Xe and halides such as F and Cl are used to form the exciplexes [127]. Excimer laser transitions can be utilized to generate wavelengths between 126 nm in case of Ar<sub>2</sub> and 660 nm by Xe<sub>2</sub>F. However the most regularly used laser gas mixtures are fluorine (F<sub>2</sub>,  $\lambda = 157$  nm), argon fluoride (ArF,  $\lambda = 193$  nm), krypton fluoride (KrF,  $\lambda = 248$  nm), xenon chloride (XeCl,  $\lambda = 308$  nm) and xenon fluoride (XeF,  $\lambda = 351$  nm).

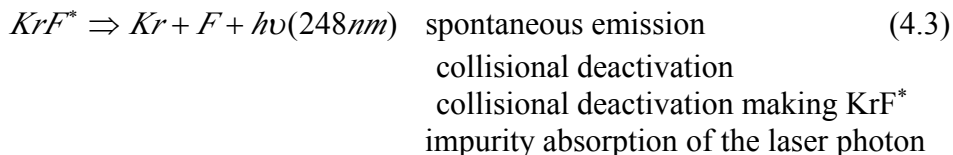
The making of the energized excimer molecules depends on a complex plasma reaction. This happens when the gas is put forward to an electrical discharge. The creation of the energized molecule is dominated by two procedures such as the neutral channel and the ion channel (Figure 4.1). For instant, in case of a KrF laser, both reactions happen in few nanoseconds leaving the energized KrF\* molecule at the lowest of the potential energy curve of the upper state. The KrF\* complex perishes after some nanoseconds through the emission of a 248 nm (wavelength) photon and splits into Kr and F. The Kr and F elements are subsequently available for a further excitation cycle. As the KrF molecules do not survive in their unexcited state, that's why KrF and other excimer lasers fit into the four energy levels group of lasers. This means that emission process does not experience the ground state dissemination and therefore has a comparatively high efficiency. Due to the fast loss processes in the

laser cavity and short life time of the energized exciplexe, pump power densities beyond  $1 \text{ mW/cm}^3$  are required to effectively excite the excimer lasers. These power densities can only be attained by pulsed systems that prevent excimer lasers from function in constant wave mode.

The following mathematical equations describe the detail of the various chemical reactions happening in a KrF laser. Similar equations can be used to explain additional excimer and exciplexe reactions <sup>[127]</sup> pumping.



#### Losses



In equations (4.1), (4.2) and (4.3), \* presents the excited status of an atom or a molecule, M is used for a third body - normally an atom from buffer gas, where as X stands for impurity in the laser gas.

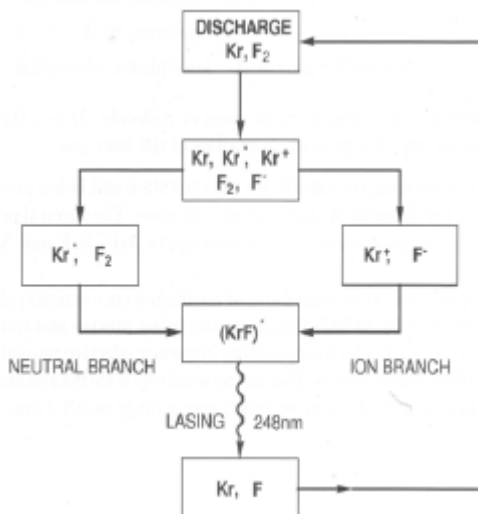


**Fig. 4.7 Excitation kinetics of the UV KrF excimer laser [127]**

Excimer lasers are the well known laser system to accomplish laser ablation. Because the UV wavelengths are normally absorbed in a shallow section of material close to the surface, excimer lasers present an excellent control of the ablation strength and of the depth of the operated layer. The pulse duration also offers irradiation peak power up to  $10^{10}$  W/cm<sup>2</sup>. Excimer lasers are utilized in the industry of microelectronics for photolithography at 248 and 193 nm [128], and annealing of amorphous silicon that are used for applications of flat panel display [129]. These laser systems have also been employed for micromachining and surface patterning [130,131], chemical or physical modification [132,133] and for hole boring in electronic circuit packaging [134]. Further, excimer lasers are also utilized as a source of excitation for pulsed laser deposition of elevated quality material [135].

#### 4.2.1 KrF Laser Characteristics

Prior to investigate quantum well intermixing, it is imperative to realize the behaviour of the instrument we are using. The status of the excimer laser might have vast influence on the process of intermixing. Figure 4.2 presents the temporal pulse profile of the KrF laser. It shows the pulse profile for two different pulse fluences i.e., 200 mJ/pulse and 600 mJ/pulse, before and after the container was refilled. Although, the deposited energy was equal before and after the refill, the maximum power was approximately twice higher for the new gas mixture than that of the older one. At 600 mJ/pulse, we even noticed the dissemination in the peak power of the older gas pulse (Figure 4.2).

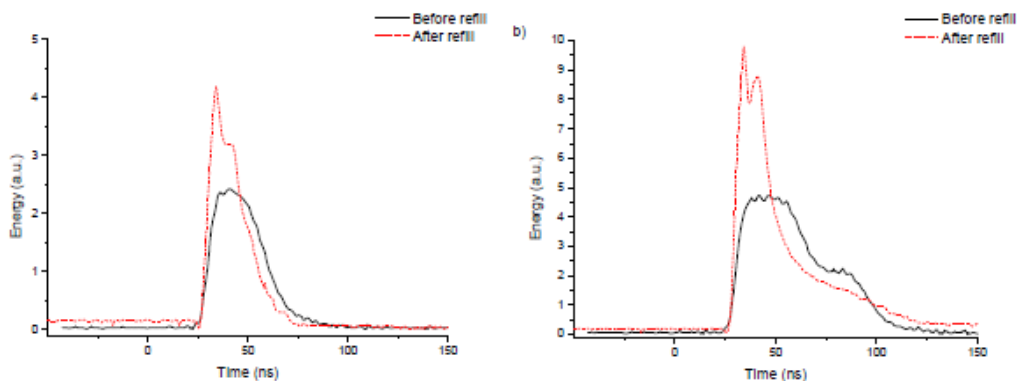


**Fig. 4.2 KrF excimer laser temporal pulse shape relies on age of the gas mixture for pulse fluences of a: 200 mJ/pulses and b: 600 mJ/pulses.**

The time period of the gas mixture also affects the stability of the energy density of each pulse. As it delivered lesser peak power, for the equal pulse energy, an older gas mixture presented better stability than a newer one (Figure 4.3). Furthermore, for the old gas mixture and for the new gas mixture, the laser stability expected to get better when the delivered energy increased. Though, in case of pulse total energy, the older gas mixture demonstrated a problem of its stability when getting pulse energy above 400 mJ/pulse. This occurred as we noticed the creation of a shoulder in the temporal pulse profile of the older gas mixture laser pulse. The fluctuations of the secondary pulse peak added to the general instability of the pulse total energy.

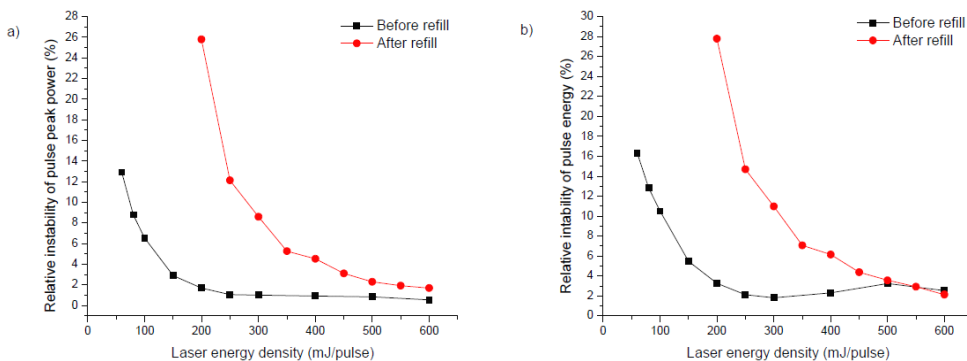


**Fig. 4.3 Instability of pulse of KrF excimer laser, a: peak power and b: total energy as a function of pulse energy.**

### 4.3 InGaAsP/InP Heterostructure

This section describes UV-laser induced quantum well intermixing technique on the standard compressively strain InGaAsP/InP, five quantum well epitaxial wafers. The PL spectral peak corresponds to the QW electron-hole recombination peak, which for the as-grown material is obtained at 1553nm. The specific layer structure of the used laser quantum well structure is given below.

The investigated sample of InGaAsP/InP laser structure contains five 1% compressively strained  $\text{In}_{0.8}\text{Ga}_{0.2}\text{As}_{0.8}\text{P}_{0.2}$  QWs with unstrained 1.25Q InGaAsP barriers. From the surface the layers are a  $0.5\mu\text{m}$  Zn-doped ( $10^{18}\text{cm}^{-3}$ ) InP sacrificial layer,  $0.2\mu\text{m}$  Zn-doped ( $10^{19}\text{cm}^{-3}$ )  $\text{In}_{0.53}\text{Ga}_{0.47}\text{As}$  cap,  $1.5\mu\text{m}$  Zn-doped ( $10^{18}\text{cm}^{-3}$ ) InP cladding,  $0.004\mu\text{m}$  Zn-doped ( $4\times 10^{17}\text{cm}^{-3}$ ) 1.3Q InGaAsP etch-stop layer,  $0.15\mu\text{m}$  Zn-

doped ( $4 \times 10^{17} \text{ cm}^{-3}$ ) InP cladding, five repeats of 10nm undoped InGaAsP barrier ( $\lambda_g = 1.25 \mu\text{m}$ ) and 5.5nm undoped In<sub>0.8</sub>Ga<sub>0.2</sub>As<sub>0.8</sub>P<sub>0.2</sub> QW which are sandwiched by two 0.06μm InGaAsP step-graded index separate confinement layers with the bandgap wavelength  $\lambda_g$  varying from 1.05μm to 1.25μm, and 1.5μm Si-doped ( $2 \times 10^{18} \text{ cm}^{-3}$ ) InP buffer on Si-doped ( $4 \times 10^{18} \text{ cm}^{-3}$ ) InP substrate.

#### 4.4 Irradiation Setup

For this project, I used two different excimer laser irradiation setups. The first one used is a krypton-fluoride (KrF) laser and was located at the Laboratory for Quantum Semiconductors and Photon-based BioNanotechnology, Interdisciplinary Institute for Technological Information (3IT), Université de Sherbrooke, Sherbrooke, Québec J1K 2R1, Canada (Figure 4.4).

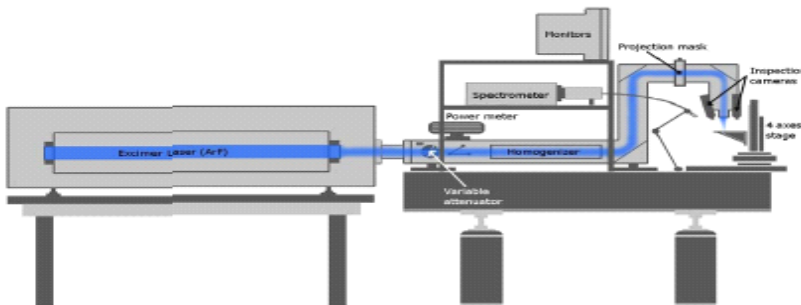


**Fig. 4.4 Irradiation setup of the ArF excimer laser**

The KrF ( $\lambda = 248 \text{ nm}$ ) laser setup (Lumonics, Pulse Master 800) which delivered pulses of nearly 23 ns with maximum energy of 200 mJ/pulse. The laser beam was formed using micro-lenses array also called beam homogenizer to a  $12 \times 19 \text{ mm}^2$  beam which has a top hat profile. Incident light intensity on the QW sample can be controlled by a variable attenuator. To shape the delivered beam at the sample surface, a projection mask was utilized (Figure 4.4). With an x-y-z-theta mechanical stage, location of the QW sample was controlled using a lateral resolution of less than  $10 \mu\text{m}$ . To monitor macroscopic alterations of the QW sample surface due to the irradiation of UV-laser, two inspection cameras were utilized.

The second setup used krypton-fluoride (KrF) laser and was located in the Laboratory of Integrated Photonics at the Zhejiang University Hangzhou. Following section presents the KrF laser irradiation setup used at our University.

#### **4.4.1 ProMaster (KrF laser)**

The KrF laser ( $\lambda = 248$  nm) used in the ProMaster is the SP 300i short pulse excimer laser manufactured by ATL Lasertechnik which delivered 22 ns pulses. The setup allowed irradiation under different atmosphere (Figure 4.6). A fused silica with anti-reflection coating was used as a mirror allowing delivery of the laser beam to the environmental chamber. The setup allowed irradiation in oxygen, nitrogen and ammonia.

In general, setting of laser parameters, operating mode, gas supply control etc, can be controlled either by the hand-held control unit OR via RS232 from the ATL Laser control program installed on the ProMaster PC. In general, it is found advantageous to operate the laser in the energy stabilized mode, for constant O/P energy. To prolong gas fill lifetime, and intervals between optics cleaning, the laser should always be operated at the lowest energy necessary to perform the process.

The Optec ProMaster is a complete, high performance, multi-featured excimer laser workstation in a tabletop package. Excimer relies on the interaction between UV pulsed laser radiation and the material to be irradiated. The short wavelength means that radiation is efficiently absorbed in the surface layers of all but a few materials; the short pulse duration ensures high peak absorbed power densities. The combination of UV & short pulse results in the removal of surface layers by one of a number of mechanisms, i.e., Vaporization in the case of metals and ceramics, molecular disintegration (Photoablative decomposition) for many polymers at  $< 300$  nm, or interface effects (stripping by exfoliation of thin films up to a few  $\mu\text{m}$  thick). Energy densities are typically in the range of 1-10  $\text{J/cm}^2$  at rep. rates up to a few hundred Hz, irradiation takes place at rates of tenths of  $\mu\text{m}/\text{shot}$ .

#### **4.4.2 Masks**

Excimer beams have typically broad spatial profile, and poorly defined mode structure. Unlike other lasers, focal point applications are rare, most processing is performed using projection optics, where the beam is used to illuminate a mask,

whose demagnified image is then focused on the part in accordance with the well-known formula

$$\frac{1}{u} + \frac{1}{v} = \frac{1}{f},$$

Where f is the focal length of the projection lens used, u and v are the object (mask) and image (part) distances respectively. The mask may define a simple motif, e.g; circle, slit, or more complex motifs which are then projected as a whole onto the part. The final irradiation on the part can be built up from repetition of selected motifs associated with part motion in X,Y and laser firing; irradiating depth is mainly controlled by local shot dose.

#### 4.4.3 UV Illumination Optics

The role of the UV illumination optics is to match the laser O/P to the mask size/shape, to the useful aperture of the imaging lens, and to set the energy density; resulting e.d, on the part is multiplied by the square of demagnification. Energy density is set to conform to a process window, or to accentuate/minimize some processing feature, e.g; low taper, illumination optics typically include steering mirrors and energy controller, and may also include other elements such as beam expanding telescope(BET) or beam concentrator, beam shaper or homogenizer, field lens etc, or anamorphic(cylindrical) optics. Illumination optics design strives to use the beam efficiently, and also has to take into account evolution of the beam profile over gas fill, cavity lifetime (Figure 4.5).

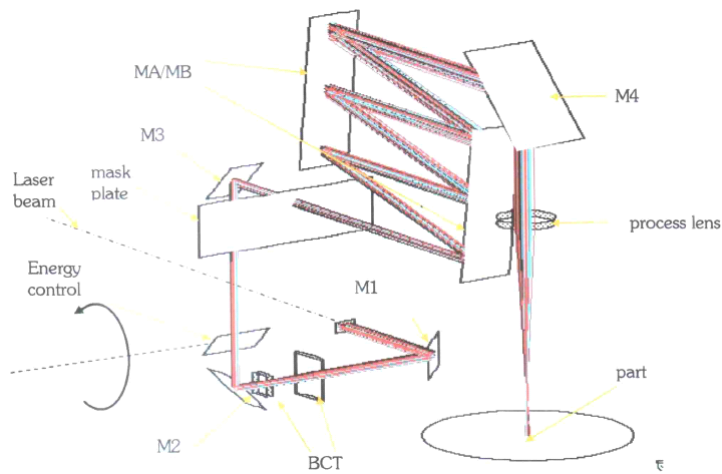


**Fig. 4.5 Projection optic layout of the ProMaster system**

#### **4.4.4 Image Projection Lens**

Image precision will be ultimately limited by the optical resolution of the imaging or process lens, as determined by useful n.a.(numerical aperture). Low cost singlets can be used at low n.a. or where the desired processing precision is such that aberrations can be tolerated. Diffraction limited multi-element lenses of higher n.a. are optimized for desired demagnification. Significant working distance is desirable to avoid damage by ablation products, leading to focal length typically in the range 50-150mm. Generally process lens is fixed to some kind of focus mechanism which may be motorized. If part alignment is to be performed it is desirable to view the part through the lens (TTL vision). And lens performance at visible wavelengths must be then adequate for the task.

#### **4.4.5 Vision Systems**

Vision system includes TTL or other inspection optics, where magnification is selected either for area viewing or fine inspection/alignment. Adequate and flexible part lighting must be provided, particularly when PRS (pattern recognition S/W) is used for automation. We can include in vision systems highlighting, whereby a visible light source is positioned on the laser side of the mask (behind a dichroic mirror), so that with a suitable process lens, the pattern to be irradiated is indicated on the part in highlight prior to actual irradiating.

#### **4.4.6 Environment**

Excimer processing, particularly of polymers, often benefits from a shield gas (He) during processing, whilst process debris/fumes must be safely extracted from the process area and taken to a suitable exhaust.

#### **4.4.7 Process Control**

Successful execution of a process generally requires coordinated and /or synchronous control of laser energy and firing, mask selection/control, and part motion. Simple repetitive tasks can be adequately controlled by PLC, but many

systems use PC control, also running ancillary systems such as PRS, environment control, safety monitoring, data logging etc.

#### **4.4.8 ProMaster System Architecture**

The ProMaster (PM) is designed as a table-top workstation. The ProMaster BDU simply clips onto the front of the laser source, and can be mounted on any solid support (Figure 4.6). The electrical rack which also houses the industrial PC main unit can be floor mounted, whilst flat screen, keyboard, mouse and joystick are positioned as convenient for the operator.



**Fig. 4.6 ProMaster excimer laser tabletop workstation**

#### **4.4.9 Laser**

The ATL SP300i short pulse excimer laser sits behind and partly supports the ProMaster BDU; the associated vacuum pump and halogen filter are sited conveniently beneath the support table or within the PM-Int cabinet when this option is chosen. The laser is connected by s/s pipe-work to the gas supply system; gas supplies and regulators (supplied), and can either be fixed conveniently using gas cylinder restraining straps or installed in a separate gas cabinet. Laser ON/OFF controls are accessible at the rear of the laser, the laser beam exits forwards into the ProMaster BDU.

#### **4.4.10 ProMaster BDU**

The o/p beam from the laser connects directly into the ProMaster BDU, which integrates in a single unit illumination optics, mask support, projection optics, vision/environment systems etc, and is built on a natural granite base upon which the

part motion equipment is fixed. The complete unit is enclosed by a dust and safety cover with visor.

The motorized mask selector (32P) translates a pre-cut and interchangeable mask plate with 32 different motifs. An option is a motorized variable rectangular aperture MVA which is designed to be used together with the 32P translator, to create an almost limitless range of combination motifs held in PC memory as “virtual masks”. Electrical connections to the ProMaster are made via terminal blocks within the BDU.

#### **4.4.11 Part Motion**

Parts to be irradiated are held on a small vacuum chuck, which is mounted 100mm travel, 1 $\mu$ m resolution X,Y stages fixed to the granite base of the ProMaster BDU. Drivers for the stages are situated in the electrical rack. A theta stage allows free rotation over 360° and micrometer driven correction of +/5°.

#### **4.4.12 Controls**

Part lighting intensity and UV% energy control are manually set from the user panel on the r.h., PM side. All other PM functions are controlled by the on-board industrial PC, whose main unit is situated in the electrical rack. This PC also houses the motion controller, joystick and frame grabber cards. PM operation is controlled by Process Power PM, a unique Optec program allowing synchronization of laser, BDU settings and part motion, with many user-friendly features. Flat screen PC monitor, with keyboard, mouse and joystick are positioned to suit operator convenience. Power supply (100-220V a.c.) is directly connected to the PM rack, which houses general electrical distribution plus all motor drives and interface cards.

### **4.5 Characterization Techniques**

For the characterization of optoelectronic devices, luminescence spectroscopy is one of the powerful tools used. It is a nondestructive method that can give information on elementary properties of semiconductors. It is also responsive to different impurities and defects that influence the QW material's optical and electrical properties and device performance. Luminescence is the term that represents light

emission after some energy was injected in the material. There are many ways to stimulate under observation sample to cause luminescence. The most general method is Photoluminescence in which light emission is stimulated by revealing the semiconductor material to light by higher energy than the energy of the luminescence light. Photoluminescence is also called fluorescence if the emission happens less than about 1  $\mu\text{s}$  after the excitation and phosphorescence, if it takes long time up to hours and days for the emission.

Another potential method to excite the under observation sample is by using an external current. This process is called electroluminescence. Electroluminescence is particularly imperative in the production of optoelectronic devices like Light Emitting Diodes (LED), and Lasers. The principal technique used in this work was photoluminescence (PL). It measures the intensity and energy of radiative transition. It can thus characterize the extent of bandgap shift and gives a qualitative idea of the material quality.

#### **4.5.1 Principle of Photoluminescence**

For measuring the band-gaps of materials, photoluminescence (PL) is a non-destructive optical method used for the characterization, investigation, and detection of point defects. It involves the irradiation of the semiconductor material to be characterized with photons having energy greater than the bandgap energy of the under observation material. The incident photons will create electron-hole pairs in the example of a crystal scintillator. Once these electrons and holes recombine, this recombination energy will convert partially into non-radiative emission and partially into radiative emission (Figure 4.7).

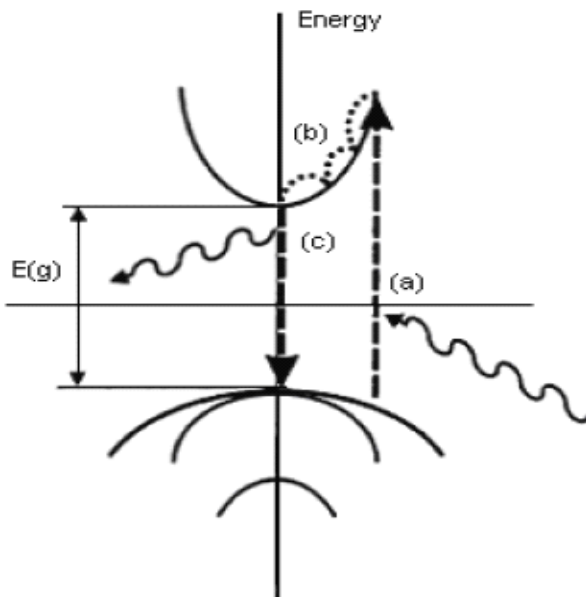


**Fig. 4.7 Photoluminescence schematic.** (a) An electron absorbs a photon and is promoted from the valence band to the conduction band. (b) The electrons cools down to the bottom of the conduction band. (c) The electron recombines with the hole resulting in the emission of light with energy  $h\nu$ .

PL consists of impinging comparatively high energy ( $h\nu > E_g$ ) light onto a material, exciting electrons of the atom. Following relaxation may result in the creation of photons that are properties of the crystal or defect site that emits light. The detected PL signals could be due to the band to band recombination, defects of the intrinsic crystalline (growth defects), dopant impurities (introduced during growth or ion implantation), or other extrinsic defect levels (due to radiation or thermal effects). While bombarded with photons of energy higher than the bandgap of the under observation material, an impurity energy level can emit certain photons via numerous different types of radioactive recombination processes, allowing the final PL spectra to be used to examine the precise type of semiconductor defect. This interaction gives an extremely sensitive, qualitative measurement of resident and extrinsic impurity levels found inside the material bandgap. We may briefly articulate PL process consists of three main phases

1. Excitation- Energy of external sources can be absorbed by electrons, like lasers, arc-discharge lamps, and tungsten-halogen bulbs, and they jumped to higher energy levels. Electron-hole pairs are created in this process.

2. Thermalization- Energized pairs rest towards quasi-thermal equilibrium distributions.
3. Recombination- The energy can then be released, in the shape of a lower energy photon, when the electron drops back to the normal ground state. This process can happen radiatively or non-radiatively.

#### 4.5.2 Recombination Mechanism

An electron is excited from the valence band into the conduction band leaving behind a hole, once a semiconductor absorbs a photon of energy higher than the bandgap. When the electron comes to its normal state, it can do so via radiative (release of a photon) or non-radiative (no photon creation) recombination. When the electron-hole recombines via radiative recombination, a photon is released and the energy of the released photon depends on the modification in energy states of the electron-crystal structure.

Indirect bandgap semiconductor like Si requires the help of a phonon (energy in the shape of lattice vibrations) for photon emission to preserve the momentum inside the lattice structure. Discrete energy levels are formed within the semiconductor's forbidden energy gap with the introduction of impurities in semiconductor material. Shallow donor levels are tagged as levels just under the conduction band, while shallow acceptor levels are tagged as levels situated above the valence band. These donor and/or acceptor level traps can work as recombination points for transitions inside the bandgap. Information about the impurity or defect can be resolved by investigating the nature of these trap levels. Figure 4.8 shows the energy band figure of a semiconductor, illustrating the most general radiative and non- radiative transitions. Free electrons occupy the conduction band  $E_C$ , and free holes occupy the valence band  $E_V$ , are shown in addition to donor  $E_D$  and acceptor  $E_A$  trapping regions within the prohibited gap. The shown transitions are free-to-bound transition, band-to-band transition, excitonic transition, donor-acceptor pair transition and auger transition [26].

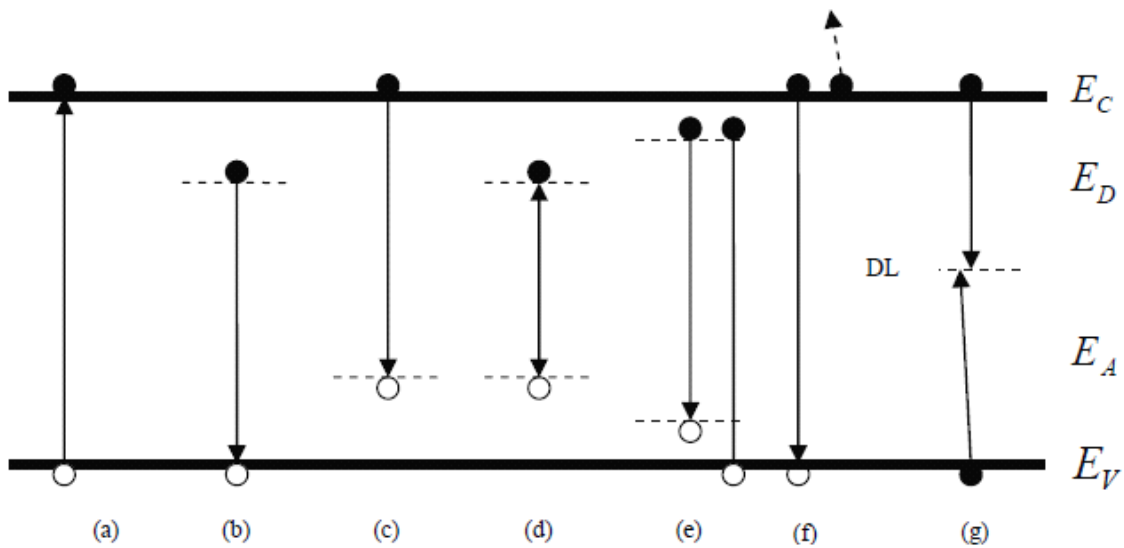


**Fig. 4.8 Most common radiative transition observable with photoluminescence and non-radiative transitions.**

Further the recombination of the electrons-holes at the top of the valence band  $E_V$  results in the release of photons of wavelength equivalent to the bandgap energy of the semiconductor. These transitions are particularly noticeable at low temperature.

The intensity of the PL signal also gives important information on the quality of the under observation QW sample. For instance, weaker signal is normally recognized as a high density of surface states<sup>[122]</sup>. Additional non-radiative processes linked to the existence of defects are also accountable for quenching the PL signal. The full width at half maximum (FWHM) of the obtained PL signal is frequently considered as a pointer of the quality of the under observation QW sample. According to Heisenberg uncertainty principle (equation 4.4), widening of the PL peak is linked to shorter carriers lifetime. This PL peak broadening (shortening of the lifetime) could be due to the change in the confinement<sup>[47]</sup>, the creation of trapping defects or the relaxation of strain<sup>[123]</sup>.

$$\Delta E \Delta t \geq \frac{\hbar}{2} \quad (4.4)$$

## 4.6 UV-Laser Processing of the QW Material

To achieve large bandgap blueshift of the InGaAsP/InPlaser structure, the sample was irradiated by a UV-laser with different parameters of energy and number of pulses. We used KrF excimer laser ( $\lambda = 248\text{nm}$ ) which delivered 22ns short high energy pulses of fluences in the range of 50-200 mJ/cm<sup>2</sup>. The sample was irradiated at room temperature and at normal incident to the surface. The pulse repetition rate was 10Hz. The laser beam was not homogenized and the spots of almost rectangular shape were created on the sample surface without using a mask. The X-Y-Z positioning of the sample was controlled by a computer. The UV-laser setup allowed for the processing of the same sample at numerous sites, each measuring approximately 600 \* 500  $\mu\text{m}^2$ . After being exposed under UV-laser, the wafers were then annealed in a nitrogen atmosphere using rapid thermal annealing at temperature 750 °C for 120s along with a sample which had not been irradiated. During the annealing, samples were placed between two Si wafers to prevent desorption of the group V elements. Since numerous sites of the same sample could be processed with different laser parameters, the annealing conditions were the same for different spot sites. The possible damage generated during the UV-laser process was then investigated before and after rapid thermal annealing (Figure 4.9).

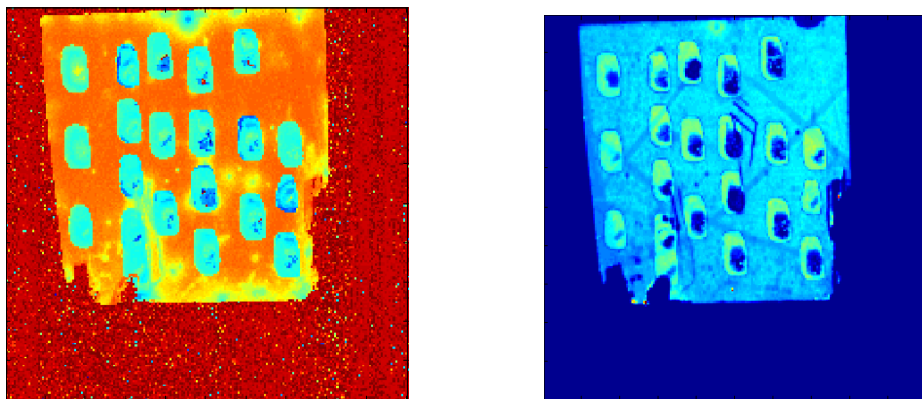


**Fig. 4.9 Room temperature PL map of a KrF laser processed InGaAsP/InPMQW damage sample following rapid thermal annealed at 750°C for 120s.**

## 4.7 Etch rate

After RTA the under observation sample's sacrificial layer was removed prior to PL measurement. As was mentioned earlier that it is very important to etch each layer separately without affecting the underneath layers, different acid solutions had to be mixed and prepared. After being etched, each sample was then rinsed off and dried. The following table presents the etch rate.

**Table 4.1 Etch rate of top layers of InGaAsP/InP laser structure**

Material to be Etched	Wet Etchants	Temperature	Time
Sacrificial layer	HCL:H <sub>2</sub> O (3:1)	Room temp.	30sec
Cap layer	H <sub>3</sub> PO <sub>4</sub> :H <sub>2</sub> O <sub>2</sub> :H <sub>2</sub> O (1:1:8)	Room temp.	50sec
Cladding layer	HCL:H <sub>2</sub> O (3:1)	Room temp.	30sec

Detailed information about laser irradiation conditions, the achieved blue shifts and the averaged PL intensity for each site shown in Figure 4.7 is collected in Table 4.2.

**Table 4.2 Processing parameters and PL results**

Spot	No. of Pulses	Pulse Energy (mJ/cm <sup>2</sup> )	Blue Shift (nm)	Intensity (nW)	FWHM (nm)
As-grown	0	0	0	1.92	93.4
RTA-only	0	0	23	1.7	109
A1	50	50	98	2.7	80.6
A2	100	50	103	2.3	77.6
A3	150	50	102	2.3	75.7
A4	200	50	122	2.6	84
B1	50	100	103	2.7	79.8
B2	100	100	123	2.6	90.7
B3	150	100	102	2.2	81
B4	200	100	112	2.0	78.7
C1	50	150	101	2.8	79.1
C2	100	150	102	2.1	78.3
C3	150	150	105	2.0	77.2
C4	200	150	125	2.1	93
D1	50	200	103	2.3	78.3
D2	100	200	130	1.9	93.8
D3	150	200	107	2.0	75.3
D4	200	200	103	2.0	85.8
E1	140	160	107	2.4	81
E2	160	160	102	2.4	78.7
E3	180	160	98	1.9	84
A4*	200	50	125	2.1	90.7
B1*	50	100	103	2.6	75.7

## 4.8 PL maps

Figure 4.10 shows the comparison of PL spectra of some of the interested spots obtained from altered sample compared with as grown sample which was not treated by UV-laser irradiation and RTA treatment. It can be seen that the differential shift between the only RTA sample and the disordered sample that was processed with the combination of the UV-laser irradiation and RTA is over 100 nm. It can also be seen that not only the peaks have been shifted well over 100 nm relative to the sample which is not irradiated, but the intensity of the under observation spots have also increased significantly. The peaks remain narrow and the full width at half maximum (FWHM) also becomes narrow.

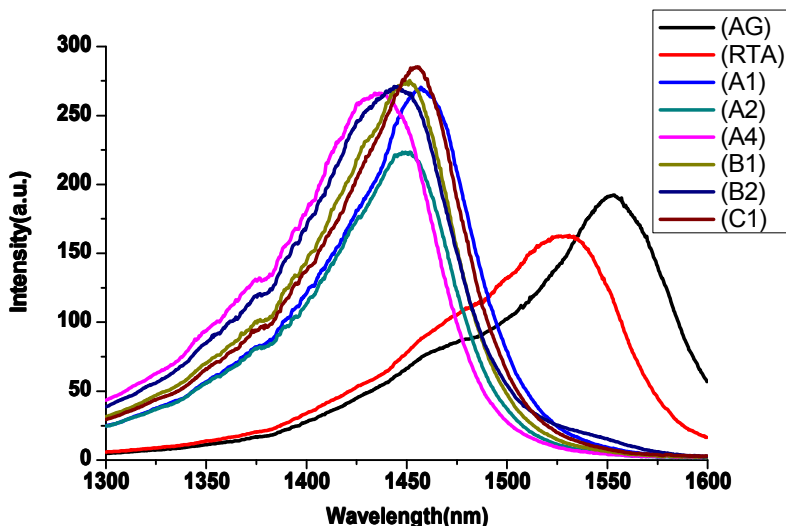


**Fig. 4.10 Comparison of photoluminescence spectra for InGaAsP/InP samples undergone through different treatments of UV-irradiation plus RTA (QWI) and RTA-only at temperature 750°C.**

## 4.9 UV-Laser of Device Fabrication

A larger sample of the InGaAsP/InP laser structure was prepared using UV-QWI procedure to see the versatility of the QWI technique. Since the irradiation window of the set-up was only about  $600 \times 500 \mu\text{m}^2$  with lower intensity at the edges, the QWI region was obtained by using a step-and-repeat process, with step sizes of  $300\mu\text{m}$  and  $250\mu\text{m}$  in the X and Y directions, smaller than the window size to improve the

uniformity. After being exposed to the laser, the sample was annealed in a nitrogen atmosphere using a RTA furnace operating at 750°C for 120s. Figure 4.11a shows wavelength map of the UV-laser irradiated sample while Figure 4.11b shows the measured PL at a point. It is clear that the UV-QWI region has been shifted well over 140 nm while no surface damage was observed.

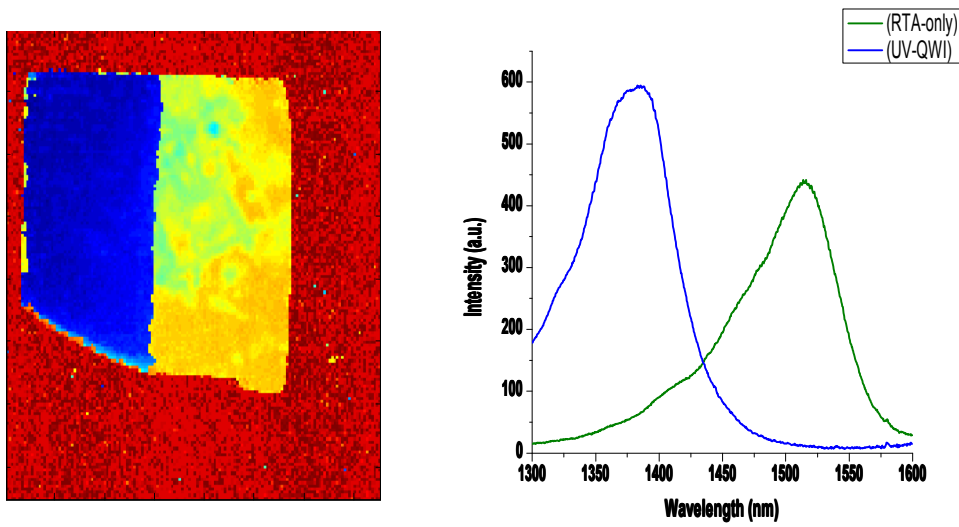


**Fig. 4.11 Room temperature PL wavelength map of a KrF laser processed InGaAsP/InP MQW sample after rapid thermal annealed at 750 °C for 120 s.**

The following section presents our preliminary results on the use of UV irradiation for the fabrication of waveguide and laser device with selective regions of the QWI material.

## 4.10 Low loss Passive Waveguide

In order to investigate the implication of the UV-laser QWI technique for photonic devices, ridge passive waveguides were fabricated. The following section explains the procedures of designing, fabricating and then characterizing of the waveguides.

### 4.10.1 Waveguide Structure

The effective height of the designed ridge waveguide is 1.5 $\mu$ m, and the width is around 3 $\mu$ m. The waveguides are formed using standard wet-etch technique. The Rsoft software was used to design and simulate the passive waveguides.

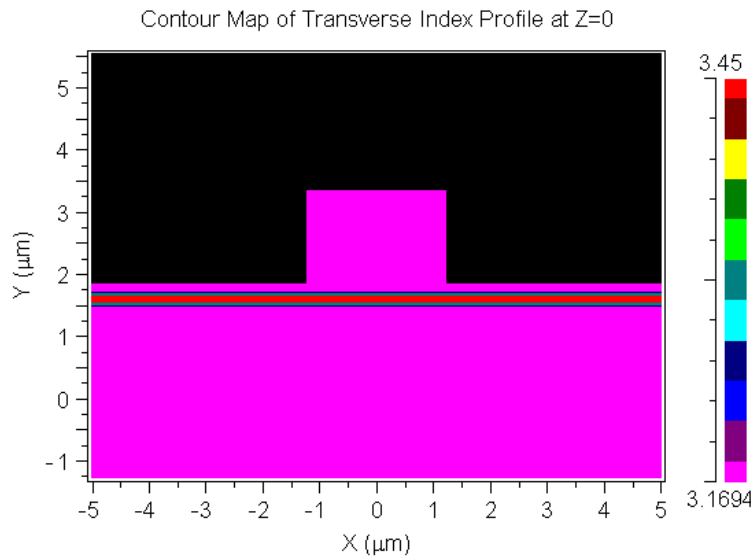


**Fig. 4.12 Cross-sectional view of the waveguide layer structure**

Figure 4.12 shows a cross-sectional view of the waveguide, in which the vertical axis is the deposition direction of the quantum well sample. The horizontal axis is the direction of the width of the waveguide. As can be seen from the Figure 4.12, the active layer is 120nm thick, which is sandwiched by two 60nm gradient refractive index layers. On the top, there is InP ridge waveguide.

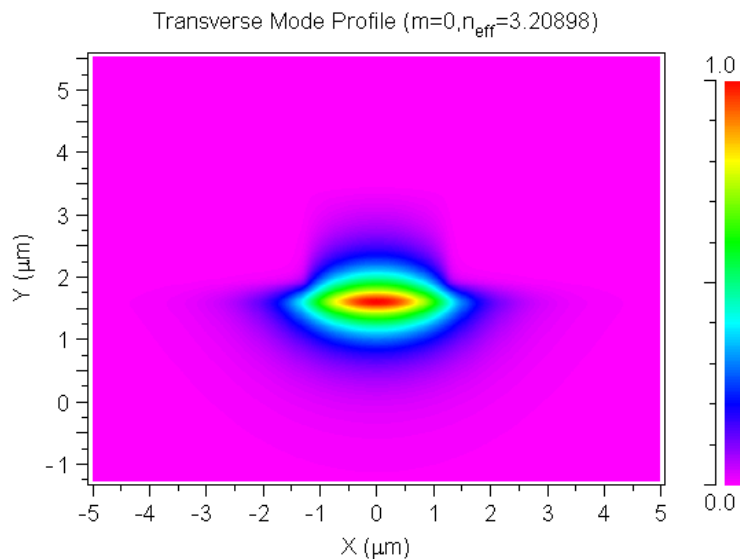


**Fig. 4.13 Optical mode of the waveguide calculated using Rsoft BPM mode**

Figure 4.13 shows the waveguide mode simulated using RSOFT BPM module. It means this waveguide design theoretically ensures single-mode transmission prohibiting high-order modes.

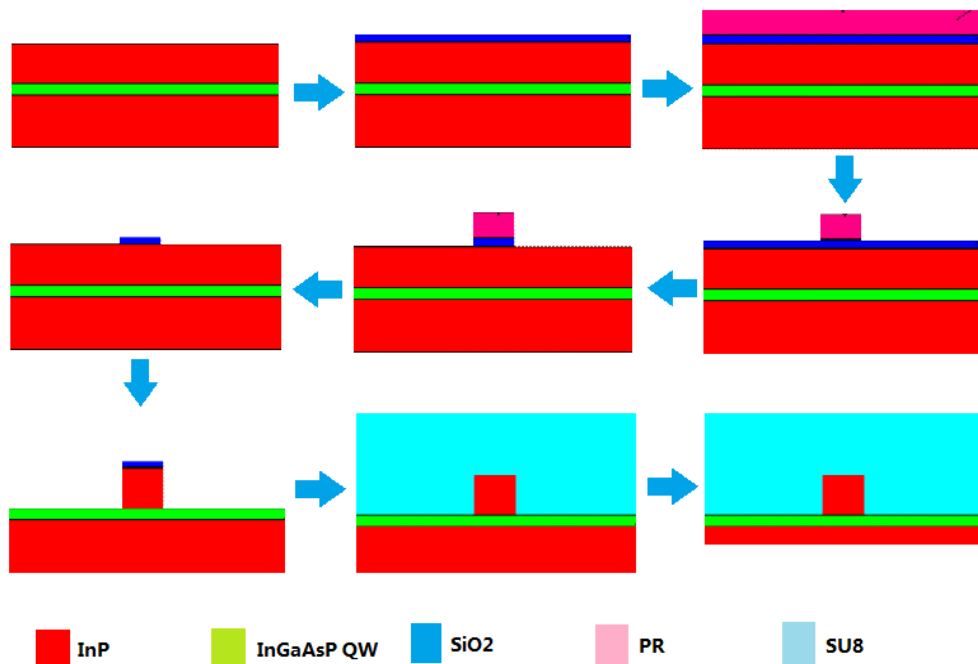
#### 4.10.2 Fabrication Steps

Table 4.3 presents the various steps of waveguide fabrication procedure and Figure 4.14 represents the graphical view of the fabrication steps.

**Table 4.3 Fabrication procedure of the passive waveguide**

**Process:**

- 1) Remove sacrificial layer using  $\text{HCl:H}_2\text{O}=3:1$  for 15s
- 2) deposit  $\text{SiO}_2$  using PECVD for 4min
- 3) Photolithography to define the waveguide pattern
- 4) Etch  $\text{SiO}_2$  using STS-ICP for 3min30s
- 5) remove AZ5214 using STS-ICP for 5min, and then using develop for 30min
- 6) Etch InP waveguide using Oxford-ICP for 1min40s, and then using  $\text{HCl:H}_2\text{O}=3:1$  for 3s
- 7) Remove  $\text{SiO}_2$  using  $\text{NH}_4\text{OH:HF}=6:1$  for 5min
- 8) Planarization using SU8 to protect the waveguides
- 9) Thickness reduction to 120um



**Fig. 4.14 Fabrication steps of passive waveguide**

### 4.10.3 Characterization and Testing Result

There are many methods to measure the loss of waveguide, which includes end-fire method, prism coupling method, scattered light collection method and FP cavity resonance method. In this thesis, we will use FP cavity resonance method, which is one of the commonest waveguide transmission loss test method. One of the benefits of this method is that it has nothing to do with the coupling loss between waveguide and optical fiber. Especially when the dissociation surface is very smooth, the result is accurate and suitable for loss waveguides test.

#### 4.10.3.1 FP Cavity Resonance Method Principle

Figure 4.15 shows the basic principle of FP cavity resonance method. When the light passes through the waveguide, the two waveguide cross-sections form the FP cavity. Then the transmission loss of the waveguide is calculated according to the contrast of the output light and input light.

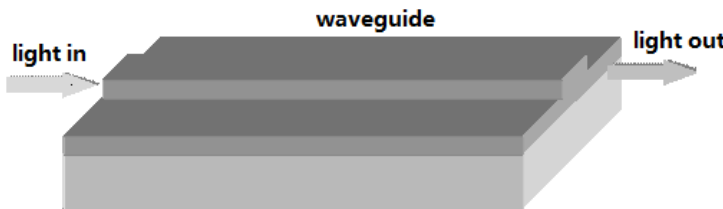


**Fig. 4.15 Waveguide loss schematic diagram of FP cavity resonance measurement**

The spectra out of this FP cavity represents as follows:

$$I_t(\lambda) = I_i \frac{T_1 T_2 \exp(-\alpha l)}{1 - 2\sqrt{R_1 R_2} \exp(-\alpha l) \cos(2n_{eff} k_0 l) + R_1 R_2 \exp(-2\alpha l)}$$

Where T1 and T2 are the two faces of the cavities respectively, and R1 and R2 are the reflectance of the two faces of the cavities respectively. l is the length of the waveguide,  $\alpha$  is the loss coefficient,  $n_{eff}$  is the effective refractive index. Thus the contrast can be expressed as:

$$K = \frac{I_t(\lambda)_{max} - I_t(\lambda)_{min}}{I_t(\lambda)_{max} + I_t(\lambda)_{min}} = \frac{2\sqrt{R_1 R_2} \exp(-2\alpha l)}{1 + R_1 R_2 \exp(-4\alpha l)}$$

According to the measured contrast,  $K_m$  can be obtained as

$$\sqrt{R_1 R_2} \exp(-\alpha l) = \frac{1}{K_m} (1 - \sqrt{1 - K_m^2})$$

The length  $l$  with the waveguide loss  $L=10\log[\exp(-\alpha l)](\text{db})$  can be expressed as

$$L = -4.34\alpha l = 10 \lg \left[ \frac{1}{\sqrt{R_1 R_2}} \frac{1}{K_m} (1 - \sqrt{1 - K_m^2}) \right]$$

The unit length of the waveguide loss is:

$$\frac{L}{l} = -4.34\alpha$$

As the rare reflectance face is very important for the contrast of the spectrum, we need to lay higher requirements on the sample dissociation. In practice, as the resolution of the spectrum analyzer used in the experiments is 0.01nm, and the test requires at least one free spectral range of 10 sampling points, i.e.  $\Delta\lambda_{FSR} > 0.1\text{nm}$ , the free spectral range can be calculated as follows:

$$\Delta\lambda_{FSR} = \frac{\lambda^2}{2n_{eff}l}$$

For our waveguide structure, in which the mode refractive index is 3.215, we obtain:

$$l \leq \frac{\lambda^2}{2n_{eff}\Delta\lambda_{FSR}} = 0.3736\text{cm}$$

Therefore, the measured waveguide should be relatively short.

#### 4.10.4 Measurement Setup

In order to investigate advantage of the UV-laser QWI technique for photonic device fabrication, first we fabricated, 3μm-wide and 500 μm-long ridge waveguides with standard wet-etch technique. Waveguides were fabricated after removing the top sacrificial layer and waveguide loss was measured using the Fabry-Perot fringe technique discussed before. Figure 4.17(a) shows the scanning electrical microscopy (SEM) image of the fabricated ridge waveguides. A tunable (1.46 – 1.62μm) laser diode was used as the input light source. The light was coupled into the TE mode of the waveguide through a polarization-preserving lens fiber. The output light was received by a similar fiber, which was coupled into an InGaAs detector built in a spectrum analyzer. When the light scanned the wavelength from 1460 nm to 1620 nm with a step length of 0.01 nm, the output spectra can be obtained. The bandgap blue

shifts from 1545 nm to 1450 nm. Because of the increase of the bandgap after QWI intermixing, the absorption for the light at 1545nm will reduce a lot. This ensures the lower waveguide loss. The optical loss measurement setup is shown in Fig. 4.16

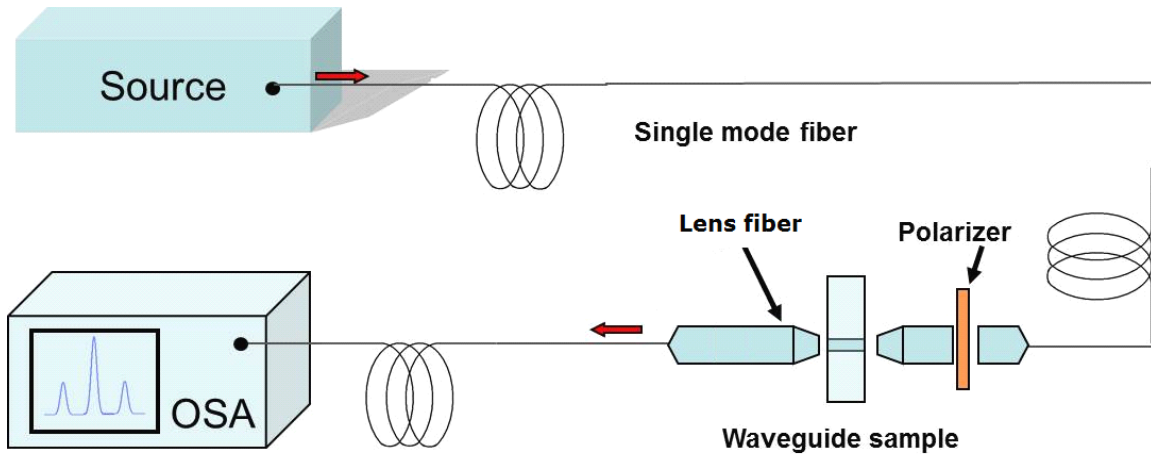


**Fig. 4.16 Schematic of optical loss measurement setup.**

#### 4.10.4.1 Results of the Fabricated Passive Waveguides

Figure 4.17b shows the comparison of optical loss between RTA-only and UV-QWI based waveguides. The intermixed spectra have a blue shift of over 100 nm compared to that of RTA-only. The Fabry-Perot interference fringe is generated due to the multiple reflectances of the two cleaved facets, which is believed to be related to the absorption constant of the waveguide. We can therefore derive the loss coefficient of waveguide via these spectra over the measurement wavelength range. At the absorption edge of the RTA-only waveguide ( $\lambda = 1525$  nm), the loss coefficient of the as-grown waveguide is measured to be 110dB/cm, while that of the intermixed waveguide is reduced to only 20dB/cm. This is a significant reduction of the loss coefficient considering over 100 nm blue shift. By comparing two results, we can find that after intermixing, the loss of the waveguide at the transparent wavelength gets lower. It is possibly due to the partial removal of the defects which exists in the quantum well region of the as-grown sample. The result also means that the UV excimer induced quantum well intermixing process does not induce any extra loss to the quantum well sample.

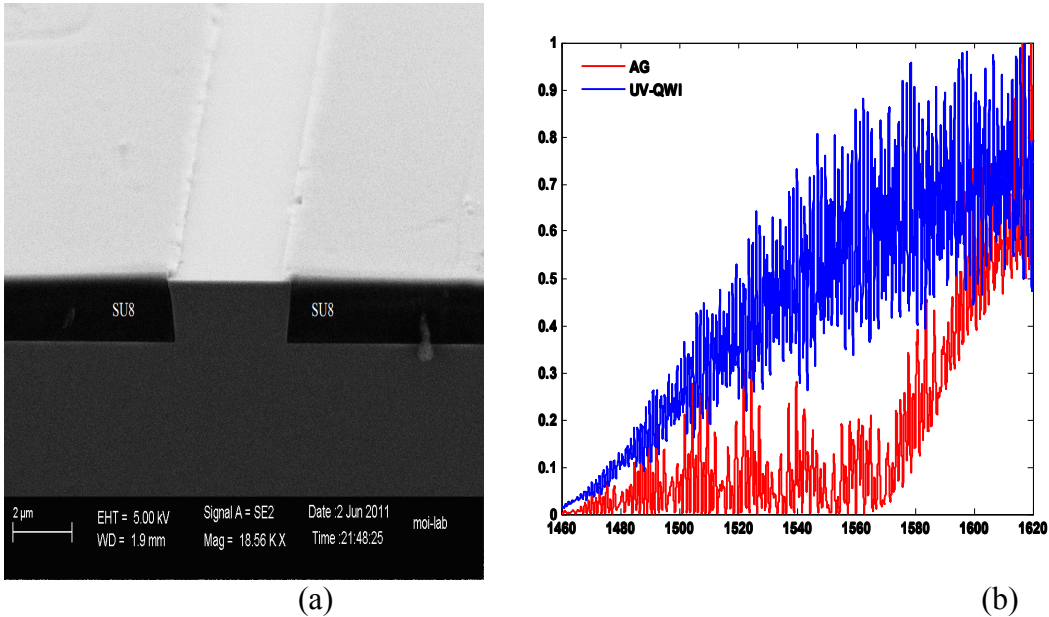


**Fig. 4.17 Transmitted intensity of the passive waveguide before and after UV excimer induced intermixing**

Horizontal axis in Figure 4.17b is the wavelength we scanned, while vertical axis is the output light intensity in linear units. Obviously, after intermixing, the spectrum achieved about 110nm blueshift, which is a quite large blueshift for photonic integration. According to the above Figure, the contrast at 1540 nm for the intermixed sample is:

$$K = \frac{I_1(\lambda)_{\max} - I_t(\lambda)_{\min}}{I_1(\lambda)_{\max} + I_t(\lambda)_{\min}} = \frac{0.810 - 0.333}{0.810 + 0.333} = 0.4173$$

The total loss in the waveguides is:

$$\begin{aligned} L &= -4.34\alpha/l \\ &= 10\lg\left[\frac{1}{\sqrt{R_1 R_2}} \frac{1}{K_m} (1 - \sqrt{1 - k_m^2})\right] \\ &= 10\lg\left[\frac{1}{0.275} \frac{1}{0.4173} (1 - \sqrt{1 - 0.4173^2})\right] \\ &= -1.0143 \text{db} \end{aligned}$$

The unit loss can be finally calculated to be

$$\frac{L}{l} = -4.34\alpha = \frac{-1.0143 \text{db}}{500 \mu\text{m}} = -20.2 \text{db/cm}$$

## 4.11 Fabry-Perot Laser

Fabry-Perot (FP) laser diodes were fabricated on a similar piece of InGaAsP/InP wafer with one half of the piece undergone the UV-QWI process and the other half undergone RTA-only for comparison. The QWI region was prepared with same parameters of UV-laser and RTA as before. The length of the fabricated lasers is 500 $\mu$ m and the width is 3 $\mu$ m. Figure 4.20(a) shows the SEM image of the fabricated FP-laser diodes.

### 4.11.1 Fabrication Steps

The detailed fabrication steps are shown in Table 4.4 while Figure 4.18 graphically represents the fabrication steps.

**Table 4.4 Fabrication procedure of the FP laser**

**Process:**

- 1) Remove sacrificial layer using HCl:H<sub>2</sub>O=3:1 for 15s
- 2) Deposit SiO<sub>2</sub> using PECVD for 4min
- 3) Photolithography to define the waveguide pattern
- 4) Etch SiO<sub>2</sub> using STS-ICP for 3min30s
- 5) remove AZ5214 using STS-ICP for 5min, and then using develop for 30min
- 6) Etch InP waveguide using Oxford-ICP for 1min40s, and then using HCl:H<sub>2</sub>O=3:1 for 3s
- 7) Remove SiO<sub>2</sub> using NH<sub>4</sub>OH:HF=6:1 for 5min
- 8) Planarization using SU8 to make electrodes
- 9) Photolithography to define the electrode pattern
- 10) Sputtering electrode using Ti/Pt/Au
- 11) Liftoff using Acetone for 5min
- 12) Thickness reduction to 120 $\mu$ m
- 13) Sputtering backside electrode using Ti/Pt/Au
- 14) RTA at 400°C for 2min

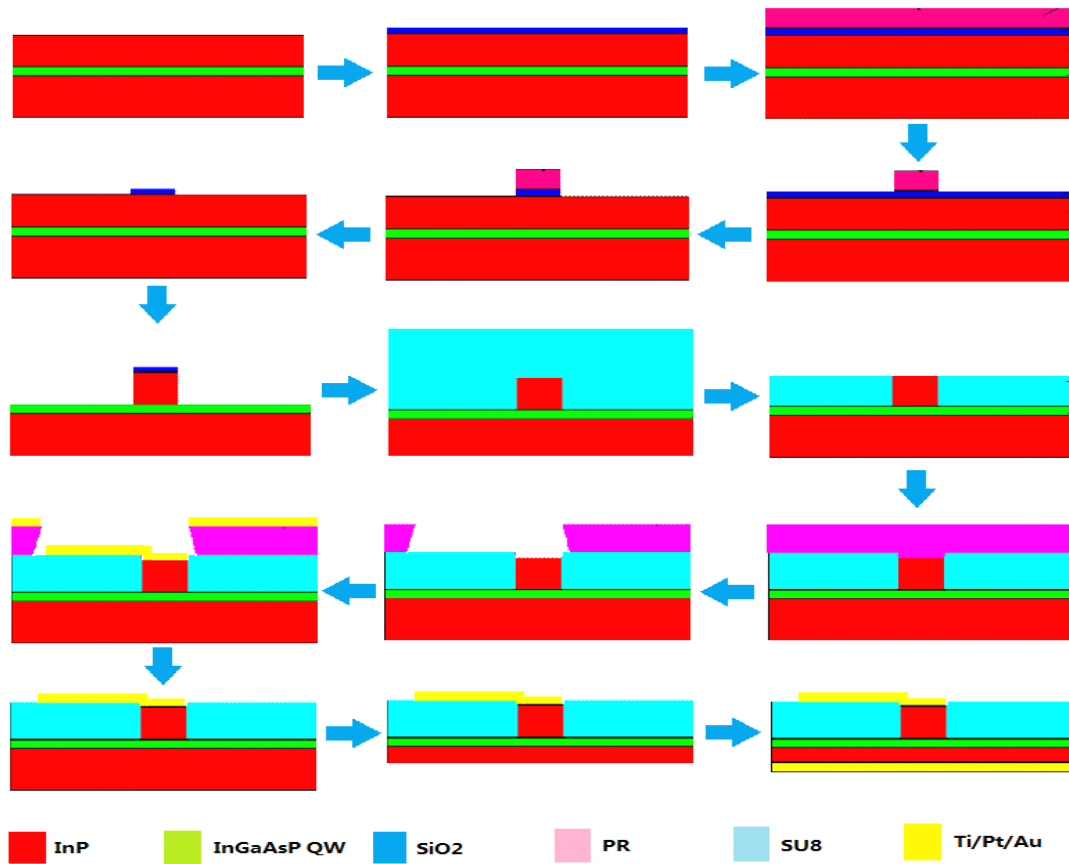
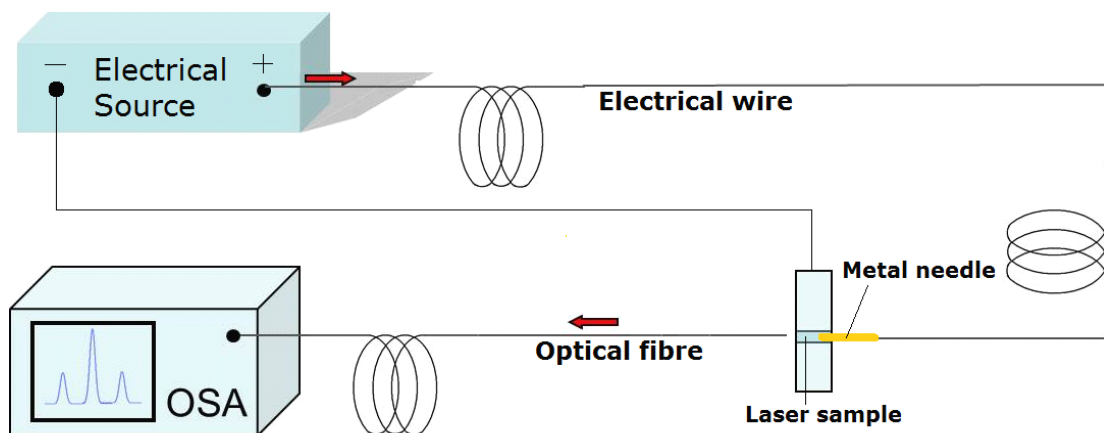


Fig. 4.18 fabrication steps of FP laser diodes

#### 4.11.2 Measurement Setup

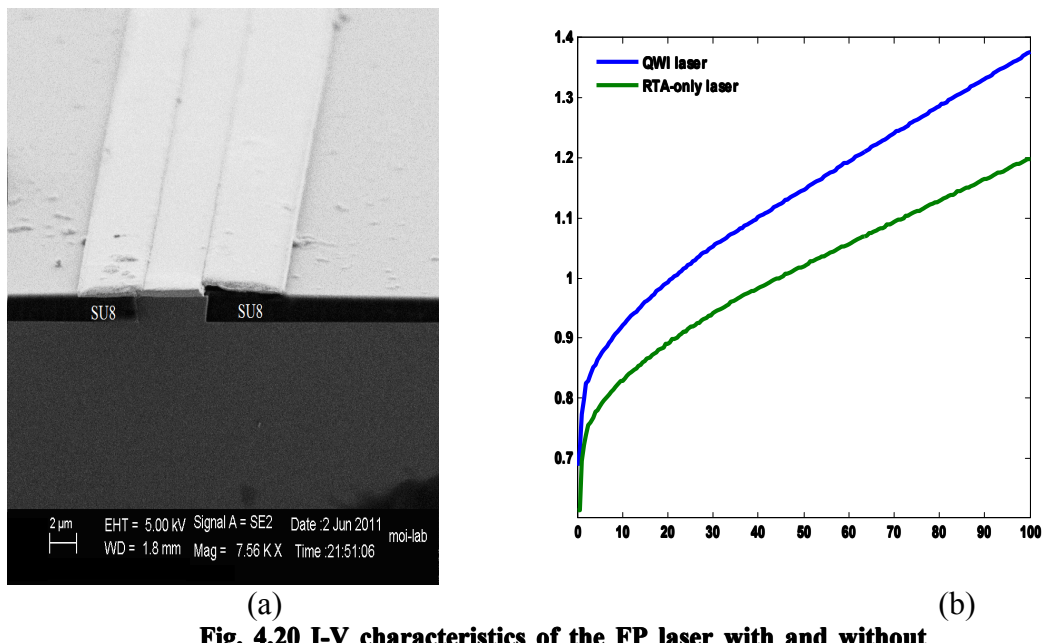
The measurement setup is shown in Fig. 4.19. The light was first focused by an objective on the facet of the sample and the output signal collected by another objective that was coupled into fibre for measurement by OSA. The resolution of the OSA is 50 pm. A polarizer is employed to control the polarization state for TE mode or TM mode measurements.



**Fig. 4.79 Schematic of optical loss measurement setup.**

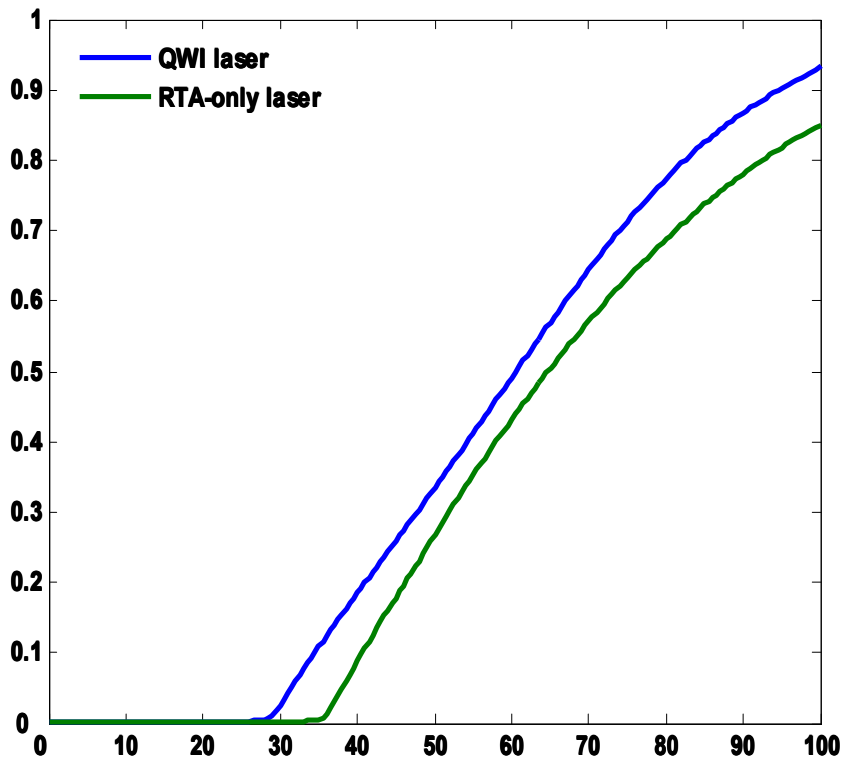
### 4.11.3 Characterisation

Fig. 4.20(b) shows the voltage vs the injected current of the UV-QWI based laser and RTA-only laser. Both the curves seem to be normal I-V laser curves. The turn-on voltage of the UV-QWI laser is measured to be 0.82 volts while that of the RTA-only laser is about 0.75 volts. The large turn-on voltage of the QWI laser is consistent with its larger bandgap as compared to RTA-only laser. The bandgap energy ratio of UV-QWI laser and the RTA-only laser is 1.09 which is about the same as the open voltage ratio of the two lasers.



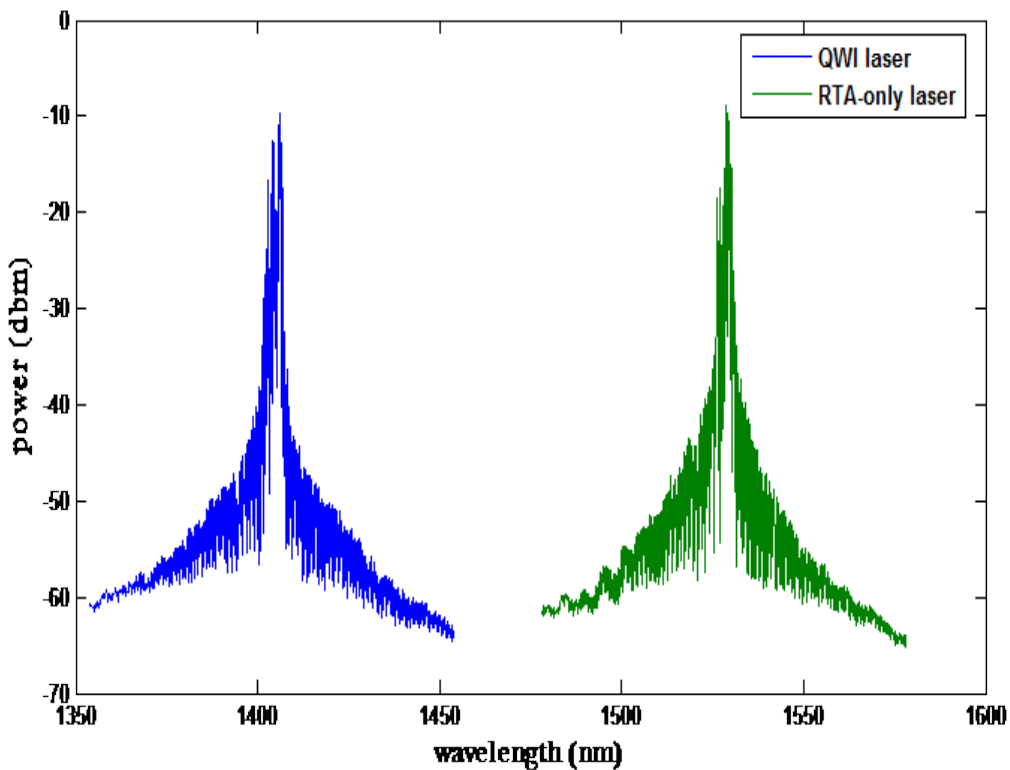
**Fig. 4.20 I-V characteristics of the FP laser with and without UV-QWI**

Figure 4.21 shows the L-I characteristics of the FP lasers from the UV-QWI region and from the RTA-only region. The UV-QWI processed laser has threshold current of 29 mA which is lower than that of the RTA-only laser at 36mA. This shows that after UV-QWI the loss of the laser cavity decreases which is consistent with the results of the PL intensities.



**Fig. 4.21 L-I characteristics of the FP laser with and without UV-QWI**

Figure 4.22 shows the emission spectra of the UV-QWI laser and the RTA-only laser. The emission peak of the QWI laser has been blue shifted from 1535nm to 1405nm, with a net blue shift of 130 nm, while the profile of the laser spectrum remains essentially the same. This further confirms that under appropriate conditions this QWI technique does not affect the lasing property of the material while achieving a large blue shift.



**Fig. 4.22 Emission spectrum of the UV-QWI laser and the RTA-only laser**

## 4.12 Summary

In this chapter we investigate and demonstrate experimentally the UV-laser QWI technique. We investigate first time the bandgap engineering of compressively strained InGaAsP/InP QW laser microstructures by using simple excimer laser irradiation followed by rapid thermal annealing. UV-laser controlled QWI uses UV photons to induce point defects or to alter near surface region chemistry of the QW material. It is achievable to limit the macroscopic modifications to a top sacrificial layer which can be removed after RTA procedure preventing the residual defects on devices produced on the intermixed regions.

We show that the photoluminescence (PL) intensity can be enhanced with reduced linewidth under certain UV irradiation conditions, possibly due to the change of strain distribution in the QW that alters the band structure and enhances the Fermi occupation factor.

Because laser wavelength is related to the material absorption and reflection coefficient therefore, it is important to carefully choose the type of excimer laser, irradiation influences, deposited energy and the interaction volume. Since the beam profile of an excimer laser is spatially non-uniform, it is vital to homogenize it with a group of lenses.

In our experiments, we achieved a net blue shift of 142 nm in the investigated QW material. Low loss waveguides and Fabry-Perot laser diodes have also been fabricated and a lower threshold current is measured for the QWI laser as compared to that of RTA-only laser, while the wavelength is blue-shifted by about 130 nm with similar profiles of the emission spectra. The experimental results have demonstrated the potential of the UV laser QWI technique for the fabrication of integrated multi-bandgap photonic devices.

## **5 QWI by Sputtering SiO<sub>2</sub> and Al<sub>2</sub>O<sub>3</sub> Methods Procedures, Experiments and Results**

### **5.1 Introduction**

In order to investigate alternative techniques to achieve controlled QWI, here we study and demonstrate experimentally SiO<sub>2</sub> and Al<sub>2</sub>O<sub>3</sub> based QWI techniques. In the first section, I present the SiO<sub>2</sub> sputtering method and explain how point defects can be created near the surface of InGaAsP/InP laser structure followed by quick RTA treatment that can lead to large blue shifts. This section also presents the characterization techniques used to analyze the impact of SiO<sub>2</sub> sputtering and discuss the results obtained after PL measurements. It also discusses how we can achieve the spatially selective control over the local optical and electrical properties of the multiple quantum well (MQW) material.

The second section presents the argon plasma induced damage during the deposition of sputtered Al<sub>2</sub>O<sub>3</sub> QWI technique. The technique is similar to SiO<sub>2</sub> based QWI, but here I demonstrate controlled blueshift using Al<sub>2</sub>O<sub>3</sub>. As discussed earlier, point defects are created near the surface of quantum well (QW) chip under the argon plasma exposure region, and then these point defects are diffused downwards to the QW active region in the rapid thermal annealing (RTA) process. More interesting results were obtained in this case which means it could also be one of the promising post-growth QWI methods to blueshift the bandgap for PIC.

### **5.2 Sputtering**

Sputtering is a process whereby atoms are ejected from a solid target material due to bombardment of the target by energetic particles. It happens when the kinetic energy of the incoming particles is much greater than conventional thermal energies ( $\gg 1$  eV). This process uses ions of an inert gas to remove atoms from the surface of a crystalline material called target, the atoms then being electrically deposited to form an extremely thin coating on a sample, for example, glass, metal, plastic, or any semiconductor QW surface. It is commonly used for deposition of coating, etching and analytical techniques (Figure 5.1).

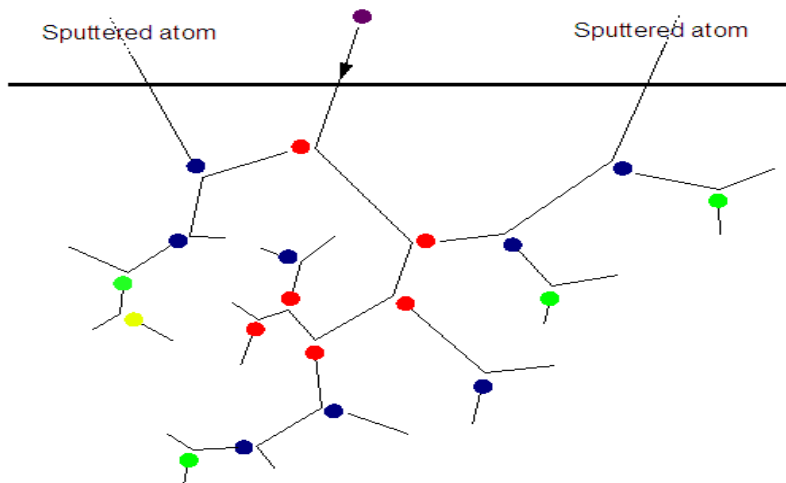


Fig. 5.7 Linear collision cascade sputtering

### 5.2.1 How Sputtering Works

It is a process of depositing thin films by sputtering that involves eroding material from a "target" source onto a "substrate" e.g. a InP wafer. In contrast, Re-sputtering involves re-emission of the deposited material, e.g. SiO<sub>2</sub> during the deposition also by ion bombardment. Sputtered atoms expelled into the gas phase are not in their thermodynamic equilibrium state, and tend to deposit on all surfaces in the vacuum chamber. A substrate (such as a InP wafer etc) placed in the chamber will be coated with a thin film. Sputtering usually uses argon plasma.

The sputtering system used in my experiments to investigate QWI is explained below. Since we are depositing dielectric materials (SiO<sub>2</sub> and Al<sub>2</sub>O<sub>3</sub>) on our laser QW structure to examine the QWI, therefore I only require RF mode because the DC mode can not be used for dielectric material (target).

### 5.2.2 Sputtering PVD 75 System

The PVD 75 System is a versatile, value engineered vacuum system which can be configured to suit a variety of thin film deposition applications. Standard features include a front-loading box chamber, turbo-molecular pump package and an integrated touch-screen control. Source flange options include magnetron sputtering, electron beam evaporation, thermal evaporation and low temperature evaporation furnaces. To ensure product reliability, the system is built using proven process

modules from other standard Kurt J. Lesker Company thin film deposition systems (Figure 5.2).



**Fig. 5.2 PVD 75 System with Integrated control rack and frame**

There are three modes of system operation i.e.,

- Manual – no computer interface or automated processes are provided
- Computer Control – a computer interface is used to operate the system manually
- Recipe Driven Computer Control – a complete computer control software package allowing for process control and creating and running recipes. This is the highest level of automation available.

In my experiment, I used Recipe driven Computer Control mode as it provides more sputtering process control and automation. As mentioned above, only RF mode of the Sputtering PVD system was utilized. Following is the sputtering procedure using RF Source.

### **5.2.3 RF Sputtering Procedure**

1. Pump down the vacuum chamber to high vacuum. The choice of base pressures is the decision of the user and determined by acceptable impurity levels.

2. Select the Vacuum screen. Set high vacuum valve to throttle position (Figure 5.3).
3. Select the Gas screen. Open source gas valve or gas injection valve (depending on system configuration (Figure 5.5).
4. Set MFC1 mode to 4.
5. Set Capman pressure set point to 10 (mTorr).
6. Wait for chamber pressure to stabilize.
7. Select the Deposition screen. Turn on RF power supply output (Figure 5.4).
8. Set power supply ramp rate (typically 10-20 watts per second).
9. Set power supply forward power set point to desired power.
10. Check for the presence of a plasma. If there is no plasma, raise the pressure to 50mTorr of argon in the process chamber. If still no plasma, briefly go to “manual” tuning on the matching network and return to “auto” tuning. If there is still no plasma, briefly open the source shutter. Another method is to fire up another source in the chamber (if available) which will help ignite the plasma.

## Chapter 5 QWI by Sputtering SiO<sub>2</sub> and Al<sub>2</sub>O<sub>3</sub> Methods Procedures, Experiments and Results

---

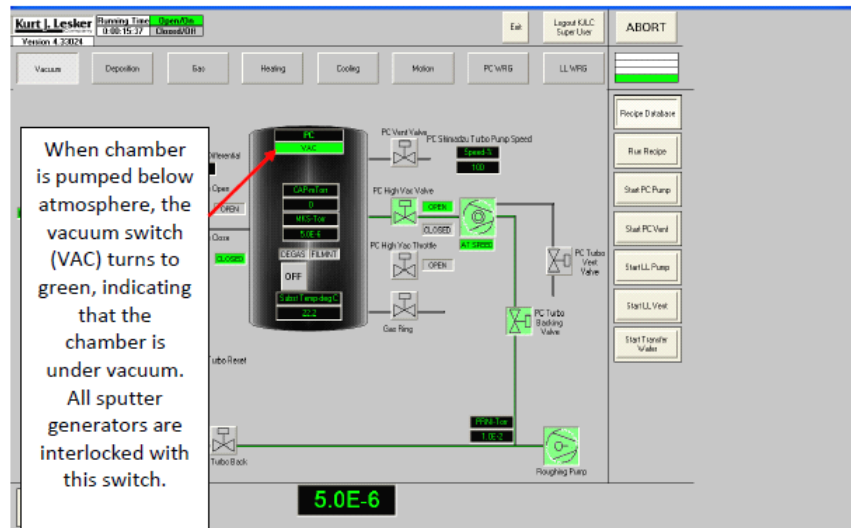


**Fig. 5-3 vacume selection GUI screen**

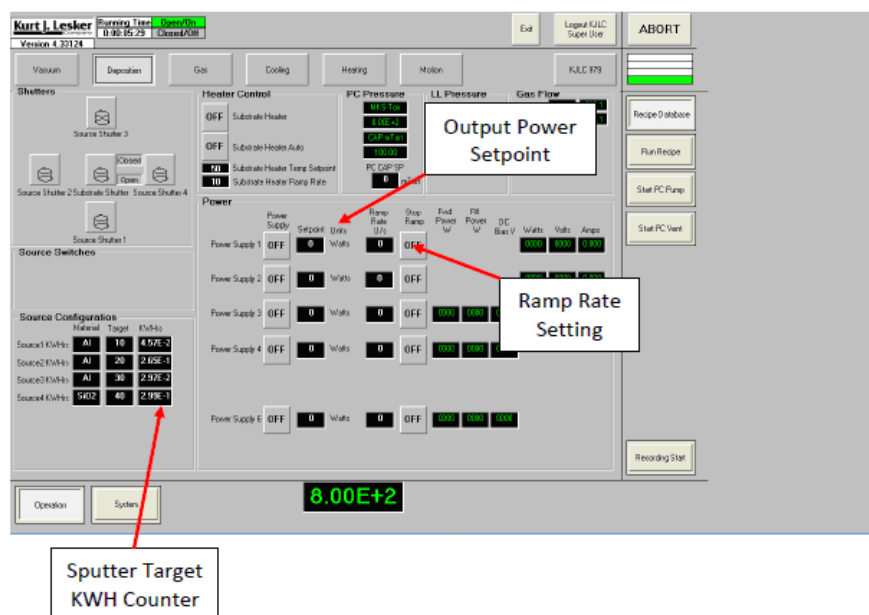


**Fig. 5-4 Deposition select screen to turn on RF power supply**

If the sputtering source is being powered through a cable connected from the matching network, monitor the temperature of this cable and the connectors for excessive heating. Excessive heating can be caused by low impedance at the sputtering source. This results in high current loads through this power transmission cable.

11. When plasma has been established, reduce the gas pressure to the required setting.

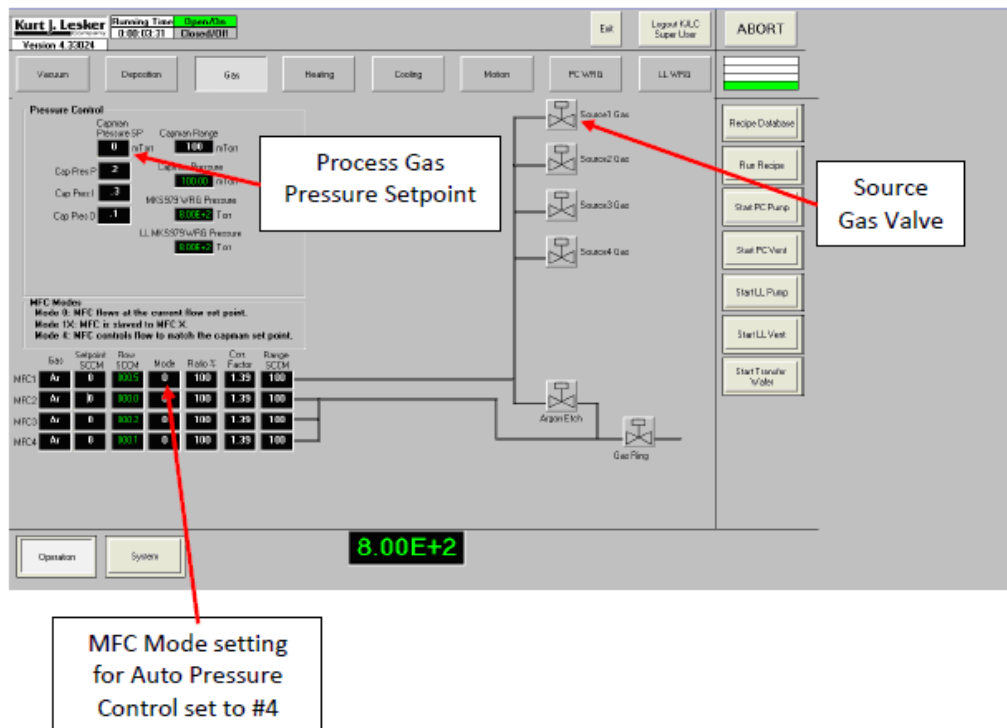


Fig. 5.5 Gas selection screen to turn off/on gas valve.

### 5.2.4 Recipe Controlled Deposition Example

Example of a recipe Controlled RF Sputtered Process:

Table 5.1 Recipe of the RF Sputtered process

Step	Equipment	Equipment Item	Operation
1	Recipe	Set Abort Recipe	Abort Process
2	Recording	Start Recording	Start
3	Recipe	Run Recipe	All Shutters Closed, and pump the chamber.
4	Recipe	Run Recipe	Inject Argon at the rate of 20mT
5	Recipe	Run Recipe	Substrate Rotation at 10rpm
6	Recipe	Run Recipe	Use power source 2 and target 2, and ignite the source under RF mode
7	Recipe	Run Recipe	Set process pressure at 60scm
8	Recipe	Run Recipe	Increase the power of the source to 250W at the speed of 10W/sec
9	Shutter	Substrate Shutter	Open shutter of substrate
10	Shutter	Source Shutter 2	Open shutter of target
11	Recipe	Dwell	3 Seconds
12	Recipe	Run Recipe	Deposite for 4600sec
13	Recipe	Run Recipe	Decrease the power of the source to 0W at the speed of 2W/sec
14	Recipe	Run Recipe	Turn off the power source
15	Recipe	Run Recipe	Stop the Argon

16	Recipe	Run Recipe	Turn off the platen motor rotation
17	Recording	Start Recording	Stop

**Step 1:** Always the first step in a recipe, sets which Abort Recipe should be run in the event a check step that has an AT (Abort on Time) fails.

**Step 2:** Waiting for a desired base pressure before deposition will begin. In this case 5x10<sup>-6</sup> Torr.

**Steps 3-4:** Sets high vacuum valve to throttle position.

**Steps 5-8:** Set-up process gas to a required pressure to strike a plasma.

**Steps 9-11:** Start-up substrate rotation.

**Steps 12-15:** Start running sputter source.

**Steps 16-17:** Reduce gas pressure to required process setting (if necessary).

**Steps 18-23:** Pre-sputter and film deposition.

**Steps 24-27:** Shut down sputter source power supply.

**Steps 28-32:** Stop substrate rotation and turn off process gas.

**Steps 33-34:** Set High vacuum valve throttle off.

Before working on any sputter source ensure that all electrical power is removed from the power supply/generator.

The main differences between RF and DC sputter deposition are

- The gas pressure will normally need to be higher when igniting the plasma
- When checking for the presence of plasma, check for a voltage greater than 50v.

### 5.2.5 Target Changing

- 1) Turn off sputter source power supply. Turn off power supply main distribution panel circuit breaker.
- 2) Switch to the deposition screen, open the source shutter.
- 3) It may sometimes be necessary to remove the shutter blade to make target removal/install easier.
- 4) Loosen the 3 screws supporting the dark space shield and remove the shield (Figure 5.6a,b).

- 5) For a 2" source, loosen the 4 screws of the target hold-down ring (Figure 5.6a,b). For a 3" or 4" source, remove the 4 screws and remove the ring.
- 6) When removing a target of magnetic material, carefully slide the target to one side and pick it up (do not attempt to pry magnetic targets from the cooling well. This may result in permanent damage to the cooling well).
- 7) Place a new target on to the source, ensuring all parts are perfectly clean. If installing a magnetic target, take extra care that fingers or parts of a glove do not get pinched between target and source as the magnets are very powerful.
- 8) Tighten the hold-down ring screws evenly (do not over-tighten screws).
- 9) The dark space shield of the TORUS® source has three machined slots, which ensure .080" dark space on top of the 1/8", 3/16", and 1/4" targets. Loosen the three #8 screws and reposition the dark space shield to the correct slot when changing the target (do not over-tighten the 3 screws).
- 10) After installing a target, check shutter operation and clearance between shutter and sputter source.

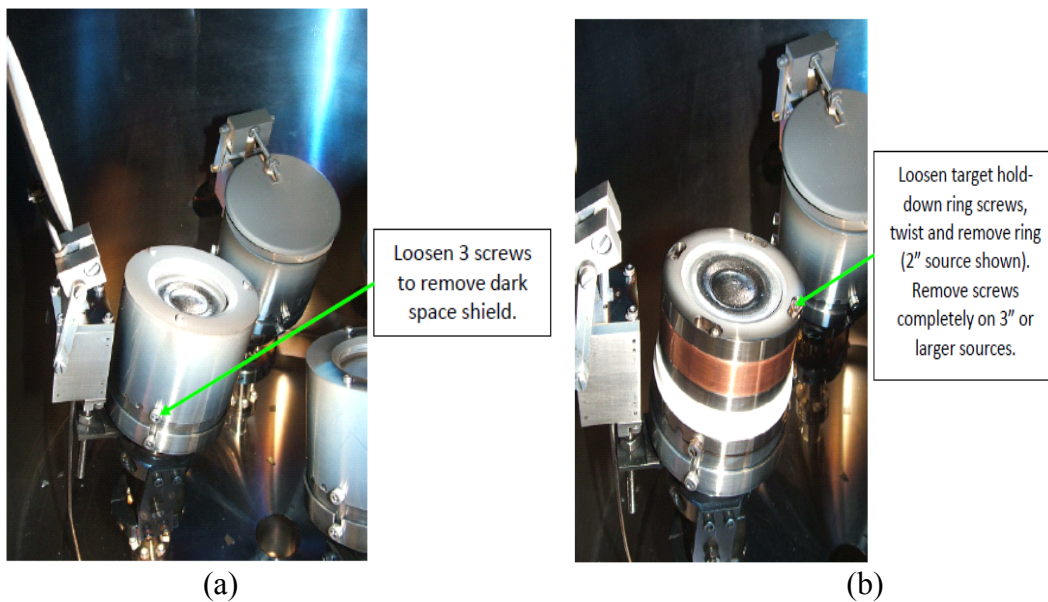


**Fig. 5.6 a: changing the target and b: Mounting the new target**

## 5.2.6 Sputtering Parameters

It is well observed that point defects are produced during the sputtering process [16]. This is because of the bombardment of Ar ions at the QW sample surface, due to acceleration from the positively charged plasma to the earthed substrate electrode.

This accelerating potential provides the ions with adequate energy to split the atomic bonds close to the QW sample surface, producing point defects in the form of free vacancies and thus enhancing the rate of atomic inter diffusion.

### **5.3 Rapid Thermal Annealing Procedure (RTA)**

Following the sputtering, anneal is an essential step performed to diffuse the generated free vacancies into the MQW active region. Certain anneal temperature also called QWI threshold temperature is used to control the amount of energy supplied to the sample. In order to attain spatial selectivity, the anneal temperature is kept low enough so that the quantum wells in the non-QWI sections do not have the required energy to intermix. However, the temperature should be high enough so that the vacancies could move freely. Since the diffusion constant of the vacancies depend on temperature. Therefore, the intermixing efficiency also depends on temperature. It is reasonable to believe that there is a threshold temperature beyond which intermixing happens readily. It is well known that the extent of intermixing is related to the anneal temperature and time. Therefore it is quite possible to control the degree of intermixing.

RTP-300 type annealing furnace is used to achieve thermal inter diffusion process. Rapid thermal annealing (RTA) is widely used as annealing method. In this method, a sample can be uniformly heated to a higher temperature in an inert gas environment within a short period of time. This significantly enhanced the movement of the thermal diffusion of the defects in the semiconductor. This is a critical step for quantum well intermixing.

For this purpose the sample is placed in a quartz chamber, and heating is achieved by high-power mercury lamps. The annealing process is divided into three steps: temperature, heat and cool down. The heating rate of 100-200°C can be achieved in generally less than 10s. Main annealing parameters are temperature and time, the parameters used in our experiments for the annealing are 600-775°C, and the annealing time is 90-120s. The following table 5.2 presents the technical performance of the RTP-300 type rapid thermal equipment.

**Table 5.2 Technical performance of the RTP-300 rapid thermal equipment.**

Temperature range	150 – 1300°C
Temperature rise time	100-200°C / s
Size of the chamber	210x140x14 mm <sup>3</sup>
Controller	Time range 0.1 - 999sec, NO. of steps 8, can be modified separately
Temperature stability	+/- 2°C
Light Source	1.25 kw x 13 Lights1kw x 13 Light
Electric Source	380V electricity , 32A
Water	Tap water, Pressure: 1-3kg / cm <sup>2</sup>
Total size of RTA machine	Total size : 440 x 200 x 520 mm <sup>3</sup>

### 5.3.1 Thermal Stability

As discussed before, intermixing efficiency largely depends on the anneal temperature. The objective of annealing was not only to maximize the differential shift between QWI part and non-QWI parts of the wafer, but also to preserve the surface quality of the QW material.

For the fabrication of photonic devices, it is required that the surface quality of the QW structure be preserved during anneal. Normally, InP based QW structures, extreme thermal annealing leads to decomposition of the semiconductor material resulting in indium accretion on the surface. The indium droplets then dissolve InP leaving macroscopic etch pits [121]. With the onset of thermal decomposition, marked by the evaporation of phosphorous, at around 480°C and increasing sharply at around 510°C [121] , it is clear that the QW material surface should be treated in such a way to stop phosphorous disappearance at the high temperatures.

During a high temperature anneal, it is normal to use a proximity cap as a source of group V overpressure. To prevent the decomposition of the sample of interest, decomposition of the proximity cap creates a sufficient group-V overpressure. This

method confirmed to be insufficient in stopping the surface decomposition. The answer was to encapsulate the under observation sample with two silicon wafers. The employ of the Silicon wafer stabilized the InP base QW surface preventing phosphorous evaporation and the creation of etch pits. The technique proved to be extremely suitable for the QWI task, as insignificant surface damage was observed while using maximum operating temperature of 900°C. Figure 5.7 shows results of RTA-only treatment at temperatures ranging from 800°C-900°C. The PL intensity goes down noticeably but no surface damage was observed as sample was encapsulated with two silicon wafers.

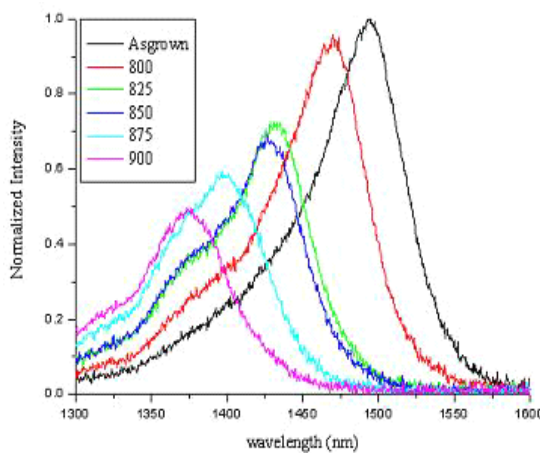


**Fig. 5.7 Photoluminescence (PL) spectra obtained for MQW As-Grown (AG) sample, MQW damage sample rapid thermal annealed (RTA) at 800°C-900°C.**

## 5.4 Photoluminescence (PL) Platform

Schematic diagram of the PL measurement system used is shown in Figure 5.8. The PL measurement system consists of a continuous laser light source Nd:YAG (yttrium aluminum garnet) ( $\lambda = 1064$  nm), maximum output power of 1mw, a directional optical coupler, fiber-optic light path, electric adjustable loading stage, photo detector array and spectrum analyzer. The photoluminescence measurements can be made by using a Nd:YAG laser as an excitation source along with a photo detector array built in a spectrum analyzer. The under observation sample is placed on a computer-controlled x-y stage, which can be moved in 17.5 $\mu$ m steps. With the computer software collecting data as a function of the x-y position, a two dimensional map for the peak wavelength and intensity can be measured.

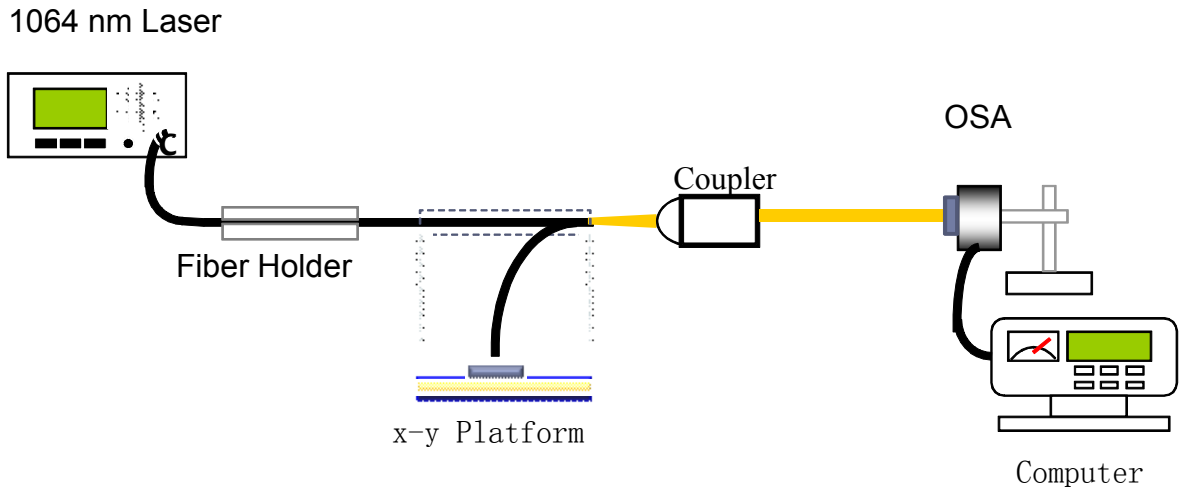


**Fig. 5.8 Schematic of the photoluminescence measurement setup.**

## 5.5 InGaAsP/InP Heterostructure

The investigated sample of InGaAsP/InP laser structure was same as described in the last chapter therefore here I simply concentrate on the experimental set up and analyze the result obtained before and after sputtering and RTA treatments.

### 5.5.1 Photoluminescence Map of the Wafer

The under observation QW laser structure discussed earlier has PL peak wavelength at  $1545 \pm 5$  nm. Figure 5.9 shows the PL map of this sample measured by the PL platform in our lab. The x and y represents the horizontal and vertical axis respectively. The right side bar shows the PL peak wavelength. We can see from the figure that the sample has almost uniform PL intensity and the central wavelength is measured to be 1550nm and the wavelength at the edge of the wafer is about 1540nm.

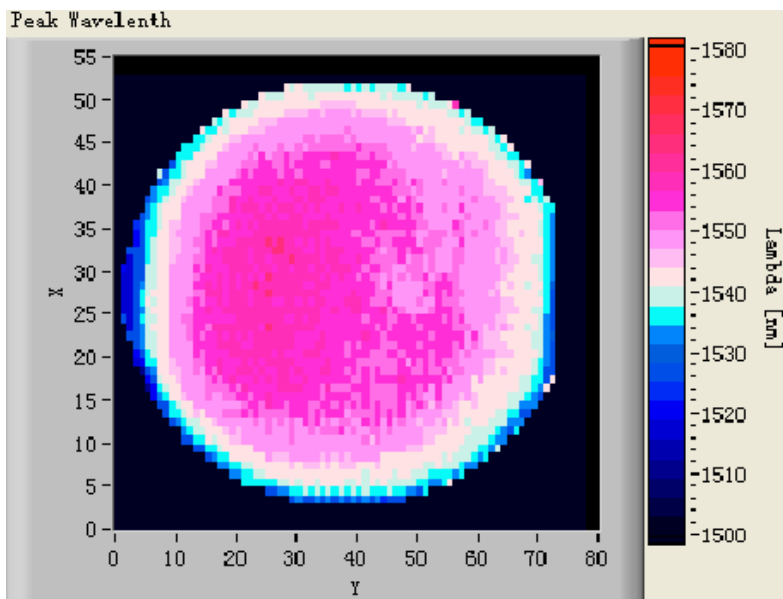


**Figure 5.9 PL map of the 3" InP QW wafer**

## 5.6 Etch Rate Analysis

It is very important to etch each layer of the sample separately before PL measurements without affecting the underneath layers. To etch each layer, the acids and the concentration level of the acid varied along with amount of time. Different acid solutions had to be mixed and prepared. After being etched, each sample was held in de-ionized water for a few seconds. This is crucial because if the sample is not rinsed off, it will continue etching even if the sample is removed from the acid. The following table shows the etch rate.

**Table 5.3 Etch rate of top layers of InGaAsP/InP laser structure**

Material to be Etched	Wet Etchants	Temperature	Time
SiO <sub>2</sub>	NH <sub>4</sub> OH:HF(6:1)	Room temp.	5min
Sacrificial layer	HCl:H <sub>2</sub> O (3:1)	Room temp.	30sec
Cap layer	H <sub>3</sub> PO <sub>4</sub> :H <sub>2</sub> O <sub>2</sub> :H <sub>2</sub> O (1:1:8)	Room temp.	50sec
Cladding layer	HCl:H <sub>2</sub> O (3:1)	Room temp.	30sec

## 5.7 RTA-only Results

Before investigating QW intermixing, we perform a thermal stability test with the as-grown sample to determine the blueshift induced by the RTA-only process. Figure 5.10 shows the results of photoluminescence (PL) energy shifts obtained for the InGaAsP/InP laser structure after performing RTA-only procedure. The InGaAsP/InP MQW laser samples exhibit band-gap shifts at temperatures as low as 660°C.

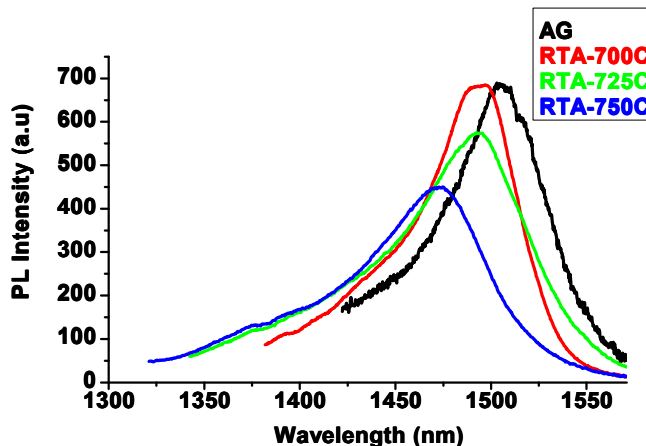


**Fig. 5.10 Room temperature Photoluminescence (PL) spectra obtained for MQW As Grown (AG) sample, MQW damage sample rapid thermal annealed (RTA) at 700°C, 725°C and 750°C.**

The band-gap shifts swiftly with increasing anneal temperature. It goes up to 25 nm at temperatures above 770°C. This shows the thermal stability of multiple quantum well laser structure used. However the PL intensity reduces sharply with increasing temperature above 725°C.

## 5.8 RTA and Sputtering SiO<sub>2</sub>

Figure 5.11 shows PL shifts for InGaAsP/InP samples with sacrificial layer removed (SACR) prior to sputtering. First the sample is capped with about 200nm sputtered SiO<sub>2</sub>. Secondly the cleaved pieces of the under observation sample are annealed at temperatures between 700°C -775°C. The deposited SiO<sub>2</sub> film was then removed using standard wet-etch techniques as discussed earlier. The bandgap shifts induced by the above sputtering procedure were measured using room temperature photoluminescence (PL) measurements. Bandgap shifts are primarily found to occur at temperature of 645°C. Above these threshold temperatures, the bandgap shifts increase quickly over 100 nm at 775 °C. Initially the PL tends to decrease following the deposition, suggesting that the sputtering process does generate damage in the form of point defects, leading to non-radiative recombination and a resultant decrease in PL intensity. The thermal inter-diffusion is believed to be responsible for the change of the confinement profile and strain distribution in the MQW structure.

Furthermore, it is possible that the diffusion of both the dopants (Zn) and surface chemical defects also contributed to the decrease of PL intensity.

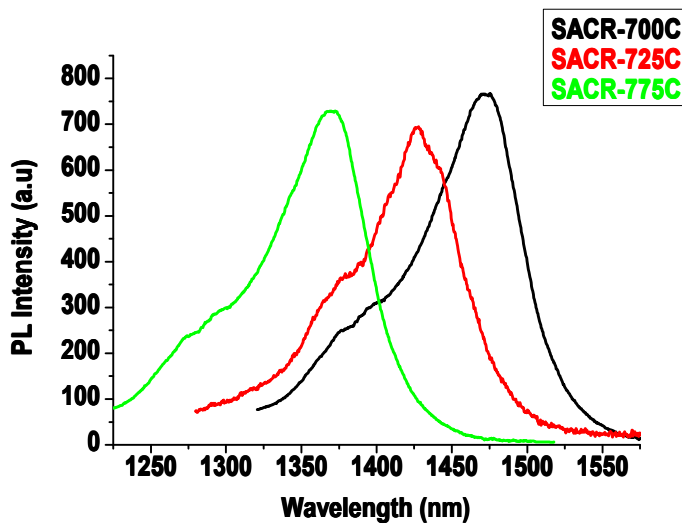


**Fig. 5.11 Room temperature Photoluminescence (PL) spectra obtained for MQW damage samples with sacrificial layer removed (SACR) before sputtering and then rapid thermal annealed at 700°C, 725°C and 775°C.**

The PL intensity then increases near the QWI threshold temperature which in our case is 770°C. The PL is found to undergo a noticeable blue shift due to the initiation of quantum well intermixing process. Even though slight reduction in intensity and line broadening is observed but all samples retain excellent optical quality.

## 5.9 PL Comparison

Figure 5.12 presents comparison of photoluminescence (PL) shifts for InGaAsP/InP samples under gone through different treatments as mentioned before. One can see small element of noise in PL measurements which can be reduced by using liquid Nitrogen. The band-gap shifts are initially found to occur at temperature of 650 °C. The reduction in intensity is found to be about 5% and slight line width broadening is also observed. These PL spectra strongly prove that point defects are generated during the sputtering process and that the thermal diffusion of such defects can lead to an enhancement in quantum well intermixing. This enables large differential bandgap shift to be obtained on a single wafer of InGaAsP/InP laser structure which is necessary for the fabrication of monolithically integrated active

passive devices. Improvement may be obtained with further optimization of process parameters and the use of photo-resist for inhibition of intermixing in selective regions of the sample.

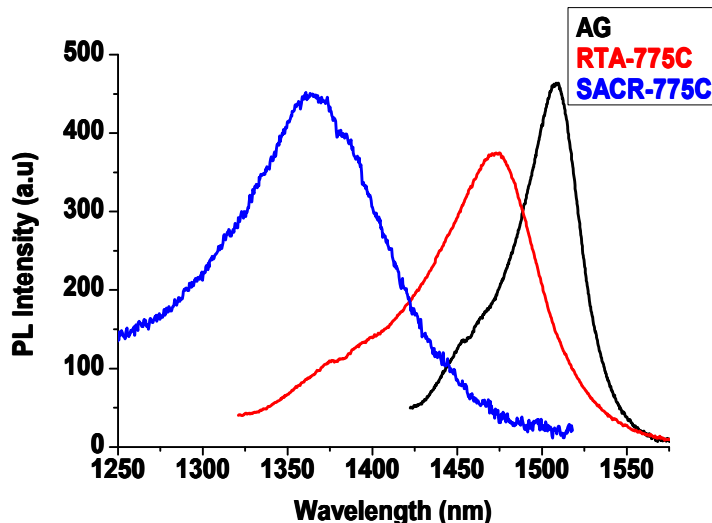


**Fig. 5.12 Comparison of photoluminescence (PL) shifts for InGaAsP samples under gone through different treatments as only RTA, SACR and RTA at temperatures 775°C with as-grown (AG) sample.**

## 5.10 Al<sub>2</sub>O<sub>3</sub> Based QWI

This section presents the recent preliminary experimental results of Al<sub>2</sub>O<sub>3</sub> base QWI. Same InGaAsP/InP standard laser structure was used to investigate this novel technique. Experimental results show that it is another effective post-growth QWI technique that can blue shift the bandgap of InGaAsP/InP QW laser structure. The bandgap of over 100 nm is achievable by sputtering Al<sub>2</sub>O<sub>3</sub> and no surface damage was observed while PL spectra shows good optical quality of the under observation laser sample.

### 5.10.1 Sputtering Procedure

RF mode of the PVD 75 sputtering system is used to carry out Al<sub>2</sub>O<sub>3</sub> sputtering. In my experiments, I used Recipe driven Computer Control mode as it provides more sputtering process control and automation. Since complete RF procedure and the recipe are already discussed earlier, I mainly focused here on the obtained results.

### **5.11.2 Sputtering Parameter**

To achieve large bandgap blueshift of InGaAsP/InP laser structure, a thin layer of about 200 nm sputtered Al<sub>2</sub>O<sub>3</sub> cap was deposited upon the sample structures. The possible damage generated during the sputtering process was investigated before and after sputtering. The deposition was carried out at a RF power of 100 W without DC power using only optimized argon flow rate of 60sccm to generate the sputtering plasma while keeping the chamber temperature of the sputtering machine at 30°C. InGaAsP/InP laser sample was exposed under argon plasma for almost 45 minutes. The wafers were then cleaved and annealed in a nitrogen atmosphere using rapid thermal annealing (RTA). The point defects created during the sputtered Al<sub>2</sub>O<sub>3</sub> process can be ascribed to the bombardment by Ar ions at the sample surface, due to acceleration from the positively charged plasma to the earthed substrate electrode. This accelerating potential provides the ions with sufficient energy to break atomic bonds close to the sample surface, creating point defects in the form of vacancies and thereby enhancing the atomic inter diffusion rate.

### **5.10.3 RTA**

After sputtering Al<sub>2</sub>O<sub>3</sub>, the under observation sample of InGaAsP/InP laser structure was annealed at 750°C using RTP300 annealing furnace for 120s. For this purpose the sample was placed in a quartz chamber, and heating is achieved by high-power mercury lamps. The annealing process is divided into three steps: temperature, heat and cool down. The heating rate of 100-200°C can be achieved in generally less than 10s. Main annealing parameters are temperature and time.

### **5.10.4 Etch Rate Analysis**

It is very important to etch each layer of the sample separately without affecting the underneath layers. To etch each layer the acids and the concentration level of the acid varied along with amount of time. Different acid solutions had to be mixed and prepared. After being etched in the acid,, each sample was held in deionized water for a few seconds. This is crucial because if the sample is not rinsed off, it will continue

etching even if the sample is removed from the acid. The following table shows the etch rate.

**Table 5.4 Etch rate of top layers of InGaAsP/InP laser structure**

<b>Material to be Etched</b>	<b>Wet Etchants</b>	<b>Temperature</b>	<b>Time</b>
Al <sub>2</sub> O <sub>3</sub>	Developer	100°C temp.	60min
Sacrificial layer	HCL:H <sub>2</sub> O (3:1)	Room temp.	30sec
Cap layer	H <sub>3</sub> PO <sub>4</sub> :H <sub>2</sub> O <sub>2</sub> :H <sub>2</sub> O (1:1:8)	Room temp.	50sec
Cladding layer	HCL:H <sub>2</sub> O (3:1)	Room temp.	30sec

### 5.10.5 PL Maps

The bandgap shifts induced by the above Al<sub>2</sub>O<sub>3</sub> procedure were measured using room temperature photoluminescence (PL) measurements. The photoluminescence mapper using a Nd:YAG (yttrium aluminum garnet) laser ( $\lambda = 1064$  nm) was used as an excitation source along with a photo detector array built in a spectrum analyzer. The under observation sample was placed on a computer-controlled x-y stage, which was moved in 17.5 $\mu$ m steps. With the computer software collecting data as a function of the x-y position, a two dimensional map for the peak wavelength and intensity was measured. The PL spectral peak corresponds to the QW electron-hole recombination peak, which for the as-grown material is obtained at 1554nm.

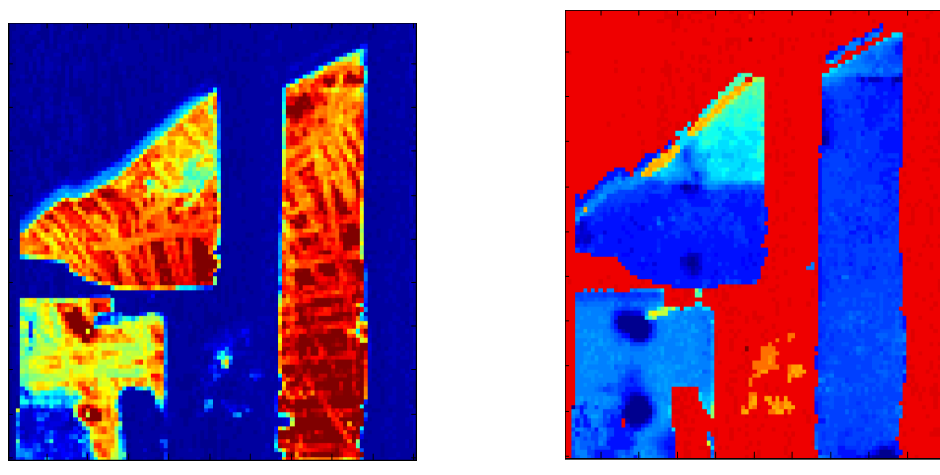


**Fig. 5.13 Room temperature PL wavelength (a) and intensity (b) maps of Al<sub>2</sub>O<sub>3</sub> processed InGaAsP/InP MQW sample after rapid thermal annealed at 750°C for 120s.**

Figure 5.13a,b presents the PL peak wavelength and intensity maps of the under observation sample of InGaAsP/InP laser structure. Four samples marked with A, B, C and D were prepared for analysis as shown in the Figure 5.13a,b. Sample marked with letter C is the as grown sample. Sample marked with letter A is the sample whose sacrificial layer was not removed prior to sputtering Al<sub>2</sub>O<sub>3</sub> and some part of this sample was covered to prevent sputtering for analysis. While samples marked with letter B and D are the samples whose sacrificial layer was removed prior to sputtering 35 nm and 220 nm of Al<sub>2</sub>O<sub>3</sub>.

It can be seen in Figure 5.13b that all samples (A, B, D) exhibit the large blue shifts while covered part of sample A shows clear suppression of wavelength shift. Further, the PL intensity of all samples (A, B, D) is found to be quite good, even higher than that of as grown sample (C) shown in Figure 5.13a. The sample (D) sputtered with about 200 nm of Al<sub>2</sub>O<sub>3</sub> shows higher PL intensity and larger blue shift than that of sample (B) sputtered with only 35 nm of Al<sub>2</sub>O<sub>3</sub>.

## 5.11 Summary

As an alternative two more potential QWI techniques were investigated. In the first section of this chapter, we discussed experimental procedures used to carry out SiO<sub>2</sub> sputtering quantum well intermixing technique. We described the general concept of the sputtering and discussed the influence of certain conditions on the defects generation process. We also illustrated the role and working principles of the sputtering PVD 75 and RTP 300 systems. We also explained the characterization techniques applied to measure the extent of the intermixing and to analyze the sputtering treated surfaces. We presented how photoluminescence is used to measure the blueshift extent and the optical quality of the material after QWI.

The layer structure of InP based QW structures used in these experiments was also described. The under observation InP based QW structure was designed to permit the fabrication of laser diodes at around 1550nm.

The second section presents another novel alternative QWI technique to blue shift the bandgap energy edge of the standard InGaAsP/InP laser structure. We illustrated how sputtering of Al<sub>2</sub>O<sub>3</sub> can generate point defects and how diffusion of these point defect leads to blue shift while no compromise is made with the PL intensity of the QW material. Improvement may be obtained with further optimization of process parameters and the use of photo-resist for inhibition of intermixing in selective regions of the sample.

Experimental results show that these techniques are simple and can be used very successfully to produce laser sources, modulators and transparent passive waveguides, reducing the absorption loss, which is vital and practical for photonic integrated circuit applications.

## 6 Conclusions and Future Work

### 6.1 Conclusion

This research work aimed at the study and improvement of monolithically integrated circuits (PIC) using InGaAsP/InP laser structure. We experimentally presented UV-laser,  $\text{SiO}_2$  and  $\text{Al}_2\text{O}_3$  controlled quantum well intermixing technologies for InP based heterostructures. We for the first time demonstrated the practical applications of UV-laser QWI technique for compressively strained InGaAsP/InP laser structure. We further investigated two alternative QWI techniques based on sputtering  $\text{SiO}_2$  and  $\text{Al}_2\text{O}_3$ . Through this research work, we have illustrated the dynamics and estimated the potential of UV- QWI technology to produce multi-bandgap wafers appropriate to fabricate photonic devices that leads to monolithically integrated photonic circuits in QW structures. At the same time, this work has also highlighted problems which would require to be solved in future work.

For photonic devices to play key role in the dynamic telecommunication market, novel photonics technologies have to show genuine increase in functionalities that can only be achieved by developing a trustworthy and capable integration technology that can afford to reduce the size of photonic integrated circuit and production costs. While considering different integration techniques for photonic devices, QWI technologies are attractive due to numerous advantages. These techniques are simpler to realize and cheaper than ordinary etching and re-growth steps. They generally require equipment well-suited to micro-fabrication methods and can locally altered the bandgap of a QW structure over large energy range with little interface defects among the different bandgap regions. However, these methods are rarely used in the industry. This is largely due to the issue of reliability and reproducibility of many quantum well technologies for accomplishing a desire blueshift. Moreover, the majority of quantum well intermixing technologies depend on the introduction of an additional concentration of point defects into the QW structure. In some cases, these defects can decrease the feature of the intermixed material and influence the optical and electrical characteristics of devices.

In this work, we have developed UV-laser induced QWI to control the energy bandgap of compressively strained InGaAsP/InP MQW laser structures. Using the combination of UV-laser irradiation process and rapid thermal annealing treatment, we show that large bandgap blue shifts can be achieved and the photoluminescence (PL) intensity can be enhanced with reduced linewidth under certain UV irradiation conditions. This is possible due to the change of strain distribution in the QW that alters the band structure and enhances the Fermi occupation factor. By using a thick InP sacrificial layer that is removed after UV irradiation and RTA, little surface damage was observed which might affect the device performance. Depending on the UV laser irradiation fluence and number of pulse, the thermal shift was suppressed over a range of 20 nm. Lateral resolution of about  $1\mu\text{m}$  or better can be achieved with a  $\text{SiO}_2$  dielectric mask that will increase the sharpness between two different bandgap regions. This technique has the potential to become a simple technology to manufacture multi-bandgap quantum well wafers using inexpensive equipment.

In InP-based MQW structures with a thicker InP sacrificial layer, irradiation of UV-laser favors the desorption of near surface atoms and splits atomic bonds which creates more point defects. The additional concentration of point defects helps the UV-laser QWI to shift the bandgap over 142 nm by controlling the laser fluence and number of pulses. A logical model was also established to explain the intermixing enhancement due to the irradiation of UV-laser. For large number pulses, the extent of intermixing saturates and reduces the quality of QW structure.

The UV-laser controlled QWI technology was also applied to fabricate passive waveguides and laser diodes covering wavelengths ranging from 1430 to 1560 nm. The intermixed material achieved by UV-laser QWI confirmed a quality that is equivalent to the reference material. After annealing, the PL spectra from the irradiated sites was much higher than that of untreated sites and the optical losses as well as the threshold current of the intermixed laser diodes was also lower, than the threshold current of the reference laser diodes. The fabricated devices exhibited excellent characteristics in terms of output power, low threshold current and low optical loss.

## 6.2 Perspectives and Future Work

One of major restraint of the UV-laser QWI technology is the control on the laser beam intensity. Unfortunately, this is an inbuilt restraint of the excimer laser. For less number of pulses, the ambiguity of the dumped energy per each pulse is comparatively high and prohibits precise calculation of the induced blueshift. This could be neutralized indirectly by linking the changes in surface properties to the degree of intermixing. Though, it still depends on the excimer laser pulse-to-pulse permanence. This nevertheless would involve a better understanding of the relationship between the modifications of the surface conditions and the degree of intermixing and it would also require standardization of irradiation and annealing processes.

Up till now, we have achieved a significant success in controlling QWI in compressively strained InGaASP/InP quantum well structures using UV-laser. The large blueshift of 142 nm obtained offers an adequate range to fabricate monolithically integrated photonic circuits involving active and passive devices. The low loss transparent passive waveguides would require to be produced in the regions representing highest blueshift. Using accurate plasma etching technology to characterize the waveguides, we can simply visualize a photonic chip containing multiple lasers leasing on various channels and the multiplexing optics. The degree of integration realized would allow large production of such high resolution chips for the communication and information industry.

Last but not least, an even simpler alternative Al<sub>2</sub>O<sub>3</sub> based QWI technique is proposed and demonstrated experimentally for this purpose. Large blueshift of over 110 nm was achieved while the PL intensity of the altered sample also remains high, even higher than that of as-grown sample. The preliminary results are very encouraging and further investigation is required to realize the full potential of this novel technique as this approach could also allow for the formation of multiple quantum well band edges, ideally one specific to each integrated component.

## References

- [1] Peter J. Winzer, "Optical communications Beyond WDM", 2013.
- [2] RBN, "CWDM Technology", Standards, Economics & Applications, 2002.
- [3] Sean Koehl and Mario Paniccia, "The Quest to Siliconize Photonics-Producing photonic devices with standard silicon could revolutionize communications, computing, medicine and more.", Photonics Spectra, 2005, vol.39, no.11, p53-61.
- [4] Gordon E Moore and others, "Cramming more components onto integrated circuits", McGraw-Hill, 1965.
- [5] Sylvain Charbonneau, Emil S Koteles, PJ Poole, JJ He, GC Aers, J Haysom, M Buchanan, Y Feng, A Delage, F Yang and others, "Photonic integrated circuits fabricated using ion implantation", Selected Topics in Quantum Electronics, IEEE Journal of, 1998, vol.4, no.4, p772-793.
- [6] J. Mills, "Photonic integration combats network complexity", 2007.
- [7] Hyundai Park, Alex Fang, er W , Satoshi Kodama and John E Bowers, "Hybrid silicon evanescent laser fabricated with a silicon waveguide and III-V offset quantum well", 2005.
- [8] Mario Paniccia and Justin Rattana, "The 50 Gbps Si photonics link", 2013.
- [9] Alex Fang, er W , Hyundai Park, Richard Jones, Oded Cohen, Mario J Paniccia and John E Bowers, "A continuous-wave hybrid AlGaInAs-silicon evanescent laser", Photonics Technology Letters, IEEE, 2006, vol.18, no.10, p1143-1145.
- [10] Mario Paniccia, Victor Krutul, Richard Jones, Oded Cohen, John Bowers, A Fang and Hyundai Park, "A Hybrid Silicon Laser: Silicon photonics technology for future tera-scale computing", Technology, 2006, p1.
- [11] Elizabeth Bruce, "Tunable lasers", IEEE Spectrum, 2002, vol.39, no.2, p35-39.
- [12] James W Raring and Larry A Coldren, "40-Gb/s widely tunable transceivers", Selected Topics in Quantum Electronics, IEEE Journal of, 2007, vol.13, no.1, p3-14.
- [13] John Marsh, "Intermixing Drives Photonic Integration", Compound Semiconductor, 2001, p63-67.
- [14] Li, E. H., Ed, "Semiconductor Quantum Wells Intermixing. Optoelectronic Properties of Semiconductors and Superlattices", Amsterdam, Netherlands, Gordon and Breach Science Publishers, 2000, p695.
- [15] LL Chang and A Koma, "Interdiffusion between GaAs and AlAs", Applied Physics Letters, 1976, vol.29, no.3, p138-141.

- [16] John H Marsh, "Quantum well intermixing", Semiconductor science and technology, 1993, vol.8, no.6, p1136.
- [17] CJ McLean, JH Marsh, RM De La Rue, AC Bryce, B Garrett and RW Glew, "Layer selective disordering by photoabsorption-induced thermal diffusion in InGaAs/InP based multiquantum well structures", Electronics Letters, 1992, vol.28, no.12, p1117-1119.
- [18] JJ Dubowski, Y Feng, PJ Poole, Margaret Buchanan, S Poirier, J Genest and V Aimez, "Monolithic multiple wavelength ridge waveguide laser array fabricated by Nd: YAG laser-induced quantum well intermixing", Journal of Vacuum Science & Technology A: Vacuum, Surfaces, and Films, 2002, vol.20, no.4, p1426-1429.
- [19] Boon Siew Ooi, Teik Kooi Ong and Oki Gunawan, "Multiple-wavelength integration in InGaAs-InGaAsP structures using pulsed laser irradiation-induced quantum-well intermixing", Quantum Electronics, IEEE Journal of, 2004, vol.40, no.5, p481-490.
- [20] DV Podlesnik, HH Gilgen, AE Willner, RM Osgood Jr and others, "Interaction of deep-ultraviolet laser light with GaAs surfaces in aqueous solutions", JOSA B, 1986, vol.3, no.5, p775-784.
- [21] J Genest, JJ Dubowski, V Aimez, N Pauc, D Drouin and M Post, "UV laser controlled quantum well intermixing in InAlGaAs/GaAs heterostructures", Journal of Physics: Conference Series, IOP Publishing, 2007, vol.59, no.1, p605.
- [22] Mohammad Kaleem, Xin Zhang and Jian-Jun He, "Bandgap Engineering of InGaAsP/InP Laser Structure by Argon Plasma Induced Point Defects", Asia Communications and Photonics Conference, Optical Society of America, 2012.
- [23] Mohammad Kaleem, Xin Zhang, Yuan Zhuang, Jian-Jun He, Neng Liu and Jan J. Dubowski, "UV laser induced selective-area bandgap engineering for fabrication of InGaAsP/InP laser devices" Journal of Optics and Laser Tech., 2013 (accepted).
- [24] Ben G Streetman and Sanjay Banerjee, "Solid state electronic devices", Prentice Hall New Jersey, 2000.
- [25] CF Yu, MT Schmidt, DV Podlesnik and RM Osgood, "Wavelength dependence of optically induced oxidation of GaAs (100)", Journal of Vacuum Science & Technology B: Microelectronics and Nanometer Structures, 1987, vol.5, no.4, p1087-1091.
- [26] Jaques I Pankove, "Optical processes in semiconductors", Courier Dover Publications, 1971.
- [27] Jouni Ahopelto, Markku Sopanen and Harri Lipsanen, "Tailoring of energy levels in strain-induced quantum dots", Japanese journal of applied physics, 1999, vol.38, p1081.

- [28] John P Loehr, "Physics of strained quantum well lasers", Springer, 1998.
- [29] J. H. Davies, "Elastic fields in optoelectronic devices", Lausanne, 2003.
- [30] Joseph Micallef, E Herbert Li and Bernard L Weiss, "The effects of strain on the confinement profile of disordered InGaAs/GaAs single quantum wells", Superlattices and microstructures, 1993, vol.13, no.1, p125.
- [31] Weng W Chow and Stephan W Koch, "Semiconductor-laser fundamentals", Springer Verlag, 1999.
- [32] Joachim Piprek, "Semiconductor optoelectronic devices: Introduction to physics and simulation", Academic Press, 2003.
- [33] PA Kirkby, PR Selway and LD Westbrook, "Photoelastic waveguides and their effect on stripe-geometry GaAs/Ga<sub>1-x</sub>Al<sub>x</sub>As lasers", Journal of Applied Physics, 1979, vol.50, no.7, p4567-4579.
- [34] MF Pereira Jr, Stephan W Koch, Weng W Chow and others, "Effects of strain and Coulomb interaction on gain and refractive index in quantum-well lasers", JOSA B, 1993, vol.10, no.5, p765-773.
- [35] AA Grinberg, ID IAROSHETSKII, RF MEKHTIEV, SM RYVKIN and VM SALMANOV, "Absorption of laser radiation and damage in semiconductors(Absorption of laser radiation in semiconductors and mechanisms of breakdown in process)", Soviet Physics-Solid State, 1967, vol.9, p1085-1090.
- [36] J. C Miller, and R. F., Eds Haglund, "Laser ablation and desorption. Experimental methods in the physical sciences", San Diego, Academic Press, p647.
- [37] AV Kuanr, SK Bansal and GP Srivastava, "Laser induced damage in GaAs at 1.06 um wavelength: surface effects", Optics & Laser Technology, 1996, vol.28, no.1, p25-34.
- [38] Amit Garg, Avinashi Kapoor and KN Tripathi, "Laser-induced damage studies in GaAs", Optics & Laser Technology, 2003, vol.35, no.1, p21-24.
- [39] JR Meyer, FJ Bartoli and MR Kruer, "Optical heating in semiconductors", Physical Review B, 1980, vol.21, no.4, p1559.
- [40] AV Kuanr, SK Bansal and GP Srivastava, "Laser induced damage in GaAs at 1.06 um wavelength: surface effects", Optics & Laser Technology, 1996, vol.28, no.1, p25-34.
- [41] Amit Garg, Avinashi Kapoor and KN Tripathi, "Laser-induced damage studies in GaAs", Optics & Laser Technology, 2003, vol.35, no.1, p21-24.
- [42] Nick Holonyak Jr, "Impurity-induced layer disordering of quantum-well heterostructures: Discovery and prospects", Selected Topics in Quantum Electronics,

IEEE Journal of, 1998, vol.4, no.4, p584-594.

- [43] Shu Yuan, Chennupati Jagadish, Yong Kim, Yong Chang, Hark Hoe Tan, Richard M Cohen, Mladen Petracic, Lap Van Dao, Mike Gal, Michael CY Chan and others, "Anodic-oxide-induced intermixing in GaAs-AlGaAs quantum-well and quantum-wire structures", Selected Topics in Quantum Electronics, IEEE Journal of, 1998, vol.4, no.4, p629-635.
- [44] Xingquan Liu, Wei Lu, Xiaoshuang Chen, SC Shen, HH Tan, S Yuan, C Jagadish, MB Johnston, LV Dao, M Gal and others, "Wavelength shifting of adjacent quantum wells in V-groove quantum wire structure by selective implantation and annealing", Journal of Applied Physics, 2000, vol.87, no.3, p1566-1568.
- [45] R Leon, Yong Kim, C Jagadish, M Gal, J Zou and DJH Cockayne, "Effects of interdiffusion on the luminescence of InGaAs/GaAs quantum dots", Applied physics letters, 1996, vol.69, no.13, p1888-1890.
- [46] JE Haysom, GC Aers, S Raymond and PJ Poole, "Study of quantum well intermixing caused by grown-in defects", Journal of Applied Physics, 2000, vol.88, no.5, p3090-3092.
- [47] Fabrice Bollet, WP Gillin, M Hopkinson and R Gwilliam, "On the diffusion of lattice matched InGaAs/InP microstructures", Journal of applied physics, 2003, vol.93, no.7, p3881-3885.
- [48] O Gunawan, TK Ong, YW Chen, BS Ooi, YL Lam, Y Zhou and YC Chan, "A theoretical analysis of quantum well intermixing using the pulsed laser irradiation technique in InGaAs/InGaAsP laser structure", Surface and Coatings Technology, 2000, vol.130, no.1, p116-121.
- [49] Sadao Adachi, "Material parameters of InGaAsP and related binaries", Journal of Applied Physics, 1982, vol.53, p8775.
- [50] DJ BenDaniel and CB Duke, "Space-charge effects on electron tunneling", Physical Review, 1966, vol.152, no.2, p683.
- [51] WD Laidig, N Holonyak, MD Camras, K Hess, JJ Coleman, PD Dapkus and J Bardeen, "Disorder of an AlAs-GaAs superlattice by impurity diffusion", Applied Physics Letters, 1981, vol.38, no.10, p776-778.
- [52] RM Cohen, "Point defects and diffusion in thin films of GaAs", Materials Science and Engineering: R: Reports, 1997, vol.20, no.4, p167-280.
- [53] James D Plummer, "Silicon VLSI technology: fundamentals, practice, and modeling", Pearson Education India, 2009.
- [54] John Douglas Eshelby, "The force on an elastic singularity", Philosophical Transactions of the Royal Society of London. Series A, Mathematical and Physical Sciences, 1951, vol.244, no.877, p87-112.

- [55] David T Britton and Margit Harting, "The influence of strain on point defect dynamics", Advanced Engineering Materials, 2002, vol.4, no.8, p629-635.
- [56] Kris V Srikrishnan, "Smart-cut process for the production of thin semiconductor material films", Google Patents, 1999.
- [57] LJ Guido, GS Jackson, WE Plano, KC Hsieh, N Holonyak, RD Burnham, JE Epler, RL Thornton and TL Paoli, "Index-guided  $\text{Al}_x\text{Ga}_{1-x}\text{As}$ -GaAs quantum well heterostructure lasers fabricated by vacancy-enhanced impurity-induced layer disordering from an internal  $(\text{Si}_2)_y(\text{GaAs})_{1-y}$  source", Applied physics letters, 1987, vol.50, no.10, p609-611.
- [58] S Mitra and JP Stark, "Role of vacancies and implantation defects in GaAs/AlAs superlattice intermixing", Journal of materials science, 1991, vol.26, no.24, p6650-6654.
- [59] J Beauvais, JH Marsh, AH Kean, AC Bryce and C Button, "Suppression of bandgap shifts in GaAs/AlGaAs quantum wells using strontium fluoride caps", Electronics Letters, 1992, vol.28, no.17, p1670-1672.
- [60] A Saher Helmy, NP Johnson, ML Ke, A Catrina Bryce, J Stewart Aitchison, John H Marsh, Ivair Gontijo, Gerald S Buller, J Davidson and P Dawson, "A study of impurity-free vacancy disordering in GaAs-AlGaAs for improved modeling", Selected Topics in Quantum Electronics, IEEE Journal of, 1998, vol.4, no.4, p661-668.
- [61] JH Teng, JR Dong, SJ Chua, DA Thompson, BJ Robinson, ASW Lee, John Hazell and Irwin Sproule, "Impurity-free intermixing in compressively strained InGaAsP multiple quantum well structures", Materials Science in Semiconductor Processing, 2001, vol.4, no.6, p621-624.
- [62] Vincent Aimez, Jacques Beauvais, J Beerens, Denis Morris, HS Lim and Boon-Siew Ooi, "Low-energy ion-implantation-induced quantum-well intermixing", Selected Topics in Quantum Electronics, IEEE Journal of, 2002, vol.8, no.4, p870-879.
- [63] BS Ooi, CJ Hamilton, K McIlvaney, AC Bryce, RM De La Rue, JH Marsh and JS Roberts, "Quantum-well intermixing in GaAs-AlGaAs structures using pulsed laser irradiation", Photonics Technology Letters, IEEE, 1997, vol.9, no.5, p587-589.
- [64] JW Lee and WD Laidig, "Diffusion and interdiffusion in Zn-disordered AlAs-GaAs superlattices", Journal of Electronic Materials, 1984, vol.13, no.1, p147-165.
- [65] Dennis Glenn Deppe and N Holonyak, "Atom diffusion and impurity-induced layer disordering in quantum well III-V semiconductor heterostructures", Journal of applied physics, 1988, vol.64, no.12, pR93-R113.
- [66] TY Tan, "Point defect thermal equilibria in GaAs", Materials Science and

- Engineering: B, 1991, vol.10, no.3, p227-239.
- [67] R Lai, J Pamulapati, PK Bhattacharya and RJ Baird, "Low-loss, single-mode In<sub>0.53</sub>Ga<sub>0.47</sub>As/In<sub>0.52</sub>Al<sub>0.48</sub>As/InP optical waveguides fabricated by Zn-induced impurity-induced layer disordering", Journal of applied physics, 1991, vol.70, no.9, p5136-5137.
- [68] E Kapon, NG Stoffel, EA Dobisz and R Bhat, "Birefringent channel waveguides defined by impurity-induced superlattice disordering", Applied physics letters, 1988, vol.52, no.5, p351-353.
- [69] L Fu, P Lever, HH Tan, C Jagadish, P Reece and M Gal, "Suppression of interdiffusion in InGaAs/GaAs quantum dots using dielectric layer of titanium dioxide", Applied physics letters, 2003, vol.82, no.16, p2613-2615.
- [70] Paulus L Gareso, Lan Fu, Manuela Buda, Hark H Tan and Chennupati Jagadish, "Suppression of thermal atomic interdiffusion in InGaAs/AlGaAs QW laser structures", Proc. of SPIE Vol, 2004, vol.5277, p357.
- [71] L Fu, J Wong-Leung, PNK Deenapanray, HH Tan, C Jagadish, Bin Gong, RN Lamb, RM Cohen, W Reichert, LV Dao and others, "Suppression of interdiffusion in GaAs/AlGaAs quantum-well structure capped with dielectric films by deposition of gallium oxide", Journal of applied physics, 2002, vol.92, no.7, p3579-3583.
- [72] Boon-Siew Ooi, SG Ayling, AC Bryce and JH Marsh, "Fabrication of multiple wavelength lasers in GaAs-AlGaAs structures using a one-step spatially controlled quantum-well intermixing technique", Photonics Technology Letters, IEEE, 1995, vol.7, no.9, p944-946.
- [73] BS Ooi, AC Bryce and JH Marsh, "Integration process for photonic integrated circuits using plasma damage induced layer intermixing", Electronics Letters, 1995, vol.31, no.6, p449-451.
- [74] A Pepin, C Vieu, M Schneider, H Launois and Y Nissim, "Evidence of stress dependence in SiO<sub>2</sub>/Si<sub>3</sub>N<sub>4</sub> encapsulation-based layer disordering of GaAs/AlGaAs quantum well heterostructures", Journal of Vacuum Science & Technology B: Microelectronics and Nanometer Structures, 1997, vol.15, no.1, p142-153.
- [75] WJ Choi, JI Lee, IK Han, KN Kang, Y Kim, HL Park and K Cho, "Enhanced disordering of GaAs/AlGaAs multiple quantum well by rapid thermal annealing using plasma enhanced chemical vapour deposited SiN capping layer grown at high RF power condition", Journal of materials science letters, 1994, vol.13, no.5, p326-328.
- [76] Jae Su Yu, Jin Dong Song, Yong Tak Lee and H Lim, "Influence of dielectric deposition parameters on the InGaAs/GaAs quantum well intermixing by impurity-free vacancy disordering", Journal of applied physics, 2002, vol.92, p1386.
- [77] P Cusumano, BS Ooi, A Saher Helmy, SG Ayling, AC Bryce, JH Marsh, B Voegele and MJ Rose, "Suppression of quantum well intermixing in GaAs/AlGaAs

laser structures using phosphorus-doped SiO<sub>2</sub> encapsulant layer", Journal of applied physics, 1997, vol.81, no.5, p2445-2447.

[78] Naoyuki Shimada, Yutaka Fukumoto, Masahiro Uemukai, Toshiaki Suhara, Hiroshi Nishihara and Anders Larsson, "Monolithic integration of lasers and passive elements using selective QW disordering by rapid thermal annealing with SiO<sub>2</sub> caps of different thicknesses", Electronics and Communications in Japan (Part II: Electronics), 2004, vol.87, no.1, p34-42.

[79] EVK Rao, A Hamoudi, Ph Krauz, M Juhel and H Thibierge, "New encapsulant source for III-V quantum well disordering", Applied physics letters, 1995, vol.66, no.4, p472-474.

[80] B Elman, Emil S Koteles, P Melman and CA Armiento, "GaAs/AlGaAs quantum-well intermixing using shallow ion implantation and rapid thermal annealing", Journal of applied physics, 1989, vol.66, no.5, p2104-2107.

[81] Stewart D McDougall, Olek P Kowalski, Craig J Hamilton, Fern Camacho, o , Bocang Qiu, Maolong Ke, RM De La Rue, A Catrina Bryce and John H Marsh, "Monolithic integration via a universal damage enhanced quantum-well intermixing technique", Selected Topics in Quantum Electronics, IEEE Journal of, 1998, vol.4, no.4, p636-646.

[82] Stewart D McDougall, Olek P Kowalski, Craig J Hamilton, Fern Camacho, o , Bocang Qiu, Maolong Ke, RM De La Rue, A Catrina Bryce and John H Marsh, "Monolithic integration via a universal damage enhanced quantum-well intermixing technique", Selected Topics in Quantum Electronics, IEEE Journal of, 1998, vol.4, no.4, p636-646.

[83] SD McDougall, OP Kowalski, AC Bryce, JH Marsh and CN Ironside, "Extended cavity ridge waveguide lasers operating at 1.5 um using a simple damage induced quantum well intermixing process", Electronics Letters, 1997, vol.33, no.23, p1957-1958.

[84] Minju Ying, Pijun Liu, Yueyuan Xia, Xiangdong Liu, Mingwen Zhao, Shuqin Xiao, Yuming Sun and Jiaoqing Pan, "Investigation of intermixing induced by sputtering and annealing in multiple quantum well", Applied Surface Science, 2003, vol.205, no.1, p182-187.

[85] XF Liu, BC Qiu, ML Ke, AC Bryce and JH Marsh, "Control of multiple bandgap shifts in InGaAs-AlInGaAs multiple-quantum-well material using different thicknesses of PECVD SiO<sub>2</sub> protection layers", Photonics Technology Letters, IEEE, 2000, vol.12, no.9, p1141-1143.

[86] Franck Robert, A Catrina Bryce, John H Marsh, Anthony J SpringThorpe and J Kenton White, "Passive mode locking of InAlGaAs 1.3-um strained quantum wells extended cavity laser fabricated by quantum-well intermixing", Photonics Technology Letters, IEEE, 2004, vol.16, no.2, p374-376.

- [87] Maria Kaminska, ER Weber, Z Liliental-Weber, R Leon and ZU Rek, "Stoichiometry-related defects in GaAs grown by molecular-beam epitaxy at low temperatures", Journal of Vacuum Science & Technology B: Microelectronics and Nanometer Structures, 1989, vol.7, no.4, p710-713.
- [88] C Dion, PJ Poole, S Raymond, P Desjardins and F Schiettekatte, "Tuning of the electronic properties of self-assembled InAs/ InP (001) quantum dots using grown-in defect mediated intermixing", Applied physics letters, 2006, vol.89, p131905.
- [89] David A Thompson, John F Hazell, Alex S Lee, Tao Yin, Gregory J Letal, Brad J Robinson, Nicholas Bertsch and John G Simmons, "New methods of defect-enhanced quantum well intermixing and demonstrated integrated distributed-feedback laser modulator", Asia Pacific Optical Communications, International Society for Optics and Photonics, 2000, p148-161.
- [90] D. K. Brice, J. A. Borders, "Ion Implantation in semiconductors", New York, Plenum Publishing Corporation, xiv, 1997, p754.
- [91] James F Ziegler, "Handbook of ion implantation technology", North-Holland Amsterdam etc., 1992.
- [92] S Charbonneau, PJ Poole, PG Piva, GC Aers, Emil S Koteles, M Fallahi, J-J He, JP McCaffrey, Mu Buchanan, M Dion and others, "Quantum-well intermixing for optoelectronic integration using high energy ion implantation", Journal of applied physics, 1995, vol.78, no.6, p3697-3705.
- [93] M Paquette, J Beauvais, J Beerens, PJ Poole, S Charbonneau, CJ Miner and C Blaauw, "Blueshifting of InGaAsP/InP laser diodes by low-energy ion implantation", Applied physics letters, 1997, vol.71, no.26, p3749-3751.
- [94] Seng Lee Ng, Hwi Siong Lim, Yee Loy Lam, Yuen Chuen Chan, Boon Siew Ooi, Vincent Aimez, Jacques Beauvais and Jean Beerens, "Generation of multiple energy bandgaps using a gray mask process and quantum well intermixing", Japanese journal of applied physics, 2002, vol.41, no.2B, p1080-1084.
- [95] SL Ng, HS Djie, HS Lim, YL Lam, YC Chan, BS Ooi, V Aimez, J Beauvais and J Beerens, "Fabrication of wide-band electro-absorption waveguide modulator arrays using quantum well-intermixing process", Optics communications, 2003, vol.226, no.1, p191-197.
- [96] HS Djie, T Mei and J Arokiaraj, "Photoluminescence enhancement by inductively coupled argon plasma exposure for quantum-well intermixing", Applied physics letters, 2003, vol.83, no.1, p60-62.
- [97] BC Qiu, BS Ooi, AC Bryce, SE Hicks, CDW Wilkinson, RM De La Rue and JH Marsh, "Reduced damage reactive ion etching process for fabrication of InGaAsP/InGaAs multiple quantum well ridge waveguide lasers", Journal of Vacuum Science & Technology B: Microelectronics and Nanometer Structures, 1998, vol.16, no.4, p1818-1822.

- [98] CJ Hamilton, SE Hicks, B Vogege, JH Marsh and JS Aitchison, "Suppression of bandgap shifts in GaAs/AlGaAs multiquantum wells using hydrogen plasma processing", Electronics letters, 1995, vol.31, no.16, p1393-1394.
- [99] GM Mikhailov, PV Bulkin, SA Khudobin, AA Chumakov and S Yu Shapoval, "XPS investigation of the interaction between ECR-excited hydrogen and the native oxide of GaAs (100)", Vacuum, 1992, vol.43, no.3, p199-201.
- [100] M Rahman, MA Foad, S Hicks, Holl, MC and CDW Wilkinson, "Defect Penetration During the Plasma Etching of Semiconductors", MRS Proceedings, Cambridge Univ Press, 1992, vol.279, no.1.
- [101] A Saher Helmy, JS Aitchison and JH Marsh, "The kinetics of intermixing of GaAs/AlGaAs quantum confined heterostructures", Applied physics letters, 1997, vol.71, no.20, p2998-3000.
- [102] HS Djie, T Mei, J Arokiaraj, C Sookdhis, SF Yu, LK Ang and XH Tang, "Experimental and theoretical analysis of argon plasma-enhanced quantum-well intermixing", Quantum Electronics, IEEE Journal of, 2004, vol.40, no.2, p166-174.
- [103] HS Djie and T Mei, "Plasma-induced quantum well intermixing for the universal high-density photonic integration", Journal of crystal growth, 2006, vol.288, no.1, p49-52.
- [104] JE Epler, RD Burnham, RL Thornton, TL Paoli and MC Bashaw, "Laser induced disordering of GaAs-AlGaAs superlattice and incorporation of Si impurity", Applied physics letters, 1986, vol.49, no.21, p1447-1449.
- [105] JE Epler, RL Thornton and TL Paoli, "Very low threshold buried heterostructure quantum well lasers by laser-assisted disordering", Applied physics letters, 1988, vol.52, no.17, p1371-1373.
- [106] A McKee, CJ McLean, AC Bryce, RM De La Rue, JH Marsh and C Button, "High quality wavelength tuned multiquantum well GaInAs/GaInAsP lasers fabricated using photoabsorption induced disordering", Applied physics letters, 1994, vol.65, no.18, p2263-2265.
- [107] Andrew McKee, CJ McLean, Giuseppe Lullo, A Catrina Bryce, Richard M De La Rue, John H Marsh and Christopher C Button, "Monolithic integration in InGaAs-InGaAsP multiple-quantum-well structures using laser intermixing", Quantum Electronics, IEEE Journal of, 1997, vol.33, no.1, p45-55.
- [108] CJ McLean, A McKee, G Lullo, AC Bryce, RM De La Rue and JH Marsh, "Quantum well intermixing with high spatial selectivity using a pulsed laser technique", Electronics Letters, 1995, vol.31, no.15, p1285-1286.
- [109] TK Ong, O Gunawan, BS Ooi, YL Lam, YC Chan, Y Zhou, A Saher Helmy and JH Marsh, "High-spatial-resolution quantum-well intermixing process in

- GaInAs/GaInAsP laser structure using pulsed-photoabsorption-induced disordering", Journal of Applied Physics, 2000, vol.87, no.6, p2775-2779.
- [110] BC Qiu, AC Bryce, RM De La Rue and JH Marsh, "Monolithic integration in InGaAs-InGaAsP multiquantum-well structure using laser processing", Photonics Technology Letters, IEEE, 1998, vol.10, no.6, p769-771.
- [111] SJ Fancey, GS Buller, JS Massa, AC Walker, CJ McLean, A McKee, AC Bryce, JH Marsh and RM De La Rue, "Time-resolved photoluminescence microscopy of GaInAs/GaInAsP quantum wells intermixed using a pulsed laser technique", Journal of applied physics, 1996, vol.79, no.12, p9390-9392.
- [112] G Lullo, A McKee, CJ McLean, AC Bryce, C Button and JH Marsh, "Fabrication of electroabsorption optical modulators using laser disordered GaInAs/GaInAsP multiquantum well structures", Electronics Letters, 1994, vol.30, no.19, p1623-1625.
- [113] Tsurugi K Sudoh, Mitsutaka Kumano, Yoshiaki Nakano and Kunio Tada, "Wavelength trimming by photoabsorption-included disordering for multiple-wavelength distributed-feedback laser arrays", Photonics Technology Letters, IEEE, 1997, vol.9, no.7, p887-888.
- [114] Jan J Dubowski, "Laser-induced bandgap shifting for photonic device integration", Google Patents, 2003.
- [115] HS Djie, BS Ooi and O Gunawan, "Quantum dot intermixing using excimer laser irradiation", Applied physics letters, 2006, vol.89, no.8, p081901-081901.
- [116] HC Casey, DD Sell and KW Wecht, "Concentration dependence of the absorption coefficient for n-and p-type GaAs between 1.3 and 1.6 eV", Journal of Applied Physics, 1975, vol.46, no.1, p250-257.
- [117] DE Aspnes and AA Studna, "Dielectric functions and optical parameters of Si, Ge, GaP, GaAs, GaSb, InP, InAs, and InSb from 1.5 to 6.0 ev", Physical Review B, 1983, vol.27, no.2, p985.
- [118] HR Philipp and H Ehrenreich, "Optical properties of semiconductors", Physical Review, 1963, vol.129, no.4, p1550.
- [119] Danny Perez and Laurent J Lewis, "Ablation of solids under femtosecond laser pulses", Physical review letters, 2002, vol.89, no.25, p255504.
- [120] Salvatore Amoruso, Riccardo Bruzzese, Nicola Spinelli and R Velotta, "Characterization of laser-ablation plasmas", Journal of Physics B: Atomic, Molecular and Optical Physics, 1999, vol.32, no.14, pR131.
- [121] Ferenc Riesz, L Dobos, C Vignali and C Pelosi, "Thermal decomposition of InP surfaces: volatile component loss, morphological changes, and pattern formation", Materials Science and Engineering: B, 2001, vol.80, no.1, p54-59.

- [122] RR Chang, R Iyer and DL Lile, "Surface characterization of InP using photoluminescence", Journal of applied physics, 1987, vol.61, no.5, p1995-2004.
- [123] Alex SW Lee, E Herbert Li and Gamani Karunasiri, "Vacancy-enhanced intermixing in highly strained InGaAs/GaAs multiple quantum well photodetector", Journal of applied physics, 1999, vol.86, no.6, p3402-3407.
- [124] Yu Huang, Fengnian Xia, Vinod M Menon, Stephen R Forrest and Milind Gokhale, "Reduction of absorption loss in asymmetric twin waveguide laser tapers using argon plasma-enhanced quantum-well intermixing", Photonics Technology Letters, IEEE, 2004, vol.16, no.10, p2221-2223.
- [125] J-J He, Sylvain Charbonneau, PJ Poole, GC Aers, Y Feng, ES Koteles, RD Goldberg and IV Mitchell, "Polarization insensitive InGaAs/InGaAsP/InP amplifiers using quantum well intermixing", Applied physics letters, 1996, vol.69, no.4, p562-564.
- [126] SR Andrew, JH Marsh, Holl, MC and AH Kean, "Quantum-well laser with integrated passive waveguide fabricated by neutral impurity disordering", Photonics Technology Letters, IEEE, 1992, vol.4, no.5, p426-428.
- [127] Dirk Basting and Gerd Marowsky, "Excimer laser technology", Springer, 2005.
- [128] Victor Pol, James H Bennewitz, Tanya E Jewell and Darryl W Peters, "Excimer laser based lithography: a deep-ultraviolet wafer stepper for VLSI processing", Optical engineering, 1987, vol.26, no.4, p264311-264311.
- [129] PM Smith, PG Carey and TW Sigmon, "Excimer laser crystallization and doping of silicon films on plastic substrates", Applied physics letters, 1997, vol.70, no.3, p342-344.
- [130] James H Brannon, "Micropatterning of surfaces by excimer laser projection", Journal of Vacuum Science & Technology B: Microelectronics and Nanometer Structures, 1989, vol.7, no.5, p1064-1071.
- [131] CJ Hayden, "Three-dimensional excimer laser micromachining using greyscale masks", Journal of Micromechanics and Microengineering, 2003, vol.13, no.5, p599.
- [132] HM Phillips, S Wahl and R Sauerbrey, "Submicron electrically conducting wires produced in polyimide by ultraviolet laser irradiation", Applied physics letters, 1993, vol.62, no.20, p2572-2574.
- [133] Eric E Mayer, David A Gillett and Sergei V Govorkov, "Fiber Bragg grating writing by interferometric or phase mask methods using high-power excimer lasers", Optoelectronics' 99-Integrated Optoelectronic Devices, International Society for Optics and Photonics, 1999, p152-160.
- [134] JR Lankard Sr and G Wolbold, "Excimer laser ablation of polyimide in a

manufacturing facility", Applied Physics A, 1992, vol.54, no.4, p355-359.

[135] Douglas B Chrisey and Graham K Hubler, "Pulsed laser deposition of thin films", Pulsed Laser Deposition of Thin Films, by Douglas B. Chrisey (Editor), Graham K. Hubler (Editor), ISBN 0-471-59218-8. Wiley-VCH, May 2003, vol.1, pp. 648.

## **Author's Biography**

### **Personal Introduction**

Mohammad Kaleem was born in the city of Faisalabad Pakistan. He completed his higher secondary education from London International College London. He received his B. Eng. (Hon's) degree in Electrical, Electronics and information System engineering from London South Bank University England, in 1997. He received his master degree from the same University in Telecommunication and Computer networks engineering in 1999. He also worked as a consultant on different projects at British Telecommunication's (B&T) Research Labs based in Marsham Heath England. He is currently doing PhD study in optical communication engineering at Zhejiang University Hangzhou China. His current research interests are in the area of photonic devices and photonic integrated circuits for next generation optical communications.

### **Publications**

- [1] Mohammad Kaleem, Xin Zhang and Jian-Jun He, "Bandgap Engineering of InGaAsP/InP Laser Structure by Argon Plasma Induced Point Defects" ACP 2012 (Ei-Index).
- [2] Mohammad Kaleem, Xin Zhang and Jian-Jun He, "UV laser induced selective-area bandgap engineering for fabrication of InGaAsP/InP laser devices" Optics and Laser Technology Journal 2013, vol.51, p36-41. (Sci-Index).
- [3] Mohammad Kaleem, Xin Zhang and Jian-Jun He, "Multi-bandgap photonic materials and devices fabricated by UV-laser induced quantum well intermixing" Optoelectronics Letters 2013 (Ei-Index).